

1 A practical guide to coding line-by-line trace gas 2 absorption in Earth's atmosphere

3 *Sergey Korkin*^{1,2,*}, *Andrew M. Sayer*^{1,2}, *Amir Ibrahim*², and *Alexei Lyapustin*²

4 ¹ University of Maryland Baltimore County, Baltimore, MD, USA

5 ² NASA Goddard Space Flight Center, Greenbelt, MD, USA

6 *Corresponding author: sergey.v.korkin@nasa.gov

7

8 *“Talk is cheap. Show me the code.”*

9 – Linus Torvalds¹

10 Abstract

11 We present two new open-source codes, in the C language, for simulation of the line-by-line
12 molecular (gas) absorption in the solar spectral region with wavelengths up to ~ 2500 (nm). The
13 first one, `gcell`, simulates absorption spectroscopy in a gas cell for a given length of the cell,
14 temperature, and pressure. The second one, `aspect`, is for spectroscopy in Earth's atmosphere -
15 a common need for remote sensing applications. Both use the HITRAN database for line shape
16 (Voigt) modeling. `Aspect` adapts height variations of the thermodynamic parameters (profiles)
17 from MODTRAN. Separate discussion of the gas cell and the atmospheric modes simplifies
18 software development, documentation, and support, and ultimately the transfer of knowledge
19 between generations of scientists. These are the main goals of the current paper. Despite the
20 existence of numerous computer programs for absorption spectroscopy, the code development
21 process is poorly covered in literature. As a result, it is difficult for a non-developer to
22 confidently modify an existing code or create a new tool within a reasonable amount of time.

¹ https://en.wikiquote.org/wiki/Linus_Torvalds (see Sec. 2000-s: 2000-04)

23 **Keywords**

24 Atmosphere absorption spectroscopy, line-by-line, open-source, code development, radiative
25 transfer (RT), Earth science.

26 **Contents**

27	Abstract.....	1
28	Keywords.....	2
29	1. Introduction.....	3
30	2. Many tools for atmospheric spectroscopy: why publish one more?.....	10
31	3. Code structure and usage	14
32	3.1 Header files	15
33	3.2 Installation, input, and output parameters.....	17
34	3.2.1 Gas cell mode.....	17
35	3.2.2 Atmospheric mode	21
36	4. Calculation of absorption by a single HITRAN line	27
37	4.1 Reading one record form the HITRAN *.par file	28
38	4.2 Molparam.txt and TIPS q-files.	30
39	4.3 Basic code for a single line	33
40	4.4 Convolution – Voigt spectrum.....	36
41	4.5 Beyond Voigt: a few legacy and recent references.....	40
42	4.6 A few numbers for validation of code for an isolated line	42
43	5. Calculation of absorption in a gas cell.....	44
44	5.1 Picking necessary lines from the HITRAN *.par files.....	45
45	5.2 The line-mixing effect, which we also neglect	46
46	5.3 Simulation of LBL absorption	47
47	5.4 Gas cell validation.....	50

48	5.4.1 Oxygen A-band at 0.764 (μm)	51
49	5.4.2 Methane band at 2.3 (μm)	53
50	6. Absorption in Earth's atmosphere	55
51	6.1 Elements of MODTRAN	55
52	6.2 Column amount of gas in atmosphere	60
53	6.3 The mysterious <i>atm-cm/km</i>	64
54	6.4 Profile of optical thickness.....	68
55	6.5 Practical units for water vapor	70
56	6.6 Aspect validation	71
57	6.6.1 Literature references	71
58	6.6.2 Numerical validation of atmospheric absorption.....	77
59	7. Conclusion	81
60	Acknowledgements.....	84
61	Authors contribution	84
62	Funding information	85
63	References.....	85
64		

65 1. Introduction

66 Absorption of radiation as a function of wavelength λ (widely used in Earth science in the solar
67 spectral region of up to approximately 2,500 (nm)) or wavenumber $\nu \sim 1/\lambda$ (more common in
68 spectroscopy) by the atmosphere-surface system is a fundamental physical process that
69 influences the Earth's radiation budget and, through that, drives its climate (Luther et al., 1988;
70 Kochanov et al., 2019; Pincus et al., 2020). Molecules absorb radiation at only specific
71 wavelengths corresponding to differences in energy between different possible quantum
72 excitation states – that is, different rotational, vibrational, and electronic configurations. For an

73 isolated molecule, these lines are pure and “monochromatic”², though in practice (whether in a
74 gas cell or Earth’s atmosphere) the fact that molecules exist in groups, interacting with one
75 another, and with different populations of excitation states, greatly complicates matters and leads
76 to broadening and shifting of lines (*Elsasser*, 1942; *Goody & Yung*, 1989; *Liou*, 2002).

77 The gas spectroscopy started to systematically attract the attention of scientists in as early as
78 XIX-th century. *Pouillet* (1838) and *Tyndall* (1859) reported on the influence of gaseous
79 absorption on transfer of solar radiation through the atmosphere. *Foote* (1856) arguably was the
80 first scientist to link the atmospheric heating rate (global warming) with CO₂ concentration.
81 Later, *Arrhenius* (1896, 1897) continued this research. In the modern era, these pioneering works
82 are continued by the Orbiting Carbon Observatory (OCO³), the Scanning Imaging Absorption
83 Spectrometer for Atmospheric Chartography (SCIAMACHY⁴), the Greenhouse Gases Observing
84 Satellite (GOSAT⁵), and other missions. Thus, the importance of the effect of atmospheric
85 absorption was recognized about two centuries ago and since then has remained a focus of the
86 atmospheric community.

87 Besides climate and weather, accurate simulation of absorption is necessary for satellite remote
88 sensing of the ocean, land, and particles suspended in atmosphere (aerosols, water droplets, ice
89 crystals). For these studies, certain optical (solar and thermal) and radio instruments, both
90 passive (radiometers) and active (lidars, radars), typically measure in “atmospheric windows”.
91 The atmospheric windows are range of wavelengths (spectral bands) where absorption is low,
92 but still not negligible. In these spectral bands the atmospheric absorption is not an object of
93 study, but an obstacle. Accurate retrieval algorithms must take this absorption into account.

94 In the Earth atmosphere, the radiation is absorbed by particles (aerosols) and molecules of trace
95 gases. Gas absorption is usually divided into two components. First, is the absorption in spectral
96 lines of the molecules, which has a pronounced spectral pattern – the absorption power may vary
97 by orders of magnitude even within a narrow spectral band – due to the aforementioned
98 dependence on specific permitted rotational, vibrational, and electronic structure transitions.

² Strictly speaking, “monochromatic” light wave is an idealization because the wave has originated at some point in time and space and will end its existence at a different point and moment of time.

³ <https://ocov2.jpl.nasa.gov/>

⁴ <https://www.sciamachy.org/>

⁵ <https://www.gosat.nies.go.jp/en/>

99 Second is the continuum absorption, which is smoother, and often that of water vapor is most
100 important (Clough et al., 1989; Shine et al., 2012; Mlawer et al., 2012 & 2023). In practice
101 parameters to fit observed gas absorption lines are determined empirically from laboratory
102 measurements on a line-by-line (LBL) basis assuming some basic line absorption shape, and then
103 the continuum is calculated as the difference between these measurements and LBL calculations.
104 Then one fits this residual absorption – arising due to the complex interplay between molecules
105 that is intractable to model purely theoretically - with models that are largely empirical. Further
106 in this paper, we focus only on the first component – absorption by spectral lines – of
107 atmospheric spectroscopy.

108 Apart from the water vapor continuum, mostly affecting wavelengths in the red and longer
109 wavelengths, there are other gases manifesting spectrally smooth variations in the UV-Vis part.
110 Ozone (O_3) is the most important absorber in this spectral range. The presence of this gas causes
111 a drop in the atmospheric transmittance towards shorter wavelengths (e.g., see the second chart
112 from the top of Fig. 2.13 in Bohren & Clothiaux, 2006), causing the need for atmospheric
113 correction. Fortunately, *a*) most ozone is located high in the Earth atmosphere, and the ozone
114 correction theoretical background is simply a direct transmittance, exponential with respect to
115 (w.r.t.) absorption optical thickness, frequently noted in RT as τ , along the solar and view
116 directions; *b*) the transmittance depends on the ozone absorption cross-sections, which possess
117 moderate temperature and pressure dependence, measured in a laboratory at different
118 concentrations, a limited set of thermodynamical conditions, and reported as look-up tables
119 (Hearn, 1961; Orphal et al., 2016). Besides ozone, these smooth components of spectral
120 absorption are measured for other important atmospheric trace gases (Bogumil et al., 2003). We
121 do not include this “continuum-type” absorption in our paper.

122 Since the mentioned pioneering works in Earth science, as well as in astrophysics, the field of
123 absorption in planetary atmospheres has been growing. Results of these studies are published in
124 dedicated journals (e.g., Journal of Molecular Spectroscopy and Journal of Quantitative
125 Spectroscopy and Radiative Transfer), monographs, chapters in books, and papers in journals not
126 specialized in spectroscopy. Spaceborne spectrometers studying Earth and other planets, and
127 countless laboratory measurements generate an avalanche of experimental data. Numerous
128 datasets combine the data in a raw and processed format (e.g., after parametrization). Some of

129 the datasets, like the widely used high-resolution transmission molecular absorption database
130 (HITRAN⁶), have become standards in science and industry (McClatchey et al. 1973; Rothman
131 et al., 1978, 2005, 2010, 2021). Examples of other spectral databases include GEISA (Delahaye
132 et al., 2020), which has been developed since the 1980s, CDMS (Müller et al., 2005), ASTER
133 (Baldridge et al., 2009), to name a few. In this paper we use that part of the HITRAN database
134 that models lines with the Voigt shape profile. We refer the reader to Sec. 4.4 below for
135 references on the Voigt spectrum and to Sec. 4.5 for some legacy and recent references on the
136 non-Voigt line shapes.

137 In this paper we also do not include one type of absorption with a smooth spectral dependence,
138 which is included in HITRAN to a certain degree. This phenomenon is (inelastic) collision induced
139 absorption – CIA (Goody & Yung, 1989: Sec.5.3.4 for O₂ and 5.5.3 for CO₂; Richard et al., 2012;
140 Karman et al., 2019). This is not to be confused with (elastic) collisional broadening. During
141 collision of molecules, some energy transitions forbidden for molecules at steady state may
142 become possible, which leads to absorption of radiation at corresponding wavelengths. CIA is
143 most important for O₂ and N₂ (Karman et al., 2018). The phenomenon manifests itself at high
144 concentrations. It is parametrized in HITRAN as scaling factors (binary coefficients) and molecule
145 concentrations, e.g. $K_{ab}(v) = k(v)/(n_a \cdot n_b)$. Here ‘a’ and ‘b’ denote two colliding molecules, ‘n’ is
146 concentration, ‘ $k(v)$ ’ is the absorption cross-section at a given wavenumber v . The dependence of
147 n on temperature T and pressure p leads to the same in the CIA coefficients.

148 Analysis and application of the collected data relies on numerical modeling. The models are
149 basically computer programs. Once developed, they may be used for decades, which assures
150 reliability (Korkin et al., 2022: see references in Sec.1). But over time they are left as black
151 boxes. Contrary to the scientific background (theory), and documenting of the measurement
152 process (technique), codes do not get enough attention. They either start as or often become
153 poorly written software due to factors such as obscure coding practices (as these evolve over
154 time), unclear structure, lack of documentation and unit testing. Input/output formats, runtime, or
155 accuracy may no longer meet the requirements of new missions. New tools are needed to
156 improve reprocessing of heritage missions, and to get the most out of upcoming Earth science

⁶ <https://hitran.org/>

157 missions such as NASA's Plankton, Aerosol, Cloud, ocean Ecosystem (PACE⁷: *Werdell et al.*,
158 2019). The PACE Ocean Color Instrument (OCI) has a finer wavelength resolution than heritage
159 NASA imagers, which demands flexible (for simulation of different and variable atmospheric
160 constituents) and accurate (to avoid bias in retrievals) software tool for atmospheric
161 spectroscopy.

162 As a result of the neglect of software it is hard or impossible, to confidently support (apply minor
163 changes) or modify (significantly change) a "black box"⁸ and/or a "spaghetti code"⁹ within a
164 reasonable amount of time - especially when the need is pressing. This problem has been
165 recognized not only in planetary spectroscopy but in science in general (*Kendall et al.*, 2008;
166 *Sanders & Kelly*, 2008; *Segal & Morris*, 2008; *Easterbrook & Johns*, 2009; *LeVeque et al.*, 2012;
167 *Pipitone & Easterbrook*, 2012; *Kanewala & Bieman*, 2014; *Wilson et al.*, 2014; *Heaton &*
168 *Carver*, 2015; *Storer*, 2017; *Adorf et al.*, 2018; *Hinsen*, 2019, *Dubey*, 2022). In Earth science,
169 legacy tools currently used at many institutions are largely limited to heritage sensors (e.g.
170 MODIS) and no longer supported as the developers have retired or passed away. Other tools
171 exist (see Sec.2), but access or support are often unavailable. Lack of support makes it difficult
172 to confidently change the code. The need to change the code arises from needs to: **a)** update
173 atmospheric spectroscopy database as new information becomes available, e.g. new HITRAN
174 release (*Zhu et al.*, 2019); **b)** add new atmospheric profile, or add absorption by a new molecule
175 or its isotopes; **c)** update with improved models of the spectral line shape, such as speed-
176 dependent Voigt profile (see Sec.4.5).

177 Code is therefore the main topic of the paper. We use and refer to known equations, but only to
178 support code documentation. We do not get into details of spectroscopy (although the reader is
179 referred to various books and papers) and refer to equations and relevant parameters as they
180 appear in the code. However, in the paper we do not discuss those "technical" parts relevant to
181 the code only: declaration of variables, memory allocation/deallocation, printouts. The reader
182 will see all that in the source that comes with the paper. In the text we focus on the tight coupling

⁷ <https://pace.gsfc.nasa.gov/>

⁸ https://en.wikipedia.org/wiki/Black_box

⁹ https://en.wikipedia.org/wiki/Spaghetti_code

183 between an equation and its representation as an element of code. Thus, at any moment, the
184 developer is focused on what is needed now.

185 For simplicity of coding, the paper introduces the process of development sequentially from
186 simple to complicated. Sec.4 shows how to read the HITRAN database, briefly explains
187 necessary parameters, and shows relevant code for calculation of the relative (per molecule)
188 absorption cross-section by a single line. We calculate the Voigt line shape in Sec.4.4 and list a
189 few references for “beyond Voigt” models of spectral line shape in Sec.4.5. Sec.4.6 gives a few
190 numbers to test calculation by a single line – unit testing. In Sec.5 we combine absorption from
191 many spectral lines assumed independent. The line mixing effect (e.g., interference of broad
192 lines) is ignored, however we provide references for further reading in Sec.5.2. For a given
193 temperature, pressure, and length of the cell we calculate the absorption optical thickness of the
194 gas (Sec.5.3). Such gas cells are used in laboratories and field measurements. Our C-code
195 `gcell` aims to support measurements that use gas cells. Sec.5.4 gives some independently
196 created data to test code `gcell`.

197 An atmosphere is basically a vertical stack of gas cells, each with some given temperature,
198 pressure, and particle species number concentrations varying with height – profiles. In Sec.6 we
199 combine the gas cell calculation with MODTRAN (*Berk et al., 2014 & 2017*) atmospheric
200 profiles, described briefly in Sec.6.1. Later in Sec.6 we integrate the profiles over height in order
201 to calculate τ between top-of-the-atmosphere (TOA) and user-defined level of height, paying
202 particular attention to units of the amount of gas in the atmospheric column. An open-source C
203 code for LBL simulation of the atmospheric spectroscopy, `aspect`, is the main product
204 presented in the paper. Note that `aspect` is a revised and updated version of the LBL solver of
205 the Spherical Harmonics Interpolation and Profile Correction (SHARM-IPC) tool (*Lyapustin,*
206 2003) for broad band RT. We show how to test `aspect` in Sec.6.6.

207 We endeavor to give the interested reader a chance to start using our codes as soon as possible.
208 For that purpose, Sec. 3 is devoted to software. It explains how to install `gcell` and `aspect`,
209 helps understand input, output, content of the header files, lists all files that come with the
210 package and explains the purpose of each. The section shows structure of both codes (call
211 graphs). As both codes overlap significantly in terms of source files used, we recommend readers

212 understand `gcell` even if one needs to simulate absorption in the atmosphere. Information from
213 Sec. 3 is sufficient to start using our codes.

214 One more topic that should be clarified from the very beginning is terminology. In what follows,
215 the word “*line*” will refer to a spectral line of a molecule, while a line with ASCII symbols in the
216 HITRAN database file will be called “*record*”. We use the word “*profile*” when we talk about
217 the change of atmospheric parameters with height. For the dependence of absorption by a single
218 line vs. wavenumber, which is often called “*line profile*”, we use the word “*line shape*”. We do
219 not deal with scattering in this paper. As a result, we often drop the word “*absorption*” for τ . For
220 the same reason, “*extinction*” and “*absorption*” are used synonymously here. “*Spectral*
221 *dependence*” refers to variation of some parameter over wavenumber or wavelength, depending
222 on the context. Speaking about software, we say “C-code” for simplicity. However, we use some
223 features from C++, e.g. we allocate and deallocate memory using `new` and `delete` functions,
224 hence one must use a compiler with C++ support.

225 In this project, we use C for the reasons of numerical efficiency, standardization, long-lasting
226 history, and wide usage in science and engineering (Press et al., 1992 & 2007; Oliveira &
227 Stewart, 2006; Gottschling, 2021). C can be easily wrapped in Python and the two follow the
228 same column-major rule for allocation of matrices in memory; the original SHARM-IPC LBL
229 tool, which we have refactored, was also developed in C. However, we do not expect much
230 knowledge of C/C++ from the reader. Basically, our codes use 1D arrays, nested loops, and
231 functions that may take scalars and arrays as input and output arguments. Tools like ChatGPT¹⁰
232 quickly provide small, clear, compilable examples for all that.

233 In the following Sec.2, which we have not yet mentioned, we provide references to some already
234 existing tools for gas spectroscopy. The list is long and by far incomplete. However, we argue
235 that our tools `gcell` and `aspect` may also find their place among the existing ones and be
236 useful for the community.

¹⁰ <https://chat.openai.com/>

237 2. Many tools for atmospheric spectroscopy: why publish one more?

238 An enormous number of tools for numerical simulation of absorption spectroscopy has been
239 created within the past ~50 years in order to meet a huge variety of practical needs. This is
240 caused by different physical environments (Earth, stars, planets), observation geometries
241 (laboratory, open air horizontal path, plane-parallel or spherical atmosphere), spectral resolutions
242 (broad band, LBL), numerical techniques (real-time calculations, lookup tables - LUTs, principal
243 component analysis - PCA, neural network – NN approaches), physical effects (spectral line
244 absorption, continuum absorption, scattering by molecules and/or aerosols and clouds), desired
245 input (spectral database and atmospheric profiles) and output parameters (transmittance,
246 radiance, flux, derivatives), target instrument design (air- vs. spaceborne, field of view, spectral
247 response functions), and, last but not least, forms of software product (stand-alone tool, linked
248 library, language, open-source or proprietary).

249 These and other needs are satisfied by the following RT tools¹¹, a complete list of which is likely
250 impossible to compile¹²: 4A (*Scott & Chedin*, 1981), AER¹³ set of RT models (e.g., LBLRTM in
251 *Clough* et al., 2005), AMSUTRAN (*Turner* et al., 2019), ATREM (*Gao* et al., 1993; *Thompson*
252 et al., 2015), BTRAM¹⁴ (*Chapman* et al., 2010), FARMS (*Xie* et al., 2016), FASCODE (*Clough*
253 et al., 1981), GENLN2 (*Edwards* et al., 1992), LINEPAK¹⁵ (*Gordley* et al., 1994), KOPRA
254 (*Stiller* et al., 2001), LOWTRAN (*Kneizys* et al., 1988), MCARaTS¹⁶ (*Iwabuchi & Okamura*,
255 2017), MODTRAN (*Berk* et al., 2014 & 2017), MolecFit¹⁷ (*Smette* et al., 2015), MOLIERE
256 (*Urban* et al., 2004), MOSART (*Cornette* et al., 1994), PSG¹⁸ (*Villanueva* et al., 2018), RADIS
257 (*Pannier & Laux*, 2019), RFM (*Dudhia*, 2017), RRTM (*Mlawer* et al., 1997), RTTOV (*Saunders*
258 et al., 1999), SpectraPlot¹⁹ (*Goldenstein* et al., 2017), STREAMER & FLUXNET²⁰ (*Key &*
259 *Schweiger*, 1998), TAPAS²¹ (*Bertaux* et al., 2017), TAU²² (*Hollis* et al., 2013 & 2014), VSTAR

¹¹ https://en.wikipedia.org/wiki/Atmospheric_radiative_transfer_codes

¹² We refer the reader to respective papers for definition of the acronyms.

¹³ <http://rtweb.aer.com/lblrmt.html>

¹⁴ <https://blueskyspectroscopy.com/>

¹⁵ <https://www.spectralcalc.com>

¹⁶ <https://sites.google.com/site/mcarats/monte-carlo-atmospheric-radiative-transfer-simulator-mcarats>

¹⁷ <https://www.uibk.ac.at/eso/software/molecfit.html.en>

¹⁸ <https://psg.gsfc.nasa.gov/>

¹⁹ <https://spectraplot.com/>

²⁰ <https://stratus.ssec.wisc.edu/fluxnet/>

²¹ <http://cds-espri.ipsl.fr/tapas/>

²² <http://www.ucl.ac.uk/exoplanets/>

260 (Bailey & Kedziora-Chudczer, 2012), σ -IASI (Amato et al., 2002; Carissimo et al., 2005).
261 Source code and user guides, in addition to publication(s), are available from corresponding
262 websites (see footnotes). Some websites provide an online interface to run calculations (in
263 particular NASA GSFC’s PSG – Planetary Spectrum Generator). Graphics processing units
264 (GPUs) are used for LBL calculations in Collange et al., (2008) – an example of modern
265 hardware usage for known theory. This GPU paper explains the implementation at a high level,
266 however, no details about the code itself are given.

267 In order to account for absorption in atmospheric windows, comprehensive RT packages that
268 focus on scattering of radiation, like ARTS²³ (Buehler et al., 2018), SASKTRAN²⁴ (Bourassa et
269 al., 2008), SCIATRAN²⁵ (Rozanov et al., 2014), SHARM-IPC (Lyapustin et al., 2010), or
270 libRadtran²⁶ (Emde et al., 2016) come with built-in and/or stand-alone tools for simulation of
271 molecular absorption. PCA (Liu et al., 2016; Yang et al., 2016; Havemann et al., 2018) and
272 AI/ML/NN techniques are also used, e.g. to reduce computational burden in broadband
273 calculations and for other purposes (Zhou et al., 2021; Kistenev et al., 2022; Prischepa et al.,
274 2023; Chen et al., 2024).

275 Input for LBL computations come from datasets containing spectral optical properties of
276 molecules and defining models that describe how these optical properties change with
277 temperature and pressure. HITRAN, updated roughly every four years, is arguably the oldest and
278 most used spectroscopic database (Rothman et al., 1978 – earliest report in the HITRAN format,
279 1987 – the name HITRAN is introduced, 2005 & 2010 & 2021 – reviews of HITRAN). GEISA²⁷
280 (Delahaye et al., 2021), ABSCO (Payne et al., 2020), and SCIAMACHY molecular absorption
281 spectra²⁸ (Bogumil et al., 2003) are other examples of databases for atmospheric applications;
282 some references to IR, far IR, microwave, and submillimeter databases are listed in (Gordon et
283 al., 2016). Appendix A in Rothman et al., (2008) explains how to convert the line intensities
284 from the Jet Propulsion Laboratory (JPL, Pickett et al., 1998) and Cologne Database for
285 Molecular Spectroscopy (CDMS: Müller et al., 2005) catalogs to that of HITRAN.

²³ <https://www.radiativetransfer.org/>

²⁴ <https://usask-arg.github.io/sasktran/>

²⁵ <https://www.iup.uni-bremen.de/sciatran>

²⁶ www.libradtran.org

²⁷ <https://geisa.aeris-data.fr/>

²⁸ <https://www.iup.uni-bremen.de/gruppen/molspec/>

286 Our paper focuses on the terrestrial atmosphere and solar spectral region, up to the wavelength λ
287 ~ 2500 (nm). For typical atmospheric conditions further in the paper we also rely on HITRAN
288 for simulation of absorption by a spectral single line. The HITRAN Application Programming
289 Interface (HAPI²⁹: Kochanov et al., 2016) is an open-source Python package that can download
290 LBL data from the HITRAN online database, HITRANonline (Hill et al., 2013 & 2016). The
291 package is well documented in the above-mentioned papers, manual, and in a carefully written
292 code. HAPI contains functions for calculation of absorption spectrum for a given temperature
293 and pressure. Different line shape models are available, but height dependence of temperature
294 and pressure are not built in. Therefore, HAPI is not convenient for atmospheric calculations on
295 a large scale but can be used for validation of the gas cell calculations and absorption coefficient
296 at a given height in atmosphere.

297 The mentioned non-exhaustive list of codes shows that some spectroscopic tools are new (use
298 modern language, GPU, provide interface for online calculations), some are old, some are
299 publicly available, but some are not. Corresponding papers and user guides describe theory
300 behind the tools, input, and output, which is convenient for an end user. But as a drawback, such
301 tools are often used as a “*black box*” which does not allow the user “*to better understand the*
302 *physics of radiative transfer*”, complicates research by obscuring “*intermediate variables*”, and
303 are imperfect for “*pedagogical purposes*” (Schreier et al., 2019: pp.2-3). A paper or a manual
304 about a package does not necessarily mean a paper or a manual explaining how to create – hence
305 confidently modify – the package. Further, a full radiative transfer package, like the one
306 simulating spectral radiance in an atmosphere, is too powerful for a simple problem, like light
307 absorption by a gas in a cell or along a horizontal path, and too complicated to learn how to use
308 and develop from scratch. Big codes are not always a good fit for small needs. The user runs
309 onto a bigger problem if there is a need to replace an absorption database in a third party
310 developed code that supports, say, only HITRAN.

311 The “*black box*” software model prevents debugging, refactoring, long-lasting support, and
312 transition of knowledge with the workforce – be those new hires, or experts coming from other
313 fields. An example of the need for relatively simple refactoring is the update of the HITRAN
314 database file format. In 2004, the file format changed from 100 characters per record (line in

²⁹ <https://hitran.org/hapi/>

315 ASCII file) to 160 (*Rothman et al., 2005*: p.142). Sec.4.1 below shows that a knowledgeable user
316 would spend a few minutes to make and test the necessary change. But even for the developer,
317 the update of theoretical foundation for absorption by a single line (Sec.4.5) will require more
318 time. The latter task is barely manageable by someone who does not understand the insights of
319 the code. In addition to lack of time for in-depth studying of the existing code, the gap in
320 knowledge may be caused by the way the existing open-source code is written.

321 The need for publication of codes was recognized in spectrometry in the 1960's (*Armstrong,*
322 1967). Despite that, our abovementioned literature analysis revealed a gap in discussing the
323 software development of the spectroscopic codes, as opposed to theoretical background. A rare
324 example is the Generic Atmospheric Radiation LBL Infrared Code (GARLIC: *Schreier et al.,*
325 2014), which is a Fortran 90/2008 re-implementation (refactoring) and extension of the Modular
326 InfraRed Atmospheric Radiative Transfer (MIRART) Fortran 77/90 code (*Schreier & Boettger,*
327 2003). MIRART and GARLIC are programs for infrared-microwave atmospheric RT forward
328 modeling and retrievals. GARLIC offers limb and nadir observation geometry, user-defined
329 instrumental field-of-view and spectral response function, Jacobians, different spectral line
330 shapes, optimized algorithms for LBL calculations of molecular cross sections, and other
331 features useful for applications. Noteworthy, the developers paid attention to the software side of
332 the scientific code (see Sec. 3: "Implementation - GARLIC" in their paper). They did not simply
333 add new features into the previous version, MIRART, but invested time in refactoring:
334 translation from Fortran 77/90 to Fortran 90/2008, with emphasis on modular structure, and
335 validation of intermediate results (unit testing).

336 Overall, the MIRART-GARLIC family is an example of caring about software in addition to
337 science: MIRART was first announced in 2000 (*Schreier & Schimpf, 2001*), this "transition
338 phase" from MIRART to GARLIC took place in 2007, the GARLIC paper was published in
339 2014. In 2019, GARLIC was reimplemented again – this time as PYthon scripts for
340 Computational Atmospheric Spectroscopy (Py4CAtS) in order to use numeric and scientific
341 Python modules for computationally-intensive code sections (*Schreier et al., 2019*). Py4CAtS
342 inherits and further extends the GARLIC capabilities, and it is publicly available³⁰.

³⁰ <https://atmos.eoc.dlr.de/tools/Py4CAtS/>

343 Now we come to answer the question from the title of this section. Despite an avalanche of tools
344 for atmospheric spectroscopy has already been reported in countless papers, and many of the
345 tools offer publicly available codes, the process of development of a spectroscopic tool is poorly
346 covered. In our paper, we discuss the development of a simple (compared to many others) code.
347 But we show the process of the development from the very beginning in three modes: absorption
348 by a single line (“basic”), absorption in a gas cell by a group of lines (“moderate”), and
349 absorption in atmosphere that involves atmospheric profiles (“hard”). If the user needs to
350 simulate absorption in a gas cell or along a horizontal path (no profiles), the “hard” part can be
351 dropped. Through that, we wish not to overload the reader with unnecessary details. We used a
352 similar approach in our previous paper on how to understand and write from scratch a program
353 for numerical simulation of multiple scattering of sunlight in a plane-parallel atmosphere,
354 commonly referred to as radiative transfer code (Korkin et al., 2022).

355 In a short, our goal is a simple tool explained at the code level. To meet the goal, we target
356 developers first and users next. However, before one starts digging through the code
357 development process, it is a good idea to prove that the offered code works. It is also practical to
358 immediately show the complexity of the code, so that a potential developer would estimate the
359 time needed for the job. Our next section explains the code structure and shows how to install
360 and use it.

361 3. Code structure and usage

362 This section serves as a quick start guide. It explains a simple installation process, input, output,
363 and structure of the code – see **Fig.1(a, b)**. After reading this section, the reader will be able to
364 confidently use our codes for calculating of the LBL absorption optical thickness $\tau(v)$ in a gas
365 cell or in the atmosphere, at the desired wavenumbers, v (cm^{-1}). The wavenumber is literally the
366 number of wavelengths fitting 1 (cm): v (cm^{-1}) = $10^4 / \lambda$ (μm) = $10^7 / \lambda$ (nm).

367 In this section and onwards, we use the following notation. The `Courier` font is used for the
368 software relevant text: elements of code, commands, file names, paths, input and output data. We
369 use **bold** symbols for arrays, and *italic* for parameters (mostly defined in headers). Hence
370 **bold italic** refers to an array defined in a header file. We use the C-notation to refer to an
371 element i of an array: `A[i]`. As the reader will see, `gcell` and `aspect` uses 1D arrays only.

372 We type the unit conversion constants in `grey`. In naming convention, we prefer
373 `under_score` over `CamelCase`, despite the latter was found preferable for speed and
374 accuracy of manipulating programs (Binkley et al., 2009).

375 The code has no preferences regarding the C-compiler and has been tested using GCC under
376 Linux, and Intel C compiler integrated into Microsoft Visual Studio via oneAPI toolbox. Before
377 compilation, it is necessary to check paths to the HITRAN database in the header
378 `./src/paths.h` and update, if necessary, as explained in the next section. We also
379 recommend the reader to get acquainted with the content of the headers before using, not to
380 mention changing, the code.

381 The end-of-line marker in Windows ASCII file may cause “segmentation fault” error under Unix
382 or a HITRAN data file is not read properly: output is populated with zeros and code prints out
383 `nlines=0` despite visual inspection of the HITRAN file tells the opposite. An easy fix is to
384 open and save all ASCII files (input and HITRAN database) under Unix. Although we made sure
385 to perform this open-save operation for all ASCII files, and ran all tests on a Linux machine, we
386 advise the user to try the fix again, should the error occur.

387 [3.1 Header files](#)

388 Code `aspect` uses three primary header files, `paths.h`, `const_param.h` and
389 `hprofiles.h`, and one auxiliary header `cmplx.h`. The goal of the three is to localize all
390 parameters, including paths to files with the HITRAN data, in just a few files. Using these files,
391 updating or adding a new molecule, isotope, or changing the profile (in `aspect`) is
392 straightforward. The first header is short. It contains paths to the HITRAN database, `*.par` and
393 `TIPS` (Sec.4.2) files. The user must check these paths before compilation and update as needed.

394 The next header, `const_param.h`, contains values of physical constants (e.g., speed of light,
395 standard temperature and pressure, the Planck constant, etc.), precomputed mathematical
396 constants (e.g., π , square root of π , natural logarithm of 2, etc.), scale factors to convert units
397 (e.g., `mbar_to_atm = 1.0/1013.25` converts pressure from millibars to atmospheres),
398 file names (e.g., HITRAN `*.par` files with the line parameters, “q”-files for isotopes),
399 parameters of isotopes for each molecule (e.g., number of isotopes per each molecule,
400 abundance, molar mass, etc.), some accuracy parameters, e.g., `tau_min` is the smallest value

401 of the total τ to be saved in the binary file - all smaller τ are ignored; `delta_nu = 25.0`
402 means that contribution from all HITRAN lines within $\Delta\nu = 25$ (cm^{-1}) from the given frequency
403 is significant. This 25 (cm^{-1}) is a standard cutoff in line shape models in the solar reflectance
404 band (*Clough et al., 1981: p.152; Lyapustin, 2003: p.870; Shine et al, 2012: p.542*).
405 Alternatively, the cutoff can be defined as a certain number of half-widths at half-maximums
406 (HWHM). For example, HAPI uses 50 HWHMs as default cutoff value (*Kochanov et al, 2016:*
407 *p.25*). One should check appropriate literature and update the parameter as necessary.

408 A peculiar parameter is `water_mass_density = 1.0` (g/cm^3) which is used to convert
409 the water vapor columnar amount in *atm-cm* (Sec. 6.3) to the precipitated (liquid) water
410 equivalent in *cm* and at standard temperature. Of course, this scale factor of 1.0 could be
411 dropped in calculations, at the expense of code readability.

412 The last header, `hprofiles.h`, contains extracts from MODTRAN: temperature, pressure, air
413 density, and molecular concentration height profiles, for six standard atmospheric profiles and
414 eight molecules. It also defines grid of heights, `zkm[]`. In Sec.6, we talk more about its
415 content.

416 As a first step, the user is supposed to download the package `aspect_gcell` from the
417 journal website³¹ or from our GitHub repository³²; unzip if necessary. Note that GitHub has a
418 25Mb limitation on file size. Because of that, we have zipped `./hitran/01_hitdb.par`
419 and `./hitran/06_hitdb.par` (HITRAN data for H₂O and CH₄, respectively) before
420 uploading. These must be unzipped into the same directory before use. We uploaded other
421 HITRAN *.par files, including the one for a single O₂-record, without compression. We
422 assume in subsequent that all files and folders are in `aspect_gcell` folder; all paths are
423 defined relevant to it – see our GitHub repository for structure of folders and files. Once all paths
424 have been confirmed, both programs are ready for compilation.

³¹ In this case, all source files are in the same directory; `make_directories.py` creates proper subdirectories.

³² https://github.com/korkins/aspect_gcell/

425 3.2 Installation, input, and output parameters
 426 3.2.1 Gas cell mode
 427 As software goes, `gcell` is a relatively simple, small code. **Table 1** shows files necessary to
 428 run the code; **Fig.1(a)** shows its structure. The HITRAN database and TIPS files for molecules
 429 #1-7 and 10 (HITRAN molecular numbering is discussed shortly in Sec. 4.1) come with the code
 430 in `./hitran/` and `./hitran/TIPS/`, respectively, but are not shown in the table and on
 431 the chart.

432 **Table 1:** Description of files for `gcell`. Makefiles and the `main (...)` program file come first in the list,
 433 followed by other source files, headers, input and output ASCII files. Location of each file in the
 434 distributive is shown assuming `./` is the directory where the package was extracted. Files used only for
 435 the gas cell code (and not aspect) are highlighted in gray.

File name and location	File purpose
General files	
<code>./makefile</code>	A makefile that runs both <code>makefile_g</code> (gas cell mode) and <code>makefile_a</code> (atmospheric mode)
<code>./makefile_g</code>	Make file for gas cell mode only.
C source files	
<code>./src/main_gcell.cpp</code>	Main program file. Calculates LUT with $\tau(v)$ for a gas cell and saves the LUT into a file.
<code>./src/count_lines.cpp</code>	Counts the number of records (lines in HITRAN file) within an interval $[v_{\min} : v_{\max}]$ in the HITRAN * <code>.par</code> file and returns the index for the first line, if found.
<code>./src/isotops.cpp</code>	Calculates TIPS ratio for the given temperature and returns parameters of all isotopes of the given molecule
<code>./src/ix1ix2.cpp</code>	For a given interval, it returns the first <code>ix1</code> and last <code>ix2</code> indices of array elements belonging to the interval; zero-offset for <code>ix</code> is assumed.
<code>./src/read_hitran160.cpp</code>	Reads the HITRAN data from a * <code>.par</code> file assuming 160-symbols long format
<code>./src/voigt/humlicek.cpp</code>	Calculation of the Voigt spectrum using <i>Humlíček</i> algorithm; borrowed from SHARM-IPC (<i>Lyapustin, 2003</i>)

./src/voigt/cmplx.cpp	Defines complex arithmetic operations for humlincek.cpp; borrowed from SHARM-IPC (Lyapustin, 2003)
Headers	
./src/paths.h	Defines paths to HITRAN database and TIPS files
./src/const_param.h	Defines physical and mathematical constants, HITRAN and TIPS file names.
./src/voigt/cmplx.h	Header for humlincek.cpp and cmplx.cpp files; borrowed from SHARM-IPC (Lyapustin, 2003)
Input and output ASCII files	
./gcell-o2a.inp	Test input for oxygen A-band scenario (Sec. 5.3.1).
./gcell-ch4.inp	Test input for methane scenario (Sec. 5.3.2).
./check/gcell_o2_check.txt	Output for gcell-o2a.inp for checking purpose
./check/gcell_ch4_check.txt	Output for gcell-ch4.inp for checking purpose
./check/gcell_noinp_check.txt	Output for gcell when run without input file

436

437 The makefile contains GCC commands, with flags, to compile all sources under Unix and
 438 link these into an executable. Running the make command starts compilation of gcell first,
 439 followed by aspect. This process takes a few seconds. Alternatively, the user may run make
 440 -f makefile_g to compile the gas cell mode only. Under Windows, the user simply creates a
 441 Visual Studio project, dumps the source files in it, and compiles in Debug or Release mode.

442 Once compiled, gcell can be checked by running this command without arguments (we
 443 assume a Unix environment hereafter; note ./ in the command below)

444 \$./gcell

445 In this case, gcell tells the user that no input file is provided and the default O₂ A-band case
 446 will run. In ~0.1 seconds a file named o2.txt will appear in the gcell directory, containing
 447 two header lines explaining the content of the output file and an array with two columns. The top
 448 line contains a fill value (to keep the shape of the array) and the column number density *n*
 449 (*molec/cm*²). Next come wavenumbers, *v* (*cm*⁻¹), in the left column and corresponding optical

450 thickness $\tau(v)$ in the right one. This mode quickly tests the package – compare the content of
451 O2.txt with ./check/gcell_noinp_check.txt.

452 A user defined input comes from a text file with a fixed (in terms of sequence of input
453 parameters) format:

454 molec_id nu_usr_min nu_usr_max dnu lcm T_kelv p_atm fname

455 Parameters in the line (with data types), left to right are:

456 molec_id (integer) defines the gas species following HITRAN's notation: 1 (H_2O) –
457 water vapor; 2 (CO_2) – carbon dioxide; 3 (O_3) – ozone; 4 (N_2O) – nitrous oxide; 5 (CO) –
458 carbon monoxide; 6 (CH_4) – methane; 7 (O_2) – molecular oxygen; 10 (NO_2) – nitrogen
459 dioxide. These are some species commonly used for passive remote sensing of Earth's
460 atmosphere and surface from satellites in the visible and near-infrared portions of the solar
461 spectral range. However, the user should check for the importance of absorption by other
462 species in their spectral region of interest.

463 nu_usr_min, nu_usr_max, dnu (double) define grid of wavenumbers, $v (cm^{-1})$. The
464 minimum (left) and maximum (right) points in the grid are nu_usr_min and
465 nu_usr_max, respectively.

466 lcm (double) length of the gas cell in cm .

467 T_kelv (double) temperature in the gas cell in Kelvins (K).

468 p_atm (double) pressure in the gas cell in atmospheres (atm).

469 fname (string) defines output file name (optionally, with path – up to 256 symbols long).

470 Consider gcell-ch4.inp with the following content:

471 6 4081.901 4505.699 0.002 8.0 296.0 1.0 gcell-ch4.txt

472 One runs this case by typing³³

473 \$./gcell gcell-ch4.inp

³³ In MS Visual Studio, add the file via Configuration Properties\Debugging\Command Arguments

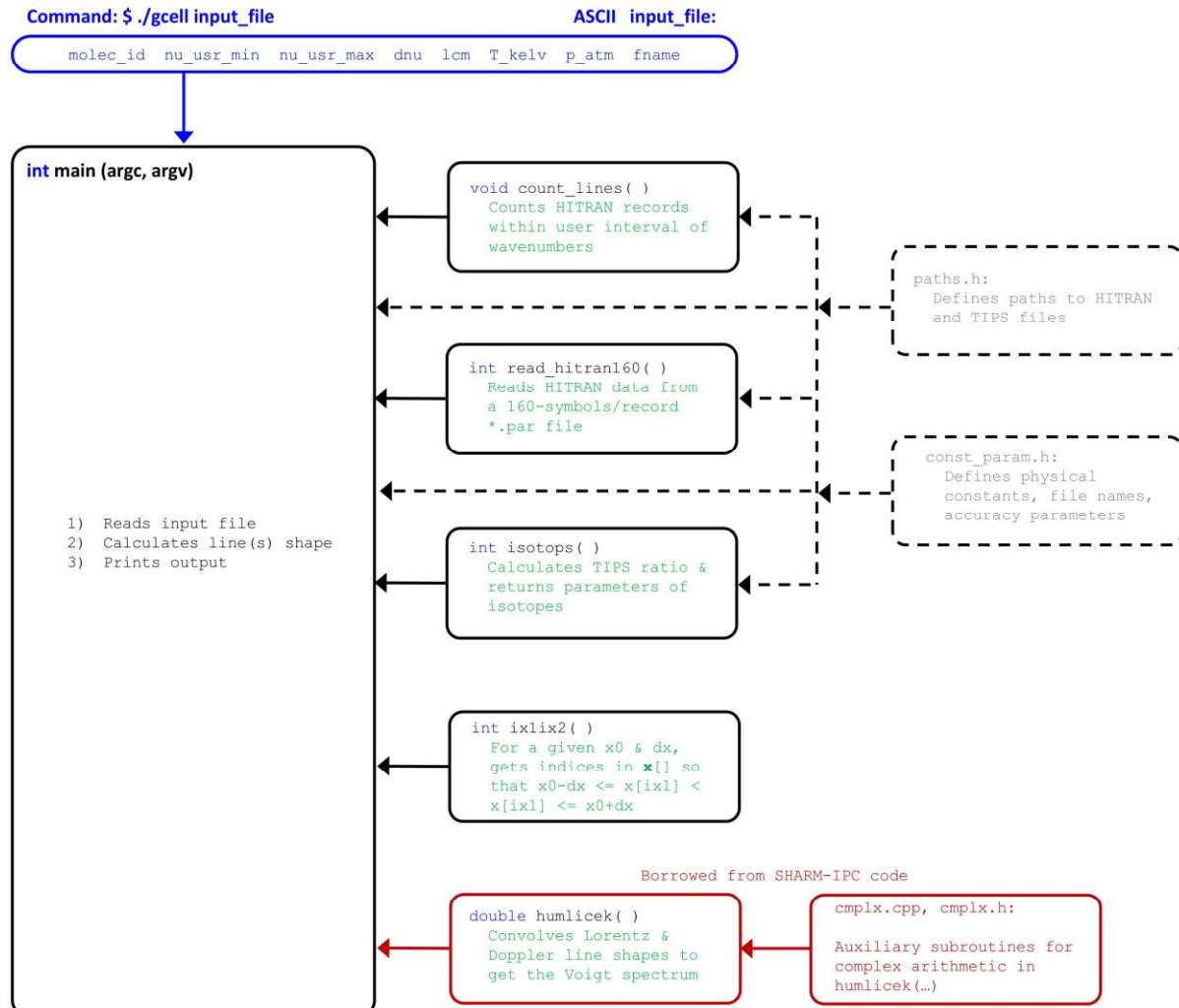


Fig.1(a): Structure of gcell. Subroutines are shown in the order they are called. Dashed lines correspond to header files.

476 It corresponds to simulation of methane, CH₄, which is HITRAN's molecule #6, across the
 477 [4081.901, 4505.699] (cm⁻¹) spectral band with step 0.002 (cm⁻¹) in an 8 (cm) long gas cell at
 478 temperature 296 (K) and pressure 1 (atm). According to the last parameter, the output file is
 479 gcell-ch4.txt.. If the input and the executable files are not in the same directory, a full path
 480 must be specified. As defined in paths.h, the full path length must not exceed 256 characters:
 481 path_len_max = 256.

482 We provide gcell-ch4.inp with the package. The corresponding output data, generated on
 483 our side, is located in ./check/gcell-ch4_check.txt. We also provide an input file

484 gcell-o2a.inp. and the corresponding output in ./check/gcell-o2a_check.txt
 485 for an oxygen A-band scenario.

486 Spaces and tabs in the input files are ignored. However, due to fixed format of the input, the
 487 input parameters are not optional. In the gas cell mode, we assume natural atmospheric
 488 abundances for isotopes (which HITRAN parameters already account for). Otherwise, one must
 489 rescale the abundances from HITRAN's default to those used *de facto*.

490 The gas cell assumes a single type of molecule. By changing one line of code, see Eq.(8) below,
 491 it is easy to account for a gas-air mixture. Thus, the gas cell mode can be used for simulation of
 492 absorption of molecules of the gas on a horizontal path in the air. In this case, the temperature
 493 and pressure remain constant, but one must modify input to account for the mixing ratio, and the
 494 "gas cell" will be long, e.g., $1\text{cm} = 100000.0$ for a 1 (km)-long trace. With these few last
 495 comments made, we continue to the atmospheric mode – code aspect.

496 3.2.2 Atmospheric mode

497 The codes aspect and gcell share some source files. In addition to those from **Table 1**
 498 without grey highlighting, **Table 2** shows files that pertain exclusively to aspect. For example,
 499 aspect uses all the same headers as gcell, and one more, hprofiles.h – the only one
 500 listed in **Table 2**. **Fig. 2(b)** shows structure of aspect.

501 **Table 2:** Description of files for aspect. The content is like in **Table 1**, which non-highlighted files are
 502 also dependencies of aspect.

File name and location	File purpose
General files	
./makefile_a	A make file for atmospheric mode only.
C source files	
./src/main_aspect.cpp	Calculates LUT with spectral and height dependence of $\tau(v)$ and saves the LUT into a file.
./src/hisotops.cpp	For each isotope of a given molecule, calculates the TIPS ratio as a function of height, and returns the molar mass, abundance, and the number of isotopes.
./src/intparab.cpp	Approximates 3 points with a parabola and integrates it for a given interval, covered by the parabola.

./src/kabs.cpp	Calculates the spectral absorption cross-section per molecule.
./src/simpson.cpp	Numerically integrates a function using Simpson's rule ³⁴ .
./src/tauabs25.cpp	Integrates the extinction profile over height from TOA to a set of user-defined heights not exceeding $z = 25$ (km). For any altitude above this point, the function returns integral from TOA to 25 (km)
Headers	
./src/hprofiles.h	Contains MODTRAN profiles for temperature, pressure, air number density, relative concentration of the gas species, and grid of heights.
Input and output ASCII data files	
./aspect-ch4.inp	Test input for a methane scenario; runtime ~1800 seconds (45823 relevant HITRAN-2020 lines).
./aspect-o2a.inp	Test input for the oxygen A-band scenario; runtime ~2 seconds (345 relevant HITRAN-2020 lines)
./check/aspect_noinp_check.txt	Output for aspect called without input file.
./check/aspect_ch4_check.txt	Output for aspect-ch4.inp for checking purpose
./check/aspect_o2_dat_check.txt	Output for aspect-o2a.inp containing metadata: initial point of the wavenumber interval v_0 , step dv , number of points over v , number of altitude points. This file also shows 2 Python commands for reading the binary files (see below).
Output binary data files	
./check/aspect_o2_check.bin	Output for aspect-o2a.inp with $\tau(v)$ as 32-bit floating point numbers as a function of height (lead dimension) and wavenumber.
./check/aspect_o2_inu_check.bin	Output for aspect-o2a.inp with the wavenumber grid expressed as a 32-bit integer index.

503

504 Once compiled, the following command is used to run aspect from the command line (like for
 505 gcell, we assume commands are typed in Unix environment)

³⁴ https://en.wikipedia.org/wiki/Simpson's_rule

```

506  $ ./aspect filename
507  The filename is an ASCII file with input parameters in the following format:
508  molec_id iatm column_amount nu_usr_min nu_usr_max dnu nzkm zkm[] fname fmt
509  Parameters, left to right are:
510  molec_id (integer) defines a molecule of gas following the HITRAN notation (see
511  gcell discussion above)
512  iatm (integer) – defines atmospheric profile of temperature and pressure following
513  MODTRAN: 1 – Tropical, 2 – Midlatitude Summer, 3 – Midlatitude Winter, 4 – Subarctic
514  Summer, 5 – Subarctic Winter 6 – Standard US 1976 atmosphere (see Sec. 6.1);
515  column_amount (double) defines the atmospheric total column amount of the selected
516  gas. For the water vapor, molec_id = 1, the column amount indicates centimeters of
517  precipitated water (see Sec. 6.5). For all other molecules, the column amount is defined in
518  parts per million in a volume (ppmv). Negative value, e.g. -1.0, instructs aspect to borrow
519  the column amount from MODTRAN (see Sec. 6.2).
520  nu_usr_min, nu_usr_max, dnu (double) define a grid of wavenumbers,  $v (cm^{-1})$ . The
521  minimum (left) and maximum (right) points in the grid are nu_usr_min and
522  nu_usr_max, respectively. To include the maximum point, aspect calculates the
523  number of points in the grid, nnu, by rounding the number of intervals towards the nearest
524  greater integer using ceil
525  nnu = int(ceil((nu_usr_max - nu_usr_min) / dnu)) + 1
526  Note, higher nnu impose higher requirements on memory.
527  nzkm (integer) defines the number of heights at which the absorption optical depth will be
528  calculated. The amount of memory required for calculations and the size of the output file
529  depend on nnu*nzkm.
530  zkm[nzkm] (double, array of nzkm elements) – defines array of heights, in kilometers (km),
531  from the lowest to the highest one, w.r.t. the ground level,  $z = 0.0 (km)$ . The output value at

```

532 the requested height **zkm** [*iz*] corresponds to τ from the MODTRAN's TOA level, $z = 120$
533 (km), to the given height.

534 **fname** (string) defines output file name (optionally, with path – up to 256 symbols long).

535 **fmt** (string of 3 characters) defines format of output: **txt** – ASCII (1 file will be returned), **bin**
536 – binary (3 files will be returned: 2 * .bin and 1 * .txt).

537 Tab(s) or more than one space are allowed as delimiters in the input file.

538 We assume it is the user's responsibility to provide meaningful input. Neither **aspect** nor
539 **gcell** check the input file for correctness, the only exception is to check if the given **imolec**
540 is included. It is convenient to keep the input file(s) in the same folder with the **aspect**
541 executable. Otherwise, the user is expected to provide a full path to the input file. If the input file
542 is missing at the specified location, **aspect** will notify the user and stop execution. If the input
543 file is not specified at all, **aspect** will run a default scenario for the oxygen A-band, O_2A ,
544 defined as follows:

545 7 6 -1.0 13050.0 13160.0 0.01 3 0.0 2.5 5.0 02 txt

546 This default option is good for a quick check. As explained above, this input is for oxygen O_2
547 (**molec_id** = 7), standard US 1976 MODTRAN profile (**iatm** = 6, see Sec.6.1) and the
548 total amount of gas from the same (**column_amount** = -1.0, see **Table 6** below), for the
549 wavenumber grid ranging from 13050 (cm^{-1}) to 13160 (cm^{-1}) with step 0.01 (cm^{-1}), and for
550 **nzkm** = 3 heights located at BOA, 0.0 (km), 2.5 (km), and 5.0 (km). The last parameter,
551 **txt**, tells **aspect** to save output as an ASCII file. Note, again, that **aspect** returns partial
552 column optical thicknesses (from TOA to the given altitudes), not the layer one calculated as
553 difference between partial column optical thicknesses.

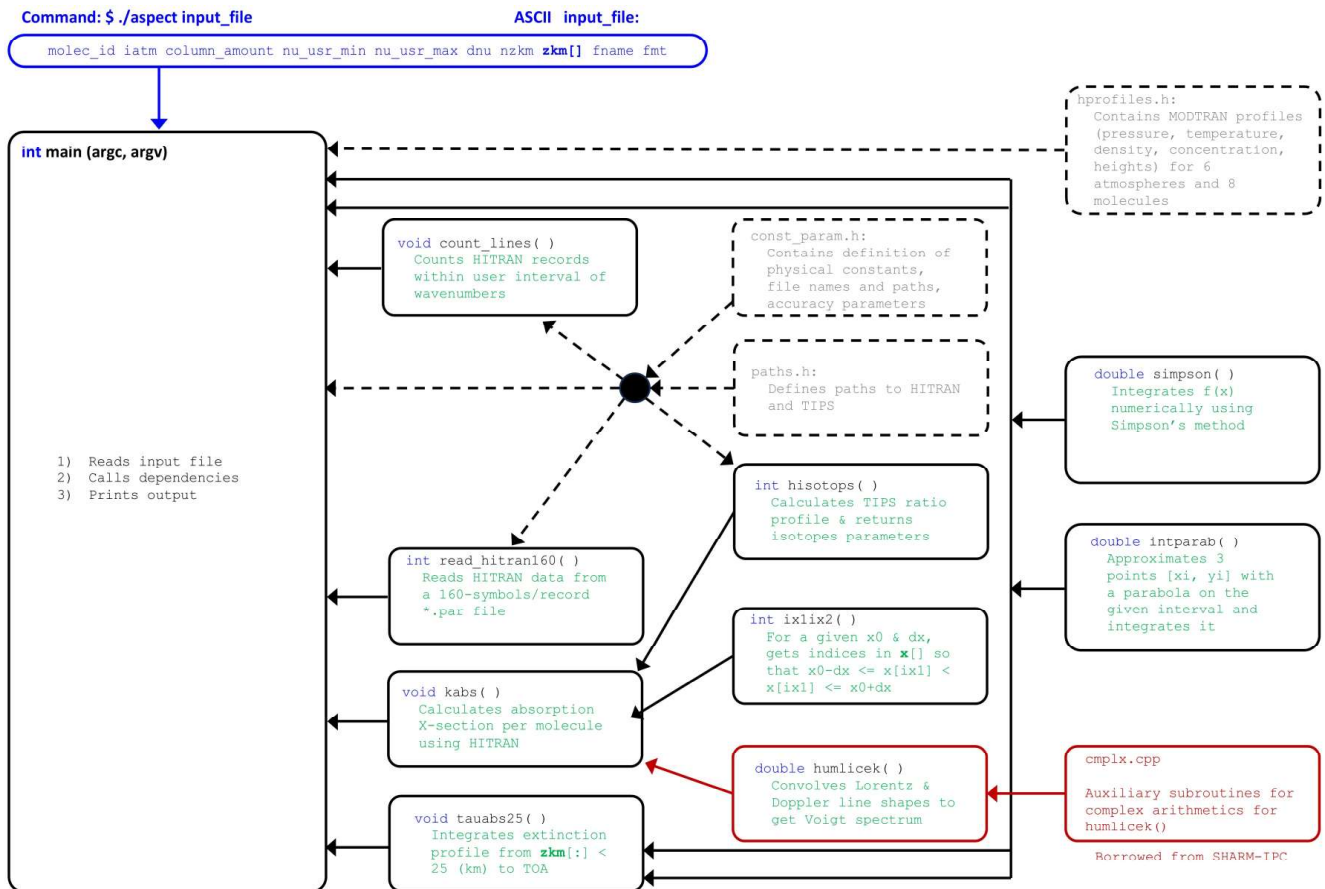


Fig.1(b): Structure of aspect. Dashed lines – headers, red – unaltered part from SHARM-IPC. Each block corresponds to a separate file. Except for `cmplx.cpp`, one file contains one function.

555 The output file `O2.txt` for the default case looks as follows (the first 4 and last 3 lines are
556 shown; the result may look slightly different if the HITRAN database has changed, these
557 correspond to HITRAN 2020 O₂ data as downloaded in October 2024)

```
558     # columns: [1] index inu, [2] nu (cm-1), [3:] tau from TOA to zkm =
559     0.000  2.500  5.000
560     0  13050.0000  2.725424e-01  1.365520e-01  6.542805e-02
561     1  13050.0100  2.838314e-01  1.421957e-01  6.812620e-02
562     2  13050.0200  2.958670e-01  1.482122e-01  7.100233e-02
563     ...
564     10998 13159.9800  4.738309e-01  2.376659e-01  1.140908e-01
565     10999 13159.9900  4.857890e-01  2.432799e-01  1.166022e-01
566     11000 13160.0000  4.994583e-01  2.497651e-01  1.195352e-01
```

567 Starting from the second line onwards, the left column indicates an integer wavenumber index,
568 `inu`, and the corresponding wavenumber `nu[inu]`, calculated as follows

```
569     nu[inu] = nu_usr_min + inu*dnu;
```

570 Next comes τ as integrated from TOA to 0.0, 2.5, and rightmost column 5.0 (km). Excluding the
571 header line (#), the file contains 11001 records:

```
572     nnu = (13160 - 13050)/0.01 + 1 = 11001.
```

573 The ASCII file is convenient for visual inspection, e.g. at debugging stage. For a smaller size of
574 the output file and faster reading of the data into memory, the binary format is preferable: `fmt`
575 = `bin`, see file `aspect-o2a.inp` as an example. In this case, `aspect` generates three files
576 on output. The first one, `O2_dat.txt`, contains information necessary to read in the binary
577 files: the number of the spectral and height grid points. It also tells that floating-point numbers
578 are stored in the single precision 32-bit format. The other two, `O2_inu.bin`, and `O2.bin`,
579 contain 32-bit integer indices `inu` for the corresponding wavenumbers. In `O2.bin`, the height
580 grid is the lead dimension; for each given wavenumber index, optical thicknesses at different
581 heights are stored consecutively.

582 The following Python script reads τ from the binary file and converts the 1D array into a 2D
583 array with heights changing column wise and wavenumbers – row wise:

```
584     import numpy as np
585     data = np.fromfile('O2.bin', dtype=np.float32)
```

```

586     tau[0:nnu, 0:nzkm] = np.reshape(data, (nnu, nzkm))
587     # O2_dat.txt contains nnu & nzkm
588 For the default O2A case, O2.bin is about 5.5 times smaller than O2.txt: 709Kb/129Kb.
589 Also, when saving and reading binary files on different machines, the user must care for
590 endianness35.
591 Based on the user-defined threshold for  $\tau$  at the lowest height (usually, at BOA), aspect may
592 skip insignificant values to reduce the size of the output *.bin file. In this case, the number of
593 records will not match the number of grid points. The threshold  $\tau$  is defined in
594 const_param.h; the current setting is tau_min = 1.0e-4, which corresponds to a one-
595 way vertical transmittance in atmosphere  $T(v, \mu = 1) = 0.9999$  (see Eq.(24) below).
596 At this point, the reader is familiar with two modes of the code, and input and output format.
597 This is the basic user level. An extension to the user level is understanding of the code structure:
598 C-functions and their purpose, as charted in Fig.1 (a, b). Now we proceed to the level of
599 development. The first step is calculation of the absorption coefficient  $k$  (cm2/molec) by a single
600 line as parameterized by a corresponding HITRAN record. Since gcell does not consider
601 height profiles, we recommend following our discussion with that code.

```

602 4. Calculation of absorption by a single HITRAN line

603 This section shows how to calculate the absorption cross-section k (cm²/molec) for a single line
604 using HITRAN parameters. As the units of k indicate, the cross-section is defined per one
605 molecule of gas present. This standard practice will be assumed hereafter and the words “per
606 molecule” will be dropped. As a prerequisite, we assume the user has downloaded the HITRAN
607 database for molecules 1 through 7 and 10. The HITRAN ASCII *.par files with the line
608 shape parameters come in the current 160-symbols-long format. The user should get acquainted
609 with the HITRAN theoretical background using, e.g., online HITRAN manuals^{36, 37} or papers
610 (Rothman, 1998: p.708; Pliutau & Roslyakov, 2017 – note, the latter describes an educational
611 software). Since typos are always possible, we recommend checking references from different

³⁵ <https://en.wikipedia.org/wiki/Endianness>

³⁶ <https://hitran.org/docs/definitions-and-units/>

³⁷ <http://www.bytran.org/howtolbl.htm>

612 authors, or different years from the same authors. All numerical results that we show in this
613 paper correspond to HITRAN 2020 downloaded from the HITRANonline website³⁸.

614 [4.1 Reading one record form the HITRAN *.par file](#)

615 It is instructive to create and read a HITRAN file with only one record. As an example, we pick
616 one O₂ line at $\nu = 13000.816219$ (cm^{-1}) and read it using the `read_hitran160(...)` function.
617 For reproducibility and simplicity of debugging, our `./hitran/` folder contains a file in the
618 HITRAN 160-symbols-long format with only the named line `07_hitdb_one_line.par`.
619 The main command executed in `read_hitran160(...)` is

```
620     fscanf(fin, "%2c%1c%12c%10c%10c%5c%5c%10c%4c%8c%93c%c",
621             str_molec_id, // molecule ID
622             str_isotop_id, // isotope ID
623             str_nuij, // transition wavenumber in vacuum
624             str_Sij, // line intensity at T=296K scaled by isotope abundance
625             str_Aij, // Einstein coefficient (not used in this paper)
626             str_gamma_air, // air-broadened Lorentzian HWHM
627             str_gamma_self, // self-broaden HWHM at T = 296 (K) and P = 1 (atm)
628             str_Elower, // Lower state energy, E''
629             str_n_air, // temperature exponent for the air-broadened HWHM
630             str_delta_air // air induced pressure shift referred to P = 1 (atm)
631             str_tail, // the rest of the line is not used
632             chr_end_of_line);
```

633 It explicitly shows the structure of the HITRAN *.par file. Note that the total number of
634 characters being read is 160 as the function name says. However, it is easy to adapt this
635 command for reading an old 100-characters long *.par file used until HITRAN 2004 edition
636 (Rothman, 2005: Table 1). All these parameters, except for `str_molec_id` (known at input)
637 and the Einstein coefficient (not used in our calculations), are converted from the character data
638 type either to integer (using `atoi`) or the floating point number (`atof`), as appropriate.

639

640 **Table 3:** Output of the `read_hitran160(...)` function; the function `count_lines(...)` from
641 **Table 1** defines the number of lines `nlines` to be read and the first line `iline0` to start reading.
642 The reference temperature and pressure are $T_{ref} = 296^{\circ}(K)$ and

³⁸ <https://hitran.org/lbl/>

643 $p_{ref} = 1.0 \text{ (atm)} = 1013.25 \text{ (Pa)} = 760 \text{ (torr)}$, respectively. For list of all HITRAN parameters with units
 644 see (Rothman, 1986: p.4060) and (Gordon, 2017: p.5).

Name	type[size]	Notation	Units	Explanation
isotop_id	int[nlines]	-	none	Isotope ID, as in HITRAN, to get proper isotope properties (e.g., molar mass): 1 = most abundant, 2 = second, etc.
nuij	double[nlines]	v_{ij}	cm^{-1}	Transition wavenumber between levels i and j (also called frequency)
Sij	double[nlines]	S_{ij}	$\frac{cm^{-1}}{molec \cdot cm^{-2}}$	Line intensity weighted with isotope abundance, I_a , at T_{ref} .
gamma_air	double[nlines]	γ_{air}	$\frac{1}{atm \cdot cm}$	Air-broadened Lorentzian HWHM at $p = 1 \text{ (atm)}$ and $T = 296 \text{ (K)}$ for Voight line shape.
gamma_self	double[nlines]	γ_{air}	$\frac{1}{atm \cdot cm}$	Self-broadened Lorentzian HWHM at $p = 1 \text{ (atm)}$ and $T = 296 \text{ (K)}$ for Voight line shape
Elower, Epp	double[nlines]	E''	cm^{-1}	Lower state energy
n_air	double[nlines]	n_{air}	none	Temperature-dependence exponent for the air-broadened HWHM, γ_{air}
delta_air	double[nlines]	δ_{air}	$\frac{1}{atm \cdot cm}$	Pressure shift induced by air, referred to $p = 1 \text{ (atm)}$

645

646 Historically, the HITRAN database convention used one symbol for the isotope number thus
 647 assuming up to 9 isotopes (1 = most abundant, 2 = second...) per molecule at most. However, for
 648 some molecules more isotopes have been introduced over time. E.g., for CO₂ (`molec_id` =
 649 2), HITRAN defines 12 isotopes using ID-s 0, A, and B for isotopes 10, 11, and 12, respectively,
 650 which must be checked before converting the isotope ID from character to integer. Note also that
 651 the line intensity, S_{ij} , is already scaled by the isotope abundance (De Biévre et al., 1984;
 652 Böhlke et al., 2005) as found in the terrestrial atmosphere, so for such applications no further
 653 scaling is necessary.

654 Other than these two peculiarities, reading the standard HITRAN database in ASCII format is
 655 not a problem. For our example of the single O₂ line, we have `nline` = 1 (total number of

656 lines), `iline0 = 0` (zero-offset index of the first line in the HITRAN file) and the line
657 parameters are

```
658     isotop_id = 1
659     nuij = 13000.816219 (cm-1)
660     Sij = 2.708e-27 (cm-1/(molec cm-2))
661     gamma_air = 0.04580 (cm-1 atm-1)
662     gamma_self = 0.047 (cm-1 atm-1)
663     Epp = 1814.01040 (cm-1)
664     n_air = 0.67 (unitless)
665     delta_air = -0.007400 (cm-1 atm-1)
```

666 Negative `delta_air` means the center of the line is shifted towards the lower wavenumber ν
667 (“left”) in air w.r.t. its position in vacuum. Despite the simplicity, it is recommended to plot, e.g.,
668 line intensity and check the plots vs. HITRAN online tool (*Hill*, 2016) or figures reported in
669 literature (*Rothman*, 2003: Fig.2; 2013: Fig.5; *Gordon*, 2017: Figs. 5, 6, 8; 2022: Fig. 5). The
670 latter references also compare molecules from different HITRAN versions.

671 [4.2 Molparam.txt and TIPS q-files.](#)

672 The other two HITRAN files are `molparams.txt` and `TIPS.txt`. For all HITRAN
673 molecules, `molparam.txt` contains a global ID molecule code (not used in this paper), the
674 isotope abundance for the Earth environment (note again, `Sij` is already scaled by this), the total
675 internal partition sum (TIPS) $Q(296)$ (explained later) at the reference temperature $T = 296^\circ (K)$,
676 the statistical weight g_j (not used in this paper), and the molar mass (in grams). In our codes, we
677 moved all necessary information from `molparam.txt` file to the header `const_param.h`.
678 Considering O_2 as an example, the content of the `molparam.txt` file³⁹

Molecule #	Iso Abundance	$Q(296K)$	g_j	Molar Mass (g)
O_2 (7)				
66	9.95262E-01	2.1573E+02	1	31.989830
68	3.99141E-03	4.5523E+02	1	33.994076
67	7.42235E-04	2.6581E+03	6	32.994045

684 corresponds to the following in `const_param.h`:

```
685     // (7) O2:
```

³⁹ To be exact, we used information from this page <https://hitran.org/docs/iso-meta/>, instead of the `.txt` file.

```

686     int const niso_o2 = 3;
687     char const fname_iso_o2[niso_o2][fname_len_max] =
688         {"q36.txt", "q37.txt", "q38.txt"};
689     double const
690         Qref_o2[niso_o2] = {215.73450400, 455.22995200, 2658.12071500},
691         molar_mass_o2[niso_o2] = {31.989830, 33.994076, 32.994045},
692         Ia_iso_o2[niso_o2] = {9.95262e-1, 3.99141e-3, 7.42235e-4};

693 Here niso_o2 is the number of isotopes, Qref_o2 are the TIPS at the reference temperature
694  $T_{ref} = 296^{\circ}(K)$ , molar_mass_o2 are the isotope molar masses, and the isotope abundances are
695 Ia_iso_o2. Note that the isotope ID number, isotope_id, which one reads from the
696 HITRAN *.par file, is used in our codes as an index to get the appropriate isotope parameters
697 from the mentioned arrays. It is therefore easy to add a new isotope by adjusting the total number
698 of isotopes and updating the arrays with new parameters. One must keep in mind that the
699 HITRAN isotope number is a unit offset integer, contrary to the C-array zero offset indexing.

700 The array fname_iso_o2, contains the file names with TIPS precomputed in a wide range of
701 temperatures  $T$  from a few degrees to a few thousand (Laraia, 2011; Gamache 2017, 2021). The
702 TIPS describes statistical properties of gas in thermodynamic equilibrium. In particular, the
703 number of molecules (population) at different energy states  $E_i$  which in its turn determines the
704 transition intensity of a line,  $S_{ij}$ . Since the dependence of the line intensity on TIPS is linear, the
705 TIPS ratio is used to scale the intensity from the value at the reference temperature,  $T_{ref} = 296^{\circ}$ 
706 ( $K$ ) to an arbitrary one.

707 Each q-file contains only two columns: left is temperature  $T (K)$  in increasing order with equal
708 step  $\Delta T = 1^{\circ} (K)$ , right is the TIPS value  $Q(T)$ . This is convenient for reading and interpolation.
709 Each q-file name is based on the global isotope ID. For example, for the oxygen, isotope_id
710 = 1, the corresponding TIPS file q36.txt in line 296 reads 215.73450400, which is the TIPS
711 value at the reference temperature Q(296°K).

712 Aspect and gcell, use special functions for the isotope data. In gcell it is

713     niso = isotops(molec_id, T_kelvin, Qratio, mmass_iso, Ia_iso);

714 Using molec_id, and a given temperature T_kelvin, the function returns the total number
715 of isotopes niso for the given molecule, ratio of TIPS  $Q(T_{ref})/Q(T)$ , the molar mass and

```

716 abundances for all niso isotopes (hence all these output parameters are arrays). In aspect,
 717 this function is slightly different because of the variation of temperature with height –
 718 hisotops (...) .
 719 Specifically, based on `molec_id`, the `isotops` (...) function decides what isotopes to read
 720 from `const_param.h`

```
721     switch (molec_id)
722     {
723         ...
724         case 7: // O2
725             niso = niso_o2;
726             for (iso = 0; iso < niso; iso++)
727             {
728                 Qref[iso] = Qref_o2[iso];
729                 mmass_iso[iso] = molar_mass_o2[iso];
730                 Ia_iso[iso] = Ia_iso_o2[iso];
731                 strcpy(fname_iso[iso], fname_iso_o2[iso]);
732             } // for iso
733             break;
734         ...
735     } // switch (molec_id)
```

736 Then, for each isotope, the function opens an appropriate `qXY.txt` TIPS file, reads it
 737 consecutively until the range of temperatures for `T_kelvin` is found, interpolates TIPS linearly
 738 and calculates the TIPS ratio

```
739     for (iso = 0; iso < niso; iso++)
740     {
741         strcpy(fpath, path_TIPS);
742         strcat(fpath, fname_iso[iso]);
743         fin = fopen(fpath, "r");
744         fscanf(fin, "%lf %lf", &T2, &Q2);
745         while (T2 < T_kelvin)
746         {
747             T1 = T2;
748             Q1 = Q2;
749             fscanf(fin, "%lf %lf", &T2, &Q2);
750         } // while T2 < T_kelvin
751         Q = Q1 + (T_kelvin - T1) * (Q2 - Q1) / (T2 - T1);
```

```

752     Qratio[iso] = Qref[iso]/Q;
753     fclose(fin);
754 } // for iso

755 This straightforward, but not the most efficient way, could be improved by: (a) reducing the
756 range of  $T$  (K) in the qXY.txt files to that typically found in the Earth atmosphere; (b)
757 converting the qXY.txt files from ASCII to an array in header (e.g., in const_param.h) –
758 this will allow to immediately find indices of the interval containing T_kelvin; (c) avoid files
759 by coding an explicit expression for  $Q(T)$  (Rothman, 1998: p.695), or by using these Fortran or
760 Python programs40. As we will see later, the performance of this subroutine is not a bottleneck.
761 Because of that, and to avoid unnecessary alteration of the default HITRAN qXY.txt file, we
762 use this simple LUT-based solution with consecutive search for the gas cell calculations.

```

763 4.3 Basic code for a single line

764 Now we are ready for calculation of the absorption cross section, k ($cm^2/molec$), in a gas cell. So
765 far, we keep the abovementioned `*.par` file with one oxygen record. All commands in this
766 section are operators of the `main(...)` function located in the `main_gcell.cpp` file.

767 For numerical calculations the user defines the following parameters:

768 nu – wavenumber to compute the absorption coefficient (cm^{-1});

769 `T_kelvin` – gas temperature (K);

770 `p_atm` – gas pressure (atm).

771 The first step is to compute the center of the spectra line ν_{ij}^{pshift} as it shifts w.r.t. its position in
772 vacuum ν_{ij} due to user specified pressure P (atm) assumed constant – like in a gas cell or at a
773 given level in the atmosphere (same for temperature and gas concentrations)

$$774 \nu_{ij}^{pshift} = \nu_{ij}(P) = \nu_{ij} + \delta_{air} P \quad (1)$$

775 `nuij_pshift = nuij + delta_air*p_atm;`
776 `13000.808819 = 13000.816219 + (-0.007400) *1`

⁴⁰ <https://hitran.org/suppl/TIPS/TIPS2021/>

777 $cm^{-1} = cm^{-1} + cm^{-1}/atm \cdot atm$. Next, the intensity of the spectral line is scaled from the reference
 778 temperature $T_{ref} = 296^\circ (K)$ to the user-defined one. This step requires calculation of several
 779 exponential functions which can be combined to reduce the number of calls to the
 780 computationally expensive `exp()` function. However, it would make the code less readable
 781 and does not provide much gain in performance.

782 $e_{11} = \exp(-c_2 E''/T)$ (2)

783 `e11 = exp(-c2_rad*Epp/T_kelvin);`
 784 `0.00016661 ≈ exp(-1.438777*1814.01040/300.0);`
 785

786 $e_{21} = \exp(-c_2 E''/T_{ref})$ (3)

787 `e21 = exp(-c2_rad*Epp/T_ref);`
 788 `0.00014813 ≈ exp(-1.438777*1814.01040/296.0);`
 789

790 $e_{12} = 1 - \exp(-c_2 v_{ij}^{pshift}/T)$ (4)

791 `e12 = 1.0 - exp(-c2_rad*nuij_pshift/T_kelvin);`
 792 `1.0 ≈ 1.0 - exp(-1.438777*13000.808819/300.0);`
 793

794 $e_{22} = 1 - \exp(-c_2 v_{ij}^{pshift}/T_{ref})$ (5)

795 `e22 = 1.0 - exp(-c2_rad*nuij_pshift/T_ref);`
 796 `1.0 ≈ 1.0 - exp(-1.438777*13000.808819/296.0).`

797 In Eqs.(2)-(5), $c_2 = hc/k \approx 1.44 (cm \cdot K)$ is the second black body radiation constant. Given its
 798 value, the spectral boundary for atmospheric remote sensing in the solar region, $\lambda_{max} \sim 2.5 (\mu m)$
 799 or $v_{min} \sim 4000 (cm^{-1})$, and the highest value temperature within $z = 0 \dots 120 (km)$ $T_{max} \sim 350^\circ (K)$,
 800 both exponents in Eqs.(4) and (5) vanish. We preserve these terms for a tutorial, rather than
 801 numerical reason, but note that they can be safely dropped for the Earth atmosphere remote
 802 sensing leveraging scattered sunlight. Also we note, that the two equations rely on Eq.(1).
 803 Apparently, similar equations in the HITRAN and BYTRAN manuals contain a typo: unshifted v
 804 is used in both.

805 With Eqs.(2) - (5), one calculates the temperature-affected intensity of the spectral line as

806
$$S_{ij}(T) = S_{ij}Q_{ratio}(T) \frac{e_{11}}{e_{21}} \frac{e_{12}}{e_{22}} \quad (6)$$

807 $S_{ijT} = S_{ij} * Q_{ratio} * e_{11} * e_{12} / e_{21} / e_{22}$
808 $3.005168e-27 \approx 2.708e-27 * 0.98664770 * 0.00016661 * 1.0 / 0.00014813 / 1.0$
809 $[S_{ijT}] = [S_{ij}]$

810 In Eq.(6), $Q_{ratio}(T)$ is the ratio of total internal partition functions Q at the reference and user-
811 defined temperatures $Q(T_{ref})/Q(T)$ (note T_{ref} is in the numerator). As stated previously, by
812 default the HITRAN line intensity S_{ij} is already scaled by the isotope abundance typical for the
813 Earth environment, so users need make no changes.

814 In addition to the intensity, the line width is also affected by temperature and pressure. It is
815 common to account for two effects contributing to the line broadening: the Doppler component
816 and the Lorentzian component. The Doppler thermal (Brownian) motion broadening is caused by
817 the Doppler effect of change of frequency of wave when the source of light (an emitting
818 molecule) moves w.r.t. the observer. Kirchhoff's law requires the same change to happen for an
819 absorbing molecule. The Doppler line shape is modeled by the Gaussian distribution with the
820 following HWHM parameter

821
$$\alpha_D = \frac{v_{ij}^{pshift}}{c} \sqrt{\frac{2N_A k T \ln(2)}{m_{iso}}} \quad (7)$$

822 $\text{alf_doppler} = \text{nuij_pshift} * \sqrt{2.0 * n_avogadro * k_boltzman * T_kelvin * \ln(2) / mmass_iso} / c_light;$
823 $0.014257689 \approx 13000.808819 * \sqrt{2.0 * 6.02214129e+23 * 1.3806488e-16 * 300.0 * \ln(2) / 31.98983} / 29979245800.0$

827 The Lorentzian-broadening accounts for the natural broadening (finite radiative lifetime makes
828 an excited atom eventually emit radiation) and collision/pressure broadening (emission of
829 radiation by an excited atom when colliding against another atom of the same – self component –
830 or another – foreign component – type). Again, Kirchhoff's law requires the same energy
831 transition to happen during absorption. The HWHM parameter for Lorentzian effects is

832
$$\gamma_L = \left(\frac{T_{296}}{T} \right)^{n_{air}} \left(\gamma_{air} (P_{total} - P_{self}) + \gamma_{self} P_{self} \right) \quad (8)$$

833 `gam_lorentz = pow(T_ref/T_kelvin, n_air) *`
 834 `(gamma_air*(p_tot - p_atm) + gamma_self*p_atm);`
 835 `0.046579204 ~`
 836 `(296.0/300.0)^0.670* (0.04580*(1.0 - 1.0) + 0.047*1.0)`

837 In Eq.(8), P_{self} is the partial pressure of the gas. In the case of the gas cell, it coincides with the
 838 total pressure and only self-broadening takes place: $P_{total} = P_{self}$ and the parameter γ_{air} becomes
 839 irrelevant. However, if the user slightly modifies input to provide the total and the partial
 840 pressures, the `gcell` code can be used for simulation of absorption along horizontal path in
 841 atmosphere that contains mixture of gases or in gas cell containing the same.

842 The Doppler and Lorentzian broadenings take place together and their combined effect is
 843 expressed as a convolution of the respective line shapes, resulting in the Voigt line shape model.
 844 This is an important step for modeling of the physics of the absorption process. Also, calculation
 845 of the Voigt contour is the most time-consuming step in both our codes. For these reasons, we
 846 consider details of the Voigt spectrum in a separate section.

847 [4.4 Convolution – Voigt spectrum](#)

848 The Voigt spectrum model is a result of the Lorentzian or pressure-broadening, that dominates in
 849 the lower atmosphere, and speed-dependent Doppler-broadening that dominates at higher
 850 temperatures and lower pressure (*van de Hulst & Reesinck*, 1947). Both are simulated by the
 851 normalized (unit integral over the wavenumber, v) line shape functions. Like in Eqs. (7) - (8), we
 852 use subscripts L and D for the Lorentz and Doppler functions, respectively:

853
$$f_L(v - v_{ij}^*) = \frac{1}{\pi} \frac{\gamma_L}{\gamma_L^2 - (v - v_{ij}^*)^2}, \quad (9)$$

854
$$f_D(v - v_{ij}^*) = \sqrt{\frac{\ln 2}{\pi \alpha_D^2}} \exp\left(-\frac{(v - v_{ij}^*)^2 \ln 2}{\alpha_D^2}\right). \quad (10)$$

855 For simplicity, Eqs. (9) - (10) do not show T and p as arguments and indicate that the line shapes
 856 depend on distance between a given wavenumber v and the line center v_{ij}^* pressure-shifted

857 according to Eq. (1). **Figure 2** schematically shows mutual broadening of the lines when the two
 858 effects take place at the same time.

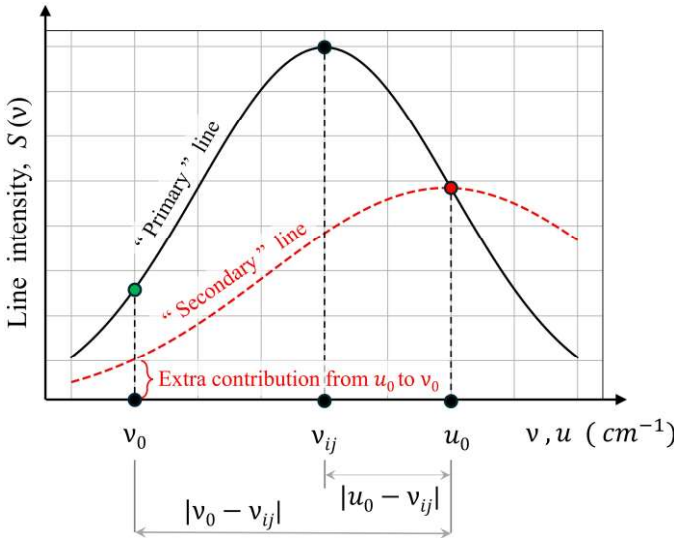


Fig.2: Schematic representation of “primary” line shape broadened by “secondary” one. Contribution at wavenumber v_0 comes not only from the “primary” line, centered at v_{ij} , but also from another wavenumber u_0 acting as a center of the secondary line. All points u_0 contribute to all points v_0 , hence both are in fact continuous variables u (for integration) and v (wavenumber space):

$$f_V(v) = \int_{-\infty}^{+\infty} f_L(v-u) f_D(u) du .$$

See the main text for details.

859
 860 Suppose we wish to calculate the line shape at a wavenumber v considering the fact that
 861 wavenumbers u also contribute to v due to broadening. Assuming the Doppler line as the primary
 862 one, we calculate the line intensity at u exactly as Eq.(10) shows

$$863 \quad f_D(u) = \sqrt{\frac{\ln 2}{\pi \alpha_D^2}} \exp\left(-\frac{(u - v_{ij}^*)^2 \ln 2}{\alpha_D^2}\right). \quad (11)$$

864 Eq.(11) is for the black solid line (**Fig.2**) centered at the HITRAN’s pressure-shifted v_{ij}^* . It is not
 865 indicated as the function argument because it is a constant parameter. Now, this line intensity
 866 $f_D(u)$ acts as a “secondary” line contributing to v via Lorentzian broadening,

$$867 \quad f_L(v-u) = \frac{1}{\pi} \frac{\gamma_L}{\gamma_L^2 - (v-u)^2} . \quad (12)$$

868 In Eq.(12), we note a new line center, u . One accumulates the contribution from all points u to v
 869 by integration:

$$870 \quad f_V(v) = (f_L * f_D)(v) = \int_{-\infty}^{+\infty} f_L(v-u) f_D(u) du . \quad (13)$$

871 Eq.(13) is a convolution (*) of two functions, which commutativity tells that it is not important
 872 what line is called “primary”. Also, negative wavenumbers are unphysical. However, we are far
 873 from wavenumbers close to zero and the line shapes attenuate quickly, within $\sim 20-25$ (cm^{-1}) in
 874 our band of interest. For mathematical reasons, which we consider shortly, it is beneficial to use
 875 the limits as in Eq.(13).

876 Eqs.(11) - (13) and an appropriate linear scaling of the integration variable u yields

$$877 f_V(v) = \sqrt{\frac{\ln 2}{\pi \alpha_D^2}} \frac{\gamma_L}{\pi} \int_{-\infty}^{+\infty} \frac{1}{\gamma_L^2 - (v-u)^2} \exp\left(-\frac{(u-v_{ij}^*)^2 \ln 2}{\alpha_D^2}\right) du = \sqrt{\frac{\ln 2}{\pi \alpha_D^2}} K(x, y), \quad (14)$$

878 where

$$879 K(x, y) = \frac{y}{\pi} \int_{-\infty}^{+\infty} \frac{\exp(-t^2)}{y + (x-t)^2} dt, \quad x = \frac{\sqrt{\ln 2}}{\alpha_D} (v - v_{ij}^*), \quad y = \frac{\sqrt{\ln 2}}{\alpha_D} \gamma_L. \quad (15)$$

880 Code `gcell` implements calculation of the Voigt line shape, Eq.(15), in a straightforward
 881 manner, i.e. making commands look similar to what is published in literature. In the code snippet
 882 below we deliberately hide operators explained earlier and show only those corresponding to
 883 Eqs.(14)-(15).

```
884     nuij_pshift = ...; // Eq. (1)
885     alf_doppler = ...; // Eq. (7)
886     gam_lorentz = ...; // Eq. (8)
887     y = sqrt_ln2*gam_lorentz/alf_doppler; // Eq. (15)
888     e11 = ...; // Eq. (2)
889     e21 = ...; // Eq. (3)
890     e12 = ...; // Eq. (4)
891     e22 = ...; // Eq. (5)
892     SijT = ...; // Eq. (6)
893     for (inu = inu1; inu < inu2+1; inu++)
894     {
895         x = sqrt_ln2*fabs(nu[inu] - nuij_pshift)/alf_doppler; // Eq. (15)
896         k_abs[inu] = SijT*(sqrt_ln2/sqrt_pi)*
897                     humlicek(x, y)/alf_doppler; //Eqs. (14)-(16)
898     } // inu = inu1 : inu2
```

899 We use the loop over `inu` to calculate absorption cross-section on the user’s grid of the
 900 wavenumbers `nu[inu]`

901 $k_{ij}(v, T, p) = S_{ij}(T) f_V(v, v_{ij}, T, p).$ (16)

902 Note that absolute value `fabs (nu[inu] - nuij_pshift)` enforces symmetry of the line
 903 shape. However, the symmetry may be violated (see Sec.4.5 below).

904 *Humlíček* (1982) developed an algorithm for calculation of $K(x, y)$, Eq.(15), with reported
 905 relative error not exceeding 10^{-4} and published a corresponding FORTRAN function. Despite
 906 using complex arithmetic, the function contains only 30 lines, including 7 comments and 7 non-
 907 executable lines: `FUNCTION`, 4 `RETURN-s`, `END` statements and one line with definition of 3
 908 local variables and the function output. Another 7 lines are mostly filled with precomputed
 909 values for 3 different “regions” of input parameters, accurate numerical evaluation of which is
 910 the main topic of that paper. A vectorized version of this subroutine (*Schreier*, 1992: Appendix
 911 2) was translated into C (*Lyapustin*, 2002: function `humlicek(...)`), which we borrow for use
 912 in `gcell` and `aspect`.

913 Strictly speaking, calculation of $K(x, y)$ is of general mathematical nature, rather than
 914 spectroscopy (like calculation of weights for Gaussian quadrature or Legendre polynomials for
 915 use in multiple scattering of light). Therefore, for confident use of the `humlicek(...)` function it
 916 is sufficient to understand its input, x and y , Eq.(15). Here we only note that (a) *Humlíček* (1982:
 917 Eq.(1)) considered the entire complex probability function from which the Voigt line shape
 918 needs only the real part; and (b) calculation of the Voigt line shape is the slowest part of our code
 919 (takes $\sim 90\%$ of the runtime). *Schreier* (1992) compared accuracy and runtime for several
 920 techniques for computation of the Voigt function. It was found that depending on the method, the
 921 computational speed for the Voigt function varies by 2 orders of magnitude, even after code
 922 optimization. The *Humlíček* (1982) algorithm was found as overall best based on accuracy,
 923 speed, and flexibility (*Schreier*, 1992: p.760). We have used it for decades (*Lyapustin*, 2002) and
 924 stick to it in this paper.

925 However, “*accurate yet efficient computation of the Voigt ... function is a challenge*” (*Schreier*,
 926 2018(a): Abstract). *Kuntz* (1997), with corrections by *Ruyten* (2004), offered a new numerical
 927 implementation of the *Humlíček* algorithm. Depending on a computer architecture, a factor of 1.2
 928 – 3.3 in acceleration was reported. Apart from computational efficiency, *Mohankumar & Sen*
 929 (2019) evaluated the Voight function with a 30-digit accuracy for reference purposes using

930 trapezoidal integration, residue correction, and quadruple precision. Corresponding FORTRAN
931 code and coefficients are reported in their paper.

932 Depending on application, it could be possible to use either Eq.(11) or Eq.(12) and avoid the
933 time-consuming Voigt convolution, Eq.(13). Alternatively, the Voigt effect can be simulated
934 approximately by a rectangular core (central) part and v^2 - shaped wings (Fels, 1979), or using
935 analytical, hence fast, approximations, e.g., as a sum of the Lorentzian profiles (McLean *et al.*,
936 1994: see Appendix for codes in C that approximately calculate the Voigt function and parameter
937 derivatives). However, one must follow the analytical path with caution (Schreier, 2018b). Wells
938 (1999) discuss an approximate algorithm tailored for atmospheric line-by-line calculations,
939 which is efficient “*if the maximum relative error criteria can be relaxed*” (Abstract). It was
940 suggested to express the algorithm in real arithmetic, use a simple analytical expression for a
941 new “region” far from the line center, redefine boundaries of the regions (Wells, 1999: p.33). In
942 the Appendix to Wells (1999), one finds codes in FORTRAN77 for calculation of the Voigt
943 spectrum in SUBROUTINE HUMLIK (...), and derivatives $\partial K(x, y)/\partial x$ and $\partial K(x, y)/\partial y$ in
944 SUBROUTINE HUMDEV (...). The Voigt code is longer than that of Humlíček (1982), also based
945 on many precalculated numerical parameters, and yields a user-controlled accuracy. Abrarov &
946 Quine (2015) approximate the Voigt function as an analytical – hence fast – series expansion
947 (see their Eq.(17)). Their MATLAB code (in Appendix) also relies on a set of precomputed
948 coefficients. For broadband atmospheric radiative transfer, Nordebo (2021) suggested replacing
949 the Voigt with the Lorentzian calculation, but on the bounds altered as described in the paper,
950 and based on the dominating role of the far wings of spectral lines in calculation of atmospheric
951 transmittance.

952 This sparse literature review indicates that calculation of the Voigt function, despite decades of
953 use, may be problematic. On top of that comes the fact that under some conditions the Voigt line
954 shape model may not be physically sufficient. Although our paper does not go “beyond Voigt”,
955 we feel obligated to say a few words supported by references.

956 [4.5 Beyond Voigt: a few legacy and recent references](#)

957 The Voigt line shape as convolution of the Doppler and Lorentzian contours, is only a model. Its
958 limitations come, e.g., from the assumption of ideal gas to simulate elastic molecular collisions.
959 In fact, the speed of molecules decreases at collision, so does the Doppler effect, causing

960 “collision narrowing” of spectral lines and increasing absorption at the line centers – the *Dicke*
961 (1953) effect⁴¹. Back in 1960’s *Galatry* (1961) and *Rautian & Sobel’man* (1967) gave a non-
962 Voigt expression for a spectral line accounting for the effect of change of speed on the line
963 shape. This effect is most important for simulation of laser light absorption by narrow lines.
964 Likewise, the Lorentzian model works well near the center of spectral lines, where absorption is
965 high, but less accurate at the line wings. Lower absorption in the wings is important for remote
966 sensing in atmospheric windows. This effect is often accounted for as continuum (see references
967 in the Introduction), based on measurements, and most important for broad lines in the
968 microwave region. Like for the Doppler model, “generalized” Lorentzian contours exist. Two
969 examples are the *van Vleck – Weisskopf* line shape and the *Benedict* scaling of the wings that
970 reduces absorption (*Goody & Yung*, 1989: p.110, Eqs.(3.52) and (3.75), respectively).
971 HITRANonline⁴² notes that “*the line shape function for many applications is much more*
972 *complex*”. The new line shape functions with better simulation of molecular collision are being
973 applied, while the Voigt model for computation of radiative parameters pertains today to a “*not-*
974 *so-distant past*”. Indeed, literature has used the term “beyond Voigt” (*Ngo et al.*, 2013, 2014;
975 *Wcislo et al.*, 2021) for cases where the Voight model is not satisfactory.
976 *Spänkuch* (1989) reviewed methods compensating deviations from the Lorentzian line shape.
977 *Boone et al.* (2007) claims that “*the Voigt profile does not provide a sufficiently accurate*
978 *representation of the line shape for air-broadened H₂O vapor over a significant range of*
979 *conditions commonly encountered in atmospheric remote sensing*” – although “sufficiently
980 accurate” depends on the end user’s individual application. They offer a speed-dependent Voigt
981 profile for analysis of infrared measurements collected by the Atmospheric Chemistry
982 Experiment (ACE) mission. A FORTRAN code for their line mixing approach, used in ACE, is
983 publicly available from the journal website (*Boone et al.*, 2011).
984 The need for accurate modeling of the high-resolution spectral measurements spawned general
985 terms like non-Voigt, beyond Voigt, speed-dependent Voigt, line-mixing, and Rautian profiles
986 (*Ngo et al.*, 2013; *Schreier & Hochstafel*, 2021; *Tran et al.*, 2013). Relevant, but more specific

⁴¹ https://en.wikipedia.org/wiki/Dicke_effect

⁴² <https://hitran.org/docs/definitions-and-units/> (see between Eqs. (9) and (10))

987 terms, found in literature are “partially-correlated quadratic-speed-dependent hard-collision
988 profile (pCqSD-HCP)” and “quadratic speed dependent Voigt profile (qSDV)” (*Tran et al.*,
989 2013). An open-source FORTRAN code is available for *Tran et al.*, (2013) from the journal
990 website. A typo in theoretical evaluations in *Ngo et al.*, (2013) and *Tran et al.*, (2013) was
991 corrected in *Tran et al.*, (2014). In order to accurately capture the influence of pressure on line
992 shape in high-resolution spectra (of water), the IUPAC Task Group recommends replacing the
993 Voigt profile with use the pCqSD-HCP and call it the Hartmann-Tran profile for simplicity
994 (*Tennyson et al.*, 2014). *Domyslawska et al.* (2016) presented laboratory measurements of the
995 oxygen B-band at low pressure (to make lines narrow). They used the qSDV-profile to simulate
996 the speed-dependence of collisional broadening and shifting of the Voigt shape. *Schreier* (2017)
997 analyzed different numerical approaches to calculation of the speed-dependent Voigt profile and
998 suggested his own technique.

999 As a result of these studies, “beyond-Voigt” line shape parameters have been introduced into
1000 HITRAN (*Wcislo et al.*, 2021) for certain molecules and lines. However, for most molecules in
1001 atmospheric applications, the Voigt line model simulated is still the baseline⁴³. Determining the
1002 need to go beyond-Voigt in remote sensing of the atmosphere is a separate problem. How
1003 important is it for the UV-Vis-NIR bands? What molecules are affected? For what temperature
1004 and pressure? We consider this beyond the scope of the present study but mention all that to
1005 prepare the reader for potential changes in standard practice soon. At present, we limited
1006 ourselves with a well-tested *Humlíček* algorithm explained in the relevant open source codes, and
1007 provided reference for further reading.

1008 4.6 A few numbers for validation of code for an isolated line

1009 In Sec.2 we noted that finding reliable (accurate and reproducible) numerical results to test the
1010 final output, not to mention unit testing, was not easy. It is, of course, possible to use tools like
1011 HAPI. But if results do not match, the developer is left with a question: “does my software have
1012 an error, or have I misunderstood the benchmark tool?”. It is therefore desirable to tabulate some
1013 numbers, like we did in Sec.4 above and earlier in Sec.3.2.2, for a clearly defined input.

⁴³ <https://hitran.org/docs/definitions-and-units/>

1014 For checking purposes, here we plot the oxygen isotope #1 for 3 temperatures, $T = 270, 300, 330$
 1015 ($^{\circ}\text{K}$) at fixed pressure $p = 1$ (atm) and, vice versa, for 3 pressures $p = 0.9, 1, 1.1$ (atm) at a fixed T
 1016 = 300° (K).

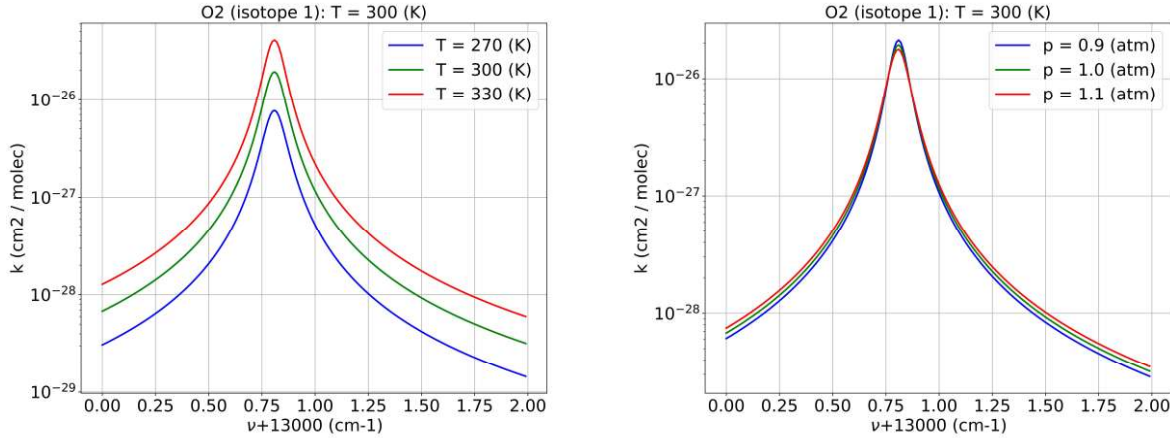


Fig.3: Dependence of the $k(v)$ shape on variation of T (left) and p (right) within 10% w.r.t. nominal values $T = 300^{\circ}$ (K), $p = 1$ (atm). See **Table 4** for a few benchmark numbers at the peak.

1017
 1018 Although the equations and the code described so far are simple this intermediate benchmark
 1019 helps catch typos, e.g. the commonly encountered wrong order of magnitude caused by wrong
 1020 units. It also leads to a better understanding of the physical background. For example, higher
 1021 temperature causes higher absorption, and the dependence is strong. But for pressure, the
 1022 dependence at the peak is the opposite and overall it is much weaker. **Table 4** shows some
 1023 reference numbers for the absorption cross-section, k (cm^2/molec), and for input defined in
 1024 Sec.4.1.

1025

1026 **Table 4:** The peak values for 6 curves shown in **Fig.3**. Because of the wavenumber grid step $\Delta v = 0.01$
 1027 (cm^{-1}), the shown peak values are at $v = 13000.81$ (cm^{-1}), which may not precisely coincide with the actual
 1028 maximum value of the spectral line. Columns, left to right, indicate pressure p (atm), location of the
 1029 maximum value of the line, Eq.(1), and three temperatures T (K).

p (atm)	$v(p)$ (cm^{-1})	$T = 270$ (K)	$T = 300$ (K)	$T = 330$ (K)
0.9	13000.809559	-	2.125930E-26	-
1.0	13000.808819	7.711446E-27	1.935411E-26	4.082727E-26
1.1	13000.808079	-	1.774578E-26	-

1030

1031 Calculation of the optical thickness and transmittance requires scaling of the cross-section by
1032 number of particles in the gas cell. In the next chapter, we calculate absorption cross-section by
1033 multiple lines of the same gas, O₂ and separately CH₄ (all isotopes), compute spectral
1034 dependence of $\tau(\lambda)$, spectral transmittance $T(\lambda) = \exp(-\tau(\lambda))$, and compare our numerical results
1035 with a few published experiments.

1036 5. Calculation of absorption in a gas cell

1037 This section shows how to calculate the absorption cross-section k ($cm^2/molec$), optical thickness
1038 τ , and transmittance $T(v)$ for a group of spectral lines at a given temperature and pressure.
1039 Practically this scenario corresponds to simulation of absorption of light in a gas cell in
1040 laboratories and remote sensing systems. As a prerequisite, we assume the user has downloaded
1041 the HITRAN database files in the current 160-character ASCII format and compiled the package
1042 in the `gcell` mode (see Sec.3.2.1 and **Fig.1(a)**).

1043 For the gas cell scenario, the user's input is

1044 `molec_id` – molecule as numbered in HITRAN: 1-7 and 10 in the current version.

1045 `T_kelvin` – gas temperature in Kelvins (K);

1046 `p_atm` – gas pressure in atmospheres (*atm*);

1047 `l_cm` – length of the gas cell in centimeters (*cm*);

1048 `nu_usr_min` – lower boundary for the desired wavenumber spectral range (cm^{-1});

1049 `nu_usr_max` – upper boundary for the same (cm^{-1});

1050 `dnu` – wavenumber spectral resolution (cm^{-1}).

1051 Using these parameters, in the next 3 parts, we begin by reading the HITRAN database, then we
1052 accumulate absorption from a group of spectral lines, and finally we test the result. Some steps
1053 are the same for the atmospheric and the gas cell computations. We refer to these as
1054 `aspect/gcell`; otherwise, we use `gcell`. Sec.5.1 and 5.2 show commands from the
1055 `main(...)` functions located in the `main_gcell.cpp` and `main_aspect.cpp` respectively
1056 for the `gcell` and `aspect` modes.

1057 5.1 Picking necessary lines from the HITRAN *.par files

1058 After reading the input data with `read_hitran160(...)` in Sec. 4.1 above, `aspect/gcell`
 1059 determines boundaries of the HITRAN spectral interval which lines contribute to the user
 1060 defined interval either directly (the HITRAN line center belongs to the user interval) or via line
 1061 wings – an “extended” spectral interval:

```
1062     nu_hit_min = nu_usr_min - delta_nu;
1063     nu_hit_max = nu_usr_max + delta_nu;
```

1064 Following the common practice, we use $\Delta\nu = 25$ (cm^{-1}) for `delta_nu` (see Introduction).

1065 Next, using these extended interval boundaries, `aspect/gcell` computes the number of the
 1066 pertaining HITRAN records, `nlines`, and location of the first contributing line in the HITRAN
 1067 *.par file `iline0` - both are output parameters of this function:

```
1068     count_lines(molec_id, nu_hit_min, nu_hit_max, iline0, nlines);
```

1069 Based on the value of `molec_id`, the function reads an appropriate *.par file sequentially
 1070 from the beginning (lowest wavenumber). The number of the very first detected line that belongs
 1071 to the extended spectral interval is saved in `iline0`; the total number of lines is counted and
 1072 saved in `nlines`.

1073 To comply with C’s array indexing, we define `iline0` with zero offset: `iline0 = 0`
 1074 corresponds to the first record in the HITRAN database that contributes to the user spectral
 1075 interval (i.e., belongs to the extended interval). If `count_lines()` finds no lines contributing
 1076 to the extended interval, it returns `iline0 = nlines = 0`. The `nlines` parameter yields
 1077 memory allocation for parameters of all spectral lines. E.g., for H₂O in the interval $\lambda = [0.25,$
 1078 $2.5]$ (μm) or $\nu = [4000, 40000]$ (cm^{-1}), `nlines = 205134` (in HITRAN 2020). That many
 1079 double precision floating point numbers occupy ~ 1.6 Mb of memory. **Table 3** above shows that
 1080 `aspect/gcell` store the HITRAN parameters in 7 arrays of the mentioned size and 1 integer
 1081 32-bits array. Thus, storing all necessary HITRAN parameters in memory for intermediate
 1082 calculations is not a problem even for a wide band. It is the output that consumes memory most.
 1083 Especially if one needs wide band, and high resolution over both wavenumber and height grids.
 1084 We return to that problem later in Sec. 6.4 for aspect mode.

1085 Allocation of 8 arrays to store parameters for each line and reading the HITRAN database has
1086 already been discussed in Sec.4.1 and 4.2. After that, `gcell` reads information about isotopes
1087 using the `isotops (...)` function, while `aspect` uses similar function `hisotops (...)` because
1088 of dependence of the TIPS ratio on height via temperature. Once completed, `aspect/gcell`
1089 proceed to the next step – simulation of a single line shape and accumulation of contribution
1090 from different lines.

1091 [5.2 The line-mixing effect, which we also neglect](#)

1092 Quoting from *Tonkov et al.* (1996: Abstract) “*It is well known that, due to line mixing effects,
1093 spectral regions with overlapping lines cannot be described by the sum of separate profiles*”.
1094 Indeed, in general, the overlapping lines interfere with each other, changing the shape of the
1095 Lorentz contour (*Goody & Yung*, 1989; *Liou*, 2002). This effect is important in some lines of
1096 CO₂, CH₄, O₂ absorption in the microwave and in the A- bands, and O₃ in the IR, when the
1097 HWHM is comparable or exceeds distance between them.

1098 *Tran et al.* (2006) considers the line mixing effect, combined with collision induced absorption
1099 (CIA), in the O₂A band at high pressure, 20-200 (*atm*), and temperature 200°-300° (*K*) for both
1100 pure O₂ and O₂-N₂ mixtures. They showed that neglecting the line mixing overestimates
1101 absorption in the wings and underestimates absorption at the peaks. Smooth spectral dependence
1102 of the effects allows treating them as “continuum” and model the difference between
1103 measurements and LBL simulation using some convenient fitting function.

1104 *Tran et al.* (2006) used the resulting model and data to build a database and software suitable for
1105 the calculation of oxygen atmospheric (hence, “regular” pressure) absorption and for inclusion in
1106 RT codes. Then, they studied the influences of both line-mixing and collision-induced processes
1107 on atmospheric photon path escape factors and on cloud-top altitude retrievals such as this band
1108 is commonly used for such purposes (e.g. *Sayer et al.*, 2023). They concluded that the mentioned
1109 effects “*make significant contributions and explain a large part of the discrepancies between
1110 measured and calculated atmospheric absorption observed recently*” (in particular, see their
1111 Fig.11 for numerical quantification of the effects). The model was later improved by *Tran &*
1112 *Harztann* (2008: see Fig.1 for influence on transmission at oblique traces) and applied to O₂-
1113 CO₂ mixture by *Vangvichith et al.* (2009), also in the A-band.

1114 Nevertheless, in this paper, we neglect the effect of line coupling for simplicity, and because
1115 HITRAN includes CIA as a separate dataset⁴⁴. We simulate joint contribution of lines via simple
1116 summation of the absorption cross-sections.

1117 [5.3 Simulation of LBL absorption](#)

1118 Using a loop over `nlines` HITRAN records it is easy to account for their joint contribution to
1119 any user-defined wavenumber v by simple accumulation, if the line-mixing effect is ignored

1120
$$k(v) = \sum_l^{nlines} k_l(v, v_l) w(v - v_l) . \quad (17)$$

1121 In Eq.(17), $k(v)$ is the total (accumulated) absorption cross-section at the user defined wavenumber
1122 v , $k_l(v, v_l)$ is the cross-section at the user requested wavenumber v by a line centered at v_l , and the
1123 weight

1124
$$w(v - v_l) = \begin{cases} 1, & \text{if } |v - v_l| \leq 25 \text{ (cm}^{-1}\text{)} \\ 0, & \text{otherwise} \end{cases} \quad (18)$$

1125 instructs to account for contribution only from those HITRAN records located no further than 25
1126 (cm^{-1}) from the user's v (Schreier, 1992: p.760; Lyapustin, 2003: p. p.870). This is standard
1127 practice when line parameters are derived and used to separate line and continuum absorption
1128 (Clough et al. 1981; Burch, 1982; Mlawer et al., 2023). The function `ix1ix2(...)` in
1129 `aspect/gcell` implements Eq.(18) with the following interface

1130 `code = ix1ix2(nuij, delta_nu, nu, nnu, inu1, inu2);`

1131 Namely, it returns indices `inu1` and `inu2` of elements of an array `nu[nnu]` falling within
1132 `delta_nu` from `nuij` and `code = 1` in case of success. If `code = -1` is returned, it means
1133 that all user-defined wavenumbers lie too far from the selected HITRAN record v_l to receive any
1134 significant contribution. The corresponding pseudocode is (see also Sec. 4.4 between Eqs.(15) -
1135 (16))

1136 `for (inu = 0; inu < nnu; inu++)`
1137 `kabs[inu] = 0.0`
1138 `for (iline = 0; iline < nlines; iline++) {`

⁴⁴ <https://hitran.org/cia/>

```

1139     if (ix1ix2(nuij, delta_nu, nu, nnu, inu1, inu2) > 0) {
1140         Calculate nuij_pshift
1141         Calculate Doppler and Lorentz HWHM
1142         Calculate e11, e12, e21, e22
1143         Calculate line intensity Sij
1144         for (inu = inu1; inu < inu2+1; inu++) {
1145             Calculate Voigt spectrum
1146             Accumulate absorption power:
1147             kabs[inu] += (line intensity) * (Voigt)
1148             } // for inu - all wavenumbers affected by iline
1149             } // if iline contributes to nu[]
1150         } // for iline - all HITRAN lines within extended interval

1151 This sequence of loops – over HITRAN lines first, over user’s wavenumbers next – allows to
1152 calculate the HITRAN parameters only once and reuse these for all v-s affected by the line
1153 wings. However, this option forces the user to keep the array kabs [nnu] in memory. This may
1154 cause memory issues if one needs a high spectral and altitude resolutions because the
1155 corresponding array has two dimension kabs [nnu*nkm] (recall, the codes unravel all arrays
1156 to 1D for efficient memory allocation). We briefly discuss this problem with regard to aspect
1157 further in Sec. 6.4.

1158 The monochromatic cross-section,  $k(v, T, p)$  ( $cm^2/molec$ ), is defined per unit column number
1159 density of molecules of the absorbing gas,  $n$  ( $molec/cm^2$ ), at a given temperature and pressure.
1160 The dimensionless absorption optical thickness is

1161  $\tau(v, T, p) = nk(v, T, p)$ . (19)

1162 Using the notation  $V$ ,  $S$ , and  $l$  respectively for the volume, square and length of the column,  $N$  for
1163 the total number of molecules in it,  $k_B$  for the Boltzmann constant, and an assumption of an ideal
1164 gas, one writes

1165  $p = N k_B T / V = n k_B T / l$ . (20)

1166 If the thermodynamic conditions do not change along the path, like in gas cell, the absorption
1167 optical thickness is

1168  $\tau(v, T, p) = \frac{p l}{k_B T} k(v, T, p)$  (21)

```

```

1169 // Note: a) n_column = l_cm * n_volume and b) units conversion
1170 n_column = l_cm*atm_to_cm_g_s*p_atm/(k_boltzman*T_kelvin);
1171 tau[inu] = k_abs[inu]*n_column;

```

1172 The absorption coefficient a (cm^{-1}) is

$$1173 a(v, T, p) = \tau(v, T, p) / l = \frac{p}{k_B T} k(v, T, p). \quad (22)$$

1174 If the thermodynamic conditions vary, e.g., with height h , the absorption optical thickness
1175 between two given heights would be (see Sec. 6.2 for relevant code)

$$1176 \tau(v) = \int_{h_1}^{h_2} a(v, h) dh = \frac{1}{k_B} \int_{h_1}^{h_2} \frac{p(h) k(v, h)}{T(h)} dh. \quad (23)$$

1177 In Eq.(23), the absorption cross-section depends on h via T and p . The monochromatic
1178 transmittance along the path, inclined at zenith angle $\theta = \arccos(\mu)$ w.r.t normal, is

$$1179 T(v, \mu) = \exp(-\tau(v)/\mu). \quad (24)$$

1180 Finally, the spectrally integrated transmittance of the solar light $S(v)$ through a gas cell to a
1181 system with spectral response function (filter) $f(v)$ is

$$1182 T(\mu) = \frac{\int_{\Delta v} T(v, \mu) S(v) f(v) dv}{\int_{\Delta v} S(v) f(v) dv}. \quad (25)$$

1183 Using Eqs.(24) and (25), it is possible to derive a spectrally integrated (efficient) absorption
1184 optical thickness

$$1185 \tau(\Delta v) = -\mu \log(T(\mu)). \quad (26)$$

1186 Note that neither `gcell` nor `aspect` provide transmittance – the user is supposed to calculate
1187 it externally because Eq.(24) is trivial. Also integration in Eq.(25) often requires interpolation
1188 from the HITRAN grid of wavenumbers to that of the Sun or spectral response functions, often
1189 defined as functions of wavelength. In the last part of this section, we report a few benchmark
1190 results for checking purpose.

1191 5.4 Gas cell validation

1192 Spectral calculations often involve hundreds and thousands of numbers which are rarely
1193 published making numerical comparisons difficult. In most cases, precise benchmark is possible
1194 if one uses software developed by others (proper understanding of that software – not only input
1195 - is therefore essential in this case) or ask the developer to generate numbers (which is not
1196 always convenient). Contrary to numerical results, graphical plots for absorption cross-section k
1197 (usually in $cm^2/molec$), absorption coefficient a (cm^{-1} or km^{-1} , depending on application),
1198 absorption optical thickness τ , or corresponding direct transmittance T (both dimensionless) have
1199 been published widely - see, e.g., *Hearn* (1961: Fig.1) for ozone. This simple visual test allows
1200 one to check magnitude (hence units conversion) and overall shape of the spectral dependence of
1201 transmittance, optical thickness, or cross-section. Thus, the key requirement for the published
1202 image is legibility.

1203 *Prischepa* et al. (2023: Fig. 1) shows spectral dependences of absorption coefficients of pure N_2 ,
1204 O_2 , H_2O within 500 - 12000 (cm^{-1}) at normal temperature and pressure. *Karlovets* et al. (2023:
1205 Fig.2) shows absorption coefficient for nitrous oxide, N_2O , measured at pressure 10 (*Torr*), or
1206 ~ 0.013 (*atm*), between 7250 and 7653 (cm^{-1}) and details showing separate lines near 7577 (cm^{-1})
1207 at 2 different scales. Fig.3.21 in *Efremenko & Kokhanovsky* (2021) shows absorption cross-
1208 section of water vapor in a relatively wide 900-1000 (*nm*) and narrow 934-926 (*nm*) bands. Figs.
1209 3.22 and 3.23 in the same show, respectively, absorption cross-section for oxygen A, B, and C-
1210 bands with 610-780 (*nm*), and O_2A band separately. *He* et al. (2019: Figs.1 & 6a) plot HITRAN-
1211 2016 line intensities for O_2 in 600-1300 (*nm*) – a simple but useful intermediate result for visual
1212 unit testing of, e.g., a HITRAN database reader. *Stamnes* et al. (2017: Fig.4.13) shows absorption
1213 coefficient spectrum for the 1510 – 1520 (cm^{-1}) part of the 6.3 (μm) water vapor band at 10
1214 (*mbar*) and 240 (*K*), and at 1 (*bar*) and 296 (*K*) using HITRAN 1982 (!). Transmittance through
1215 1 (*m*) of air at a pressure 150 (*hPa*) and a temperature of 215° (*K*) near 15 ($\mu\mu$), where CO_2 is the
1216 dominant absorber, is shown in *Coakley & Yang* (2014: Fig. 5.4). *Rothman* (2013: Fig.7) plots
1217 absorption cross-section for CH_4 at $T = 296^\circ$ (*K*) with 0.05 (cm^{-1}) resolution. *Bohren & Clothiaux*
1218 (2006) show absorption cross-section of a water molecule for a temperature of 20° (*C*) and a total
1219 pressure of 1 (*atm*) within 12-16 (μm) or 625 - 825 (cm^{-1}) (Fig.2.9); absorption cross-section for
1220 most strongly absorbing atmospheric gases in a wide range 0.1 (μm) - 0.1 (*m*) at 1013 (*mb*) and
1221 294° (*K*) (Fig.2.13); water vapor absorption at 1013 (*mbar*) and 10 (*mbar*) within 1084.7 -

1222 $1085.7\text{ (cm}^{-1}\text{)}$ with and without continuum absorption (Fig.2.19) and combination of the two
1223 (Fig.2.20). *Rothman* (2005: Fig.2) simulates CO_2 laboratory spectra in the $2\text{-}\mu\text{m}$ region at $p = 30$
1224 (torr) and 25 (m) path. *Liou* (2002: Fig.4.5) shows absorption coefficient $k\text{ (atm}\cdot\text{cm)}^{-1}$ within 600
1225 : $0.01 : 700\text{ (cm}^{-1}\text{)}$ at $p = 600\text{ (mbar)}$ and $T = 260^\circ\text{ (K)}$. *Greenblatt* et al. (1990) plot results of
1226 measurement of O_2 absorption for $330\text{-}1140\text{ (nm)}$ (Fig.1) and $675\text{-}800\text{ (nm)}$ (Fig.2) at a high
1227 pressure of 55 (atm) , 196° (K) , and a path length of 89.5 (cm) . This list, by no means exhaustive,
1228 is intended to show that a wide range of reproducible “visual” tests have been published in the
1229 literature.

1230 In this paper, we test `gcell` in two scenarios, one for the oxygen A-band and another one for
1231 methane, described in separate sections below. We use two strategies to test our code. For the A-
1232 band we reproduce published images and test `gcell` “visually”. For methane, we numerically
1233 compare our result vs. independently calculated ones. Unlike broadly published pictures of
1234 spectra and contrary to numerical benchmarks for multiple scattering of radiation, numerical
1235 benchmarks for spectroscopy are rarely available from literature. A code developer has to either
1236 set up and run another code, like HAPI, or extract data from a huge database. Neither is
1237 convenient for quick testing. To help overcome this issue, we provide our numerical results for
1238 both tests in ASCII files together with our source code and report a few more numbers in the
1239 subsequent sections.

1240 5.4.1 Oxygen A-band at 0.764 (\mu m)

1241 The oxygen A-band, commonly shortened as O_2A , is located around $\lambda \approx 0.764\text{ (\mu m)}$: $\Delta\lambda \approx$
1242 $0.760\text{...}0.768\text{ (\mu m)}$, $\Delta\nu \approx 13000\text{...}13160\text{ (cm}^{-1}\text{)}$. We use an O_2A scenario described in *Predoi-*
1243 *Cross* et al., (2008); we will refer to their paper as *P-C* within this section. The spectral
1244 transmittance, Eq.(24), was recorded in a multiple path cell of the total pathlength $l = 1633.6$
1245 (cm), at pressure of $0.724\text{ (bar)} \approx 0.7145\text{ (atm)}$, at the room temperature, with spectral resolution
1246 $0.0222\text{ (cm}^{-1}\text{)}$ (*P-C: Sec.2*). The measurement error of the line intensity is claimed not to exceed
1247 $\sim 1\%$ (*P-C: Abstratct*). The room temperature varied from $\approx 294^\circ\text{ (K)}$ to $\approx 298^\circ\text{ (K)}$ (*P-C: Table 1*).
1248 In our test, we do not intend to simulate the experiment with high precision. So, we use $T = 296^\circ$
1249 (K) for calculation. For the given temperature, pressure and path length, Eq.(20) gives $n \approx$
1250 $2.8921135\cdot 10^{22}\text{ (molec/cm}^2\text{)}$.

1251 **Fig.4 (a)** shows the simulated transmittance vs. wavenumber $\nu = [13006, 13166] \text{ (cm}^{-1}\text{)}$ and the
 1252 optical thickness vs. corresponding wavelength. **Fig.4 (b)** reproduces the same but within a sub-
 1253 band, $\nu = [13159.6, 13165.6] \text{ (cm}^{-1}\text{)}$. These spectral intervals are borrowed from Fig.1 in (P-C).
 1254 Images like that published in (P-C) and here help debug the program qualitatively by visually
 1255 inspecting the picture for presence of lines and quantitatively by checking their order of
 1256 magnitude.

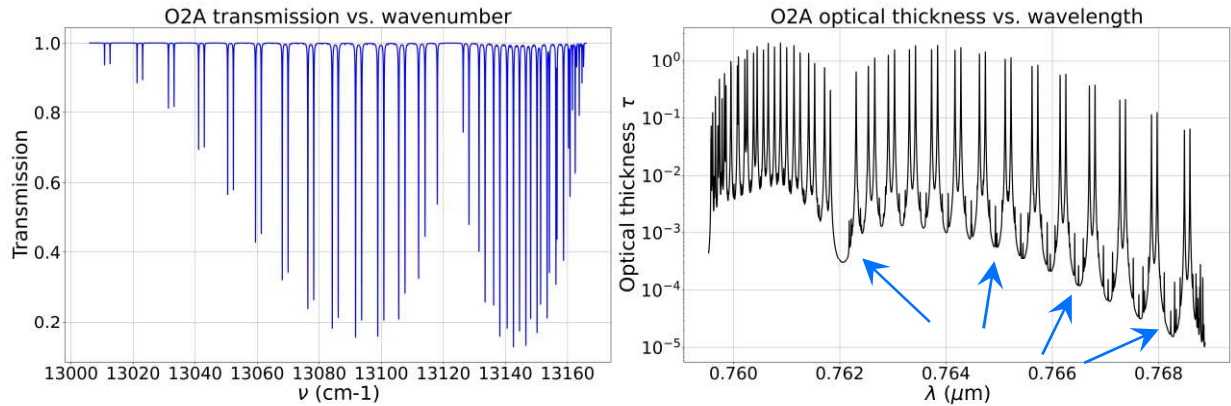


Fig.4 (a): Direct one way transmission (left) and corresponding optical thickness (right, log scale for y-axis) for the O₂A band. The left image reproduces Fig.1(A) from *Predoi-Cross et al.*, (2008: p. 91). Visual comparison of the two serves as qualitative validation of code `gcell`. The arrows in the right image indicate some weak absorption lines caused by isotopes with low abundance.

1257

1258 Our experience shows that once possible problems at these two steps are resolved, the code
 1259 should work without major problems.

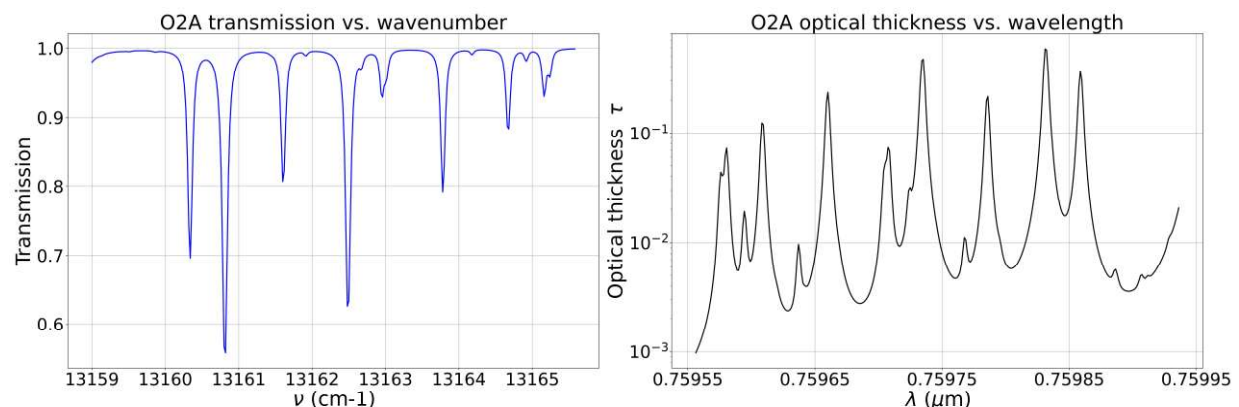


Fig.4 (b): Same as Fig.4(a), except for narrow band. The left image reproduces Fig.1(B) from *Predoi-Cross et al.*, (2008).

1260

1261 An ASCII file `./benchmarks/Sec5p4p1__test_gcell_o2a.txt` contains results
1262 of our numerical simulation. The file contains 8000 rows, excluding three header ones, and two
1263 columns. The left column is the wavenumber $v (cm^{-1})$ from 13006.00 to 13165.98 step 0.02. The
1264 right one contains τ (right images in **Fig.4 (a-b)**). Plotting $\exp(-\tau)$, Eq.(24), shows left images. .

1265 5.4.2 Methane band at 2.3 (μm)

1266 Our second benchmark scenario is for `imolec = 6`: methane, CH_4 , which is a greenhouse gas.
1267 The gas is at the same room temperature, $T = 296^{\circ} (K)$, and slightly different pressure $p = 1000.0$
1268 ($mbar$) ≈ 0.986923 (atm) compared to the previous scenario. Unlike for the published oxygen
1269 scenario, we compare our numerical simulation vs. the one kindly provided by the GATS⁴⁵ Inc.
1270 team. The GATS data contains the CH_4 spectral transmittance of an $l = 8$ (cm) gas cell, computed
1271 using the SpectralCalc⁴⁶ tool (*Gordley et al., 1994*), convolved with a spectral filter for their
1272 Digital-Array Gas-correlation Radiometer - DAGR⁴⁷. The particles columnar number density,
1273 Eq.(20), for this case is $n \approx 1.9575594 \cdot 10^{20}$ ($molec/cm^2$).

1274 The GATS data is based on HITRAN 2016 and defined within the inclusive interval $v =$
1275 $4081.901 \dots 4505.699$ (cm^{-1}), step $dv = 0.002$ (cm^{-1}). Considering their data as a benchmark, we
1276 calculated spectra of optical thickness (**Fig.5 (a)**), and corresponding direct one way
1277 transmittance (**Fig.5 (b)**), Eq.(24) with $\mu = 1$, and convolved the two. **Fig.5 (c)** shows the
1278 instrument filter (dash line), benchmark convolution (black curve), and absolute difference
1279 between our and the benchmark data (red line – almost at 0). The absolute difference, which is
1280 ~ 1000 times smaller compared to the convolution, is pictured separately in **Fig.5 (d)**.

⁴⁵ <https://www.gats-inc.com/>

⁴⁶ <https://www.spectralcalc.com/> (note recent updates: “What’s New at SpectralCalc!”)

⁴⁷ https://www.gats-inc.com/future_missions.html#DAGR

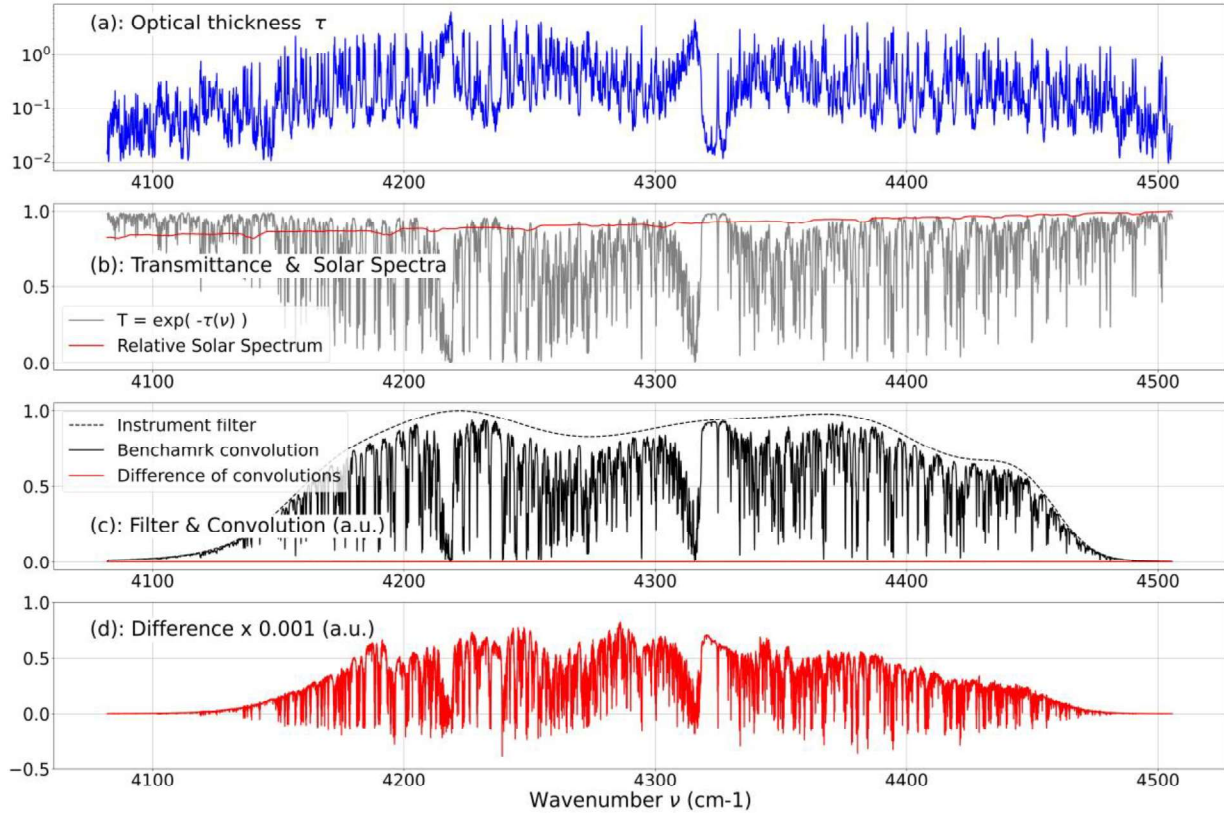


Fig.5: Graphical results for a methane gas cell test (see y-axis caption for letters (a-d)). (a) Optical thickness τ calculated using `gcell`; (b) Direct one-way transmittance, $\exp(-\tau)$, and solar irradiance relative to maximum within the band; (c) Instrument filter function (dash line), convolved with transmittance (solid line – benchmark result), and absolute difference between the benchmark result and that computed with `gcell` (red line – almost at 0). (d) The same difference pictured separately – note the scaling factor 0.001 on y-axis, i.e. the difference does not exceed 0.0008 (a.u.)

1281

1282 Next, we calculated an absolute signal transmitted through the methane gas cell. For that, we
 1283 used the *Chance-Kurucz* extraterrestrial solar irradiance spectrum defined from 50 (cm^{-1}) to
 1284 50000 (cm^{-1}) with 1 (cm^{-1}) resolution (Kurucz, 1992 & 1997; *Chance & Kurucz*, 2010). **Fig.5(b)**
 1285 (second from top - red line) shows part of the solar spectrum relative to maximum value within
 1286 the band and interpolated from 1 (cm^{-1}) grid to 0.002 (cm^{-1}) using Python's cubic spline. We then
 1287 calculated the transmitted signal

$$1288 \quad u = \int_{\Delta\nu} S_0(\nu) \exp(-\tau(\nu)) f(\nu) d\nu \quad (27)$$

1289 to obtain 187.03 (W/m^2) using benchmark convolution and 187.14 (W/m^2) using `gcell`.
 1290 Switching between trapezoidal and Simpson integration in Eq.(27) did not change the numbers.
 1291 For the spectrally integrated transmittances, Eq.(25), the values are 0.7007 (benchmark) and

1292 0.7011 (`gcell`) or +0.0004 vs. the benchmark in absolute units (*a. u.*) of transmittance.
1293 Corresponding effective (spectrally integrated) absorption optical thicknesses, Eq.(26), are
1294 0.3557 and 0.3552 (or -0.2% vs. the benchmark), respectively.
1295 We compiled an ASCII file, `./benchmarks/Sec5p4p2__test_gcell_ch4.txt`, for
1296 accurate reproducibility of this numerical exercise. The file contains 211900 rows, excluding
1297 header. Columns, left to right, contain wavenumber (floating point format with 3 digits after
1298 decimal point), optical thickness calculated using our code `gcell` (scientific format, 7 digits
1299 total), direct transmittance for the same (floating point format, 6 digits), filter function,
1300 convolution of the `gcell` transmittance with the filter, benchmark convolution (all the three are
1301 in scientific format with 6 digits total and provided by the GATS team), and difference of the last
1302 two (scientific format, 2 digits). The header shows the total number of points and names of the
1303 columns.

1304 6. Absorption in Earth's atmosphere

1305 In the previous section we explained in detail how to calculate absorption by gas in a cell, where
1306 temperature, pressure, and the gas concentration are constant. In atmospheres, however, all these
1307 parameters vary with height. Their profiles come from another established package,
1308 MODTRAN, the elements of which we consider in the next section. After that, we integrate the
1309 MODTRAN profiles over height to get column amount of each considered molecule in
1310 atmosphere, discuss units expressing that amount, and calculate τ profile – one topic per section.

1311 6.1 Elements of MODTRAN

1312 MODTRAN is a comprehensive RT code, in Fortran, for calculation of atmospheric radiances
1313 and transmittance across the solar and thermal spectral region: from 100 to 50,000 (cm^{-1}) or 0.2
1314 to 100 (μm). Multiple scattering is simulated using scalar RT code DISORT (Stamnes et al.,
1315 1988; Laszlo et al., 2016). MODTRAN v.6.0 (Berk et al., 2014, 2017, 2019) is the current
1316 release. It is not publicly available except for the online tool MODTRAN Demo⁴⁸. However, the
1317 atmospheric profiles for aspect are published in a manual for MODTRAN v.2 / LOWTRAN
1318 v.7 (Kneizys et al., 1996), the latter being a precursor for MODTRAN.

⁴⁸ http://modtran.spectral.com/modtran_home

1319 The MODTRAN/LOWTRAN package defines 6 atmospheres. They are “Tropical (15N Annual
 1320 Average)”, “Mid-Latitude Summer (45N July)”, “Mid-Latitude Winter (45N Jan)”, “Sub-Arctic
 1321 Summer (60N July)”, “Sub-Arctic Winter (60N Jan)”, and “U. S. Standard (1976)”. Aspect
 1322 calls them by an index $i_{atm} = 1 \dots 6$. The grid of heights, same for all profiles, consists of
 1323 three parts (see **Fig.6 (a)**): lower - below 25 (km), middle – between 25 and 50 (km), and upper
 1324 50-120 (km). The corresponding steps are 1, 2.5, and 5 (km). For reference, about 50%, 70% and
 1325 95% of Rayleigh atmosphere are located below 5, 10, and 25 (km), respectively.

1326

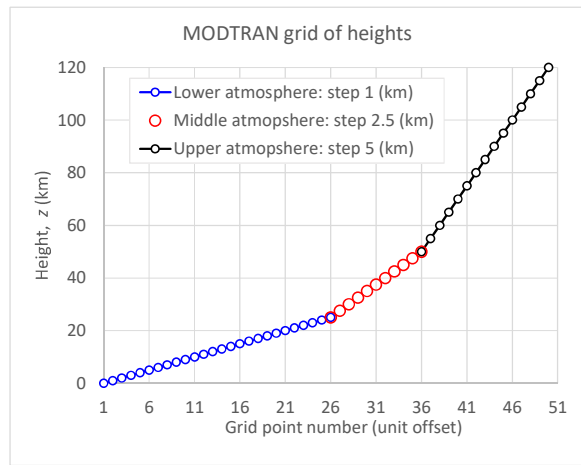
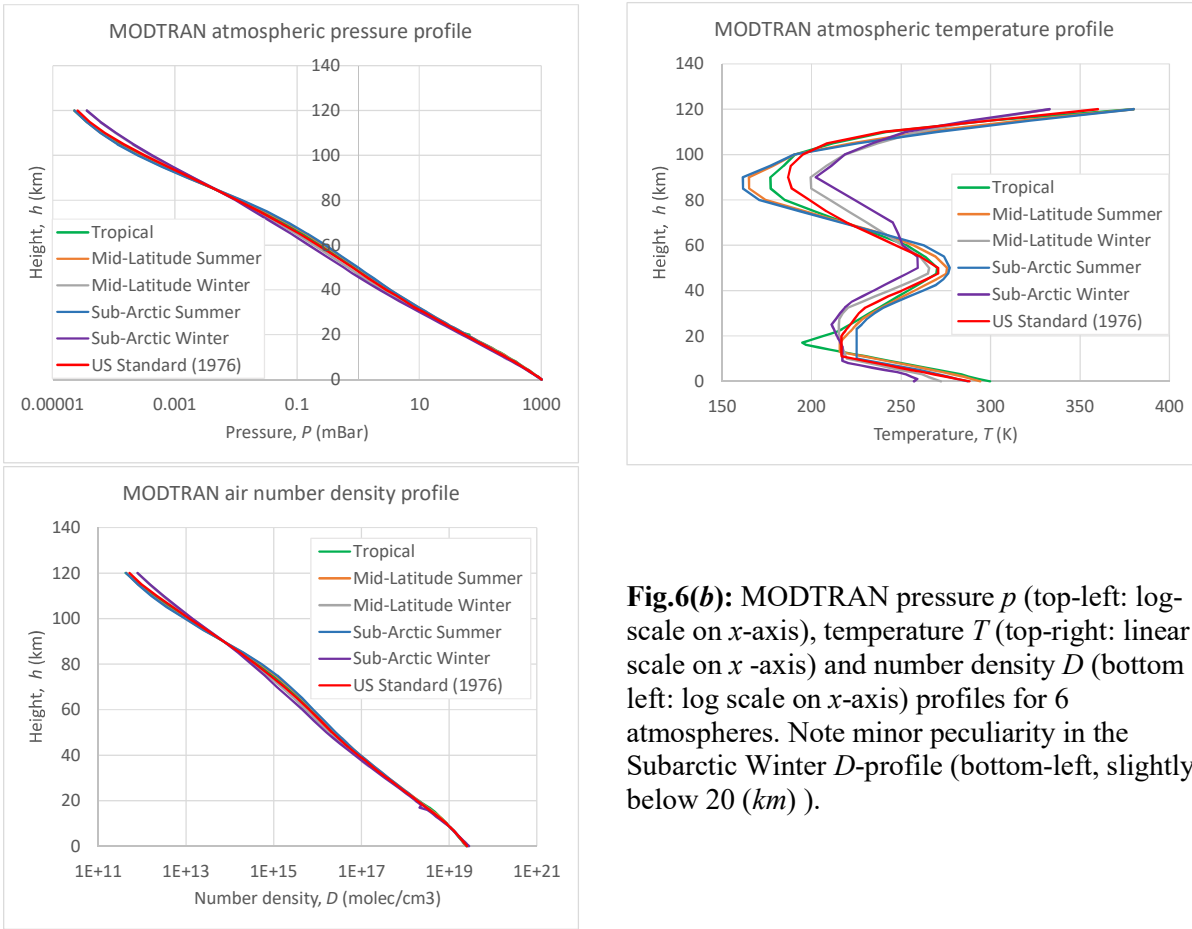


Fig.6(a): MODTRAN defines 3 intervals in the grid of heights: 1) lower atmosphere, 0-25 (km), step 1 (km) - 26 points; 2) middle atmosphere, 25-50 (km), 2.5 (km) step – 11 points; 3) upper atmosphere, 50-120 (km), step 5 (km) – 15 points. Boundary points #26 and #36 belong to both adjacent intervals.

1327

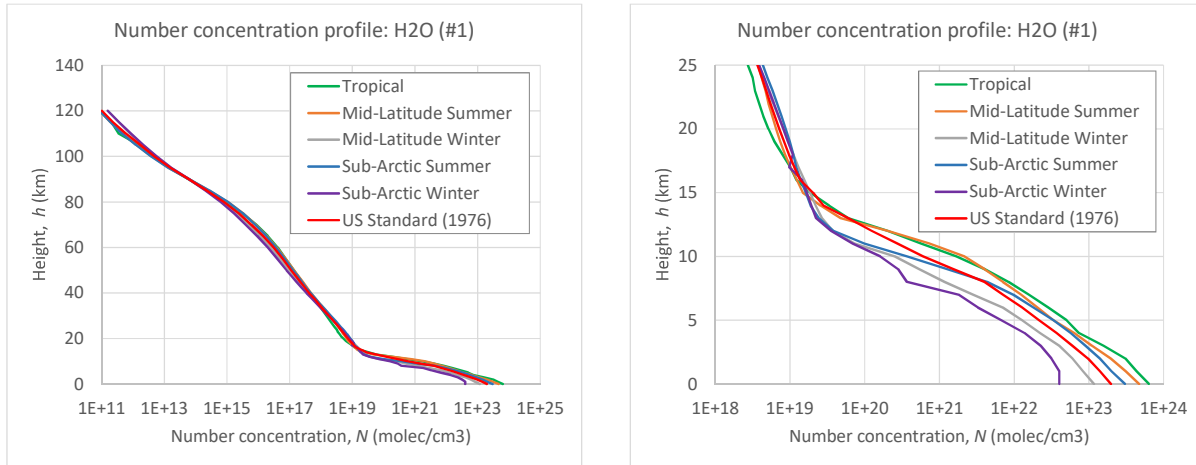
1328 For each of 6 atmospheres, MODTRAN/LOWTRAN provides LUTs with pressure p (mbar),
 1329 temperature T (K), and molecular number density per unit volume (air density) D (cm^{-3}) –
 1330 **Fig.6(b)**. The temperature profile shows the stronger variations, while the other two change little
 1331 between 6 atmospheres. Lastly, for each of the 8 main atmospheric gases, the mixing ratio in
 1332 parts-per-million in a volume (ppmv) is defined. **Fig.6(c-f)** illustrates the absolute number
 1333 concentration in cm^{-3} for each molecule calculated as the product of the atmospheric air density
 1334 and the volume mixing ratio (scaled by 10^{-6} to account for “per million”). In each figure, left
 1335 charts show the full range of the MODTRAN heights, 0-120 (km); right columns show lower
 1336 atmosphere 0-25 (km) with 1 (km) step. For another reference, we note that NASA’s ER-2
 1337 airplane carry airborne prototypes of satellite instruments at ~ 20 (km) altitude (Diner et al., 2013:
 1338 Sec.2.6; Puthukkudy et al., 2020: Sec.3.1).



1339

1340 Aspect defines all the mentioned parameters in `hprofiles.h`. This simplifies updating the
1341 existing parameters or adding a new one, if needed.

1342



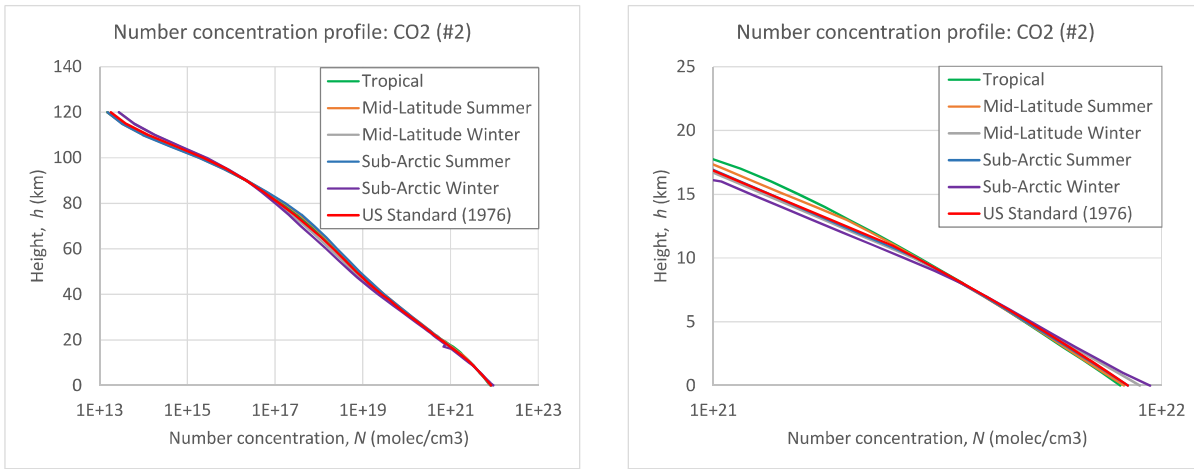


Fig.6(c): Number concentration profiles for H_2O (#1) and CO_2 (#2). The profiles are calculated based on the MODTRAN models for 6 atmospheric profiles. Left column: full range of the MODTRAN heights. Right column: lower atmosphere 0-25 (km) with 1 (km) step.

1343

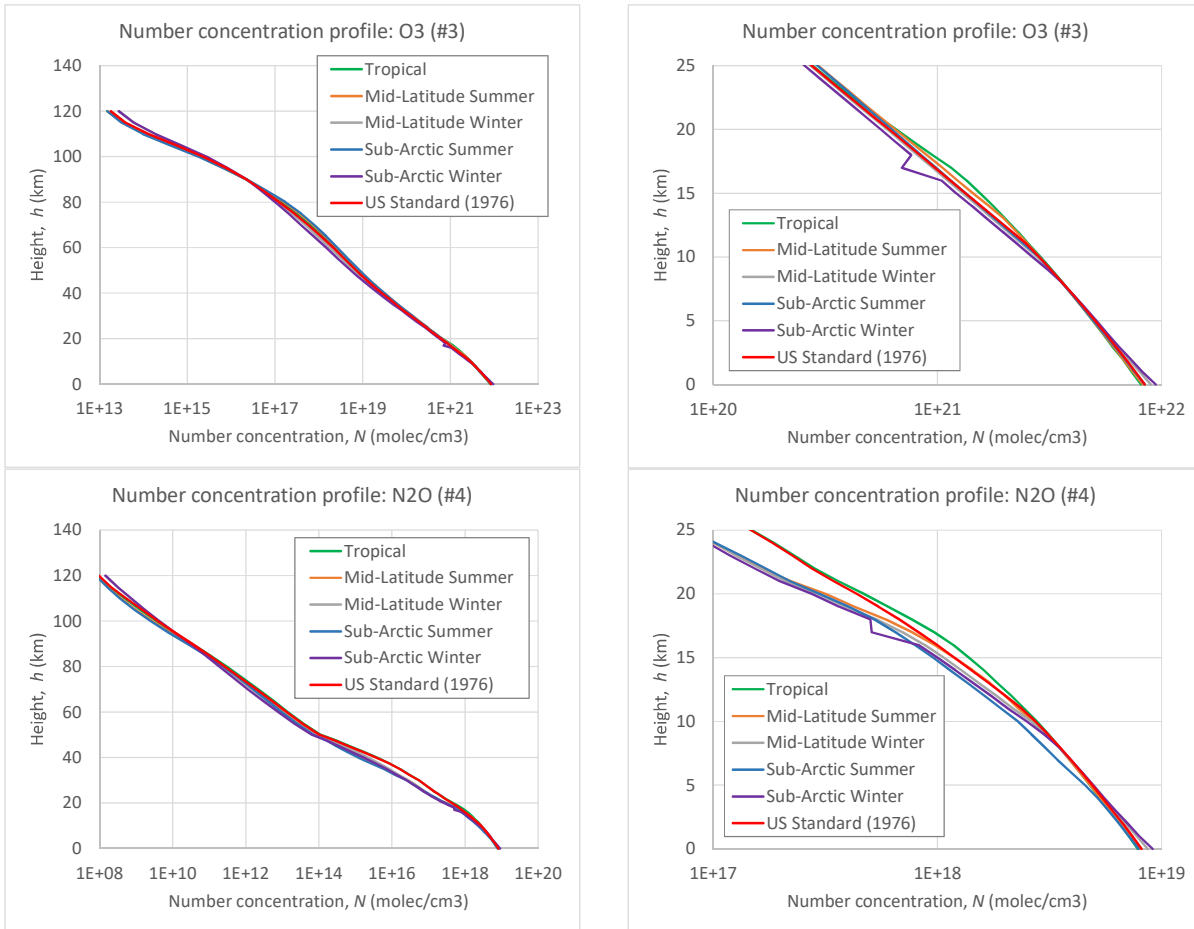


Fig.6(d): Same as **Fig.6(c)**, except for O_3 (#3) and N_2O (#4).

1344

1345

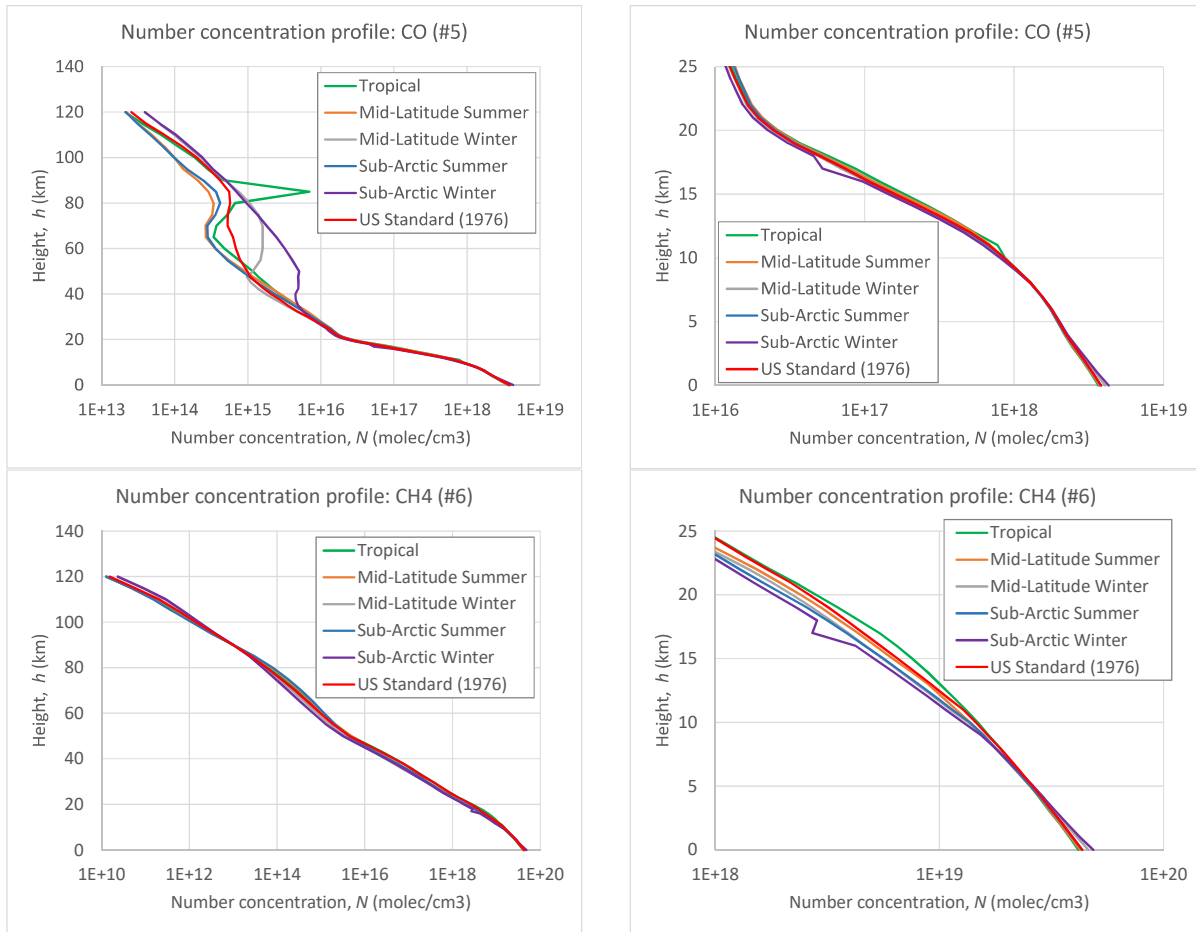
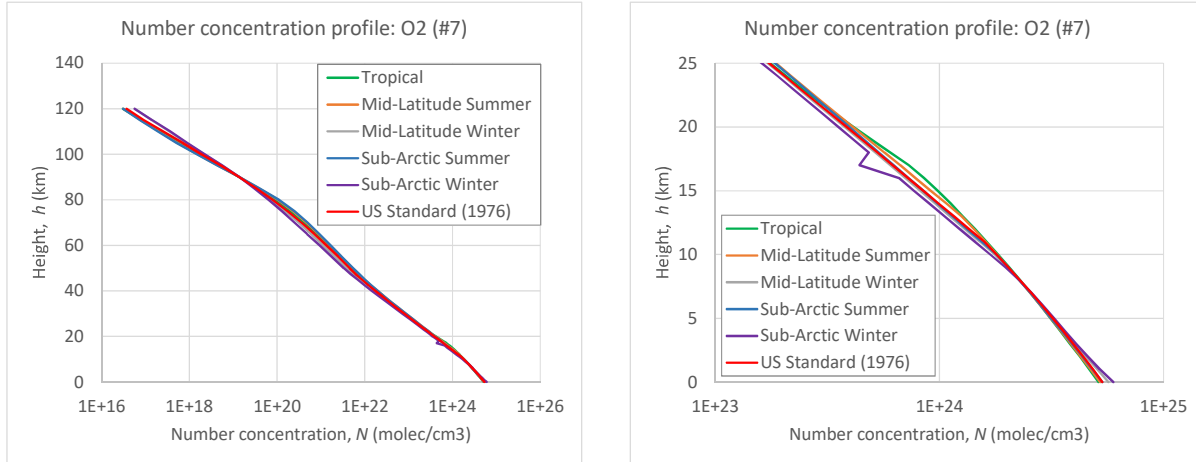


Fig.6(e): Same as **Fig.6(c)**, except for CO (#5) and CH₄ (#6).

1346

1347



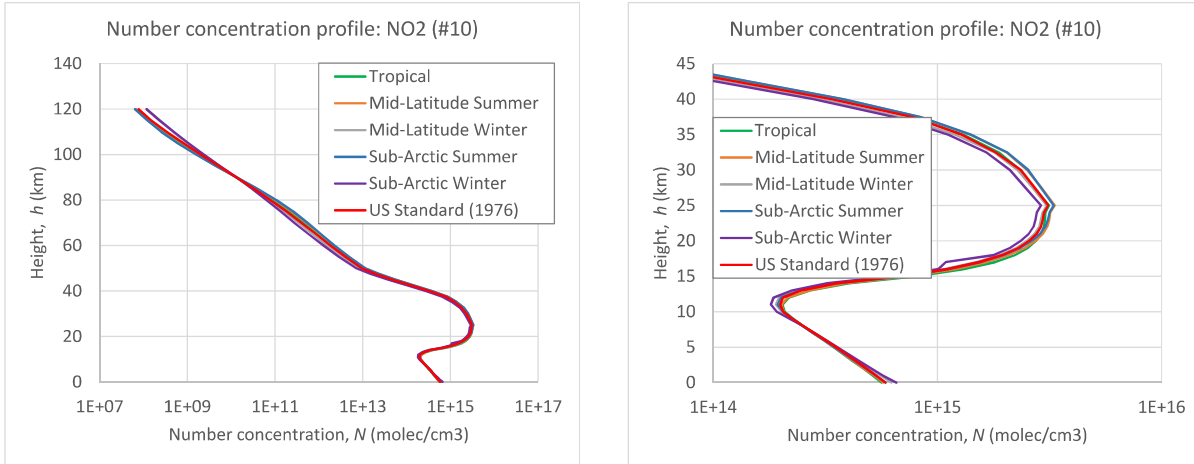


Fig.6(f): Same as Fig.6(c), except for O₂ (#7) and NO₂ (#10). Note 0 – 45 (km) in the right chart.

1348

1349 [6.2 Column amount of gas in atmosphere](#)

1350 Integration of the number concentration from BOA, $z = 0$ (km), to TOA, $z = 120$ (km), gives the
1351 columnar number density N_C (molec/cm²)

$$1352 N_C = \int_{0 \text{ km}}^{120 \text{ km}} D(z) dz. \quad (28)$$

1353 Eq.(28) uses, as an example, the MODTRANS's density of air $D(z)$ (molec/cm³) and integrates
1354 over z (km). To account for different units of length, a conversion scaling factor 10⁵ (cm/km)
1355 pops up in subsequent calculations. Numerical integration as in Eq.(28) involves a certain error,
1356 which we quantify below.

1357 Absolute value of the optical thickness is directly proportional to the result of the integration.
1358 Hence, relative error of the numerical integration is transported to the value of τ as 1:1. We
1359 quantify the error by comparing 3 methods of numerical integration: trapezoidal, Simpson, on
1360 the native MODTRAN grid of heights, and Simpson on a fine grid using cubic spline
1361 interpolation from the native grid to a finer one. We did the test in Python, hence it is not part of
1362 our C-package, and picked one method to be coded in C-language.

1363 **Table 5** shows the result of the integration for all 6 atmospheric profiles and different methods of
1364 integration. In each number, one space separates digits that are not in agreement with others in
1365 the column. For the trapezoidal and Simpson integration we use Python's `numpy.trapz` and
1366 `scipy.integrate.simpson`, respectively. To get the numbers in the “spline” row, we first

1367 interpolated the MODTRAN profiles from the default grid (**Fig.6(a)**) to an equidistant fine grid
 1368 with step $dz = 0.5$ (km) using Python's cubic spline. Then we integrated the interpolated profiles
 1369 on the fine grid using Simpson's technique. The last line, `aspect`, shows respective results of
 1370 our implementation of the Simpson quadrature in C, which we picked based on the accuracy
 1371 (better than trapezoidal) vs. coding burden (no dependence on splines). Numerical results from
 1372 **Table 5** are suitable for intermediate validation of one's code (unit testing).

1373

1374 **Table 5:** Total atmosphere columnar number density $N_C \cdot 10^{25}$ (molec/cm²), Eq.(28), for 6 model
 1375 atmospheres, and different techniques of integration. ML and SA correspond to Midlatitude and
 1376 Subarctic, respectively. The common scaling factor 10^{25} is dropped. Space separates digits that are not in
 1377 agreement with others for the same atmosphere (same column).

Technique	Tropical	ML Summer	ML Winter	SA Summer	SA Winter	US 1976
Trapezoid	2.16 71	2.1 620	2.1 685	2.1 503	2.1 503	2.15 71
Simpson	2.164 6	2.159 3	2.165 5	2.147 7	2.146 6	2.154 5
Spline	2.164 5	2.159 3	2.165 3	2.147 6	2.146 1	2.154 4
aspect	2.164 2	2.159 5	2.165 1	2.147 4	2.14 40	2.154 6

1378

1379 Except for the Subarctic Winter model (see bold number in **Table 5**), `aspect` agrees with
 1380 Python's spline and Simpson methods within 4 digits. In `aspect`, we use our self-coded
 1381 Simpson's rule for the numerical integration over height. Simpson's rule approximates the
 1382 function with a second-degree polynomial; hence the number of points must be odd. MODTRAN
 1383 uses 26 points in the lower atmosphere (**Fig.6(a)**). So, we use Simpson's rule for the first 25
 1384 points - up to 24 (km)

1385 `hint0_24km = simpson(&conc_all, 25, 1.0);`

1386 Then we draw and integrate a separate parabola for the 24-25 (km) region using 23 (km) as a
 1387 third point (could be replaced just by trapezoidal integration)

1388 `hint24_25km = intparab(24.0, 25.0, &zkm_mod[23], &zkm_mod[24],`
 1389 `&zkm_mod[25], &conc_all[23], &conc_all[24], &conc_all[25]);`

1390 Afterwards, we use Simpson's rule again for the middle (11 points, 2.5 km step)

1391 `hint25_50km = simpson(&conc_all[25], 11, 2.5)`

1392 and upper (15 points, 5.0 km step)

1393 `hint50_120km = simpson(&conc_all[35], 15, 5.0)`

1394 parts of the atmosphere (note odd number of points for both). Adding all these gives one the
 1395 column number concentration `nmolec_all` (*molec/cm²*) in the whole atmosphere

1396 `nmolec_all = (hint0_24km + hint24_25km + hint25_50km +`
 1397 `hint50_120km) * km_to_cm;`

1398 where the scaling factor `km_to_cm = 1.0e5` relates kilometers in the grid of height and
 1399 centimeters in the volume number density, and `_all` refers to all molecules in the air mixture.

1400 Identically, by integrating a particular gas number concentration over height from BOA to TOA,
 1401 one gets the total columnar number concentration for that gas only. E.g., for methane (#6: CH₄)
 1402 we first calculate the gas mixing ratio from the *ppmv*-value

1403 `case 6:`
 1404 `for (iz = 0; iz < nz_mod; iz++)`
 1405 `gas_ratio[iz] = CH4_ppmv[iatm-1][iz]/1.0e6;`
 1406 `break`

1407 and the height distribution of the volume number concentration `conc_cm3[]`

1408 `for (iz = 0; iz < nz_mod; iz++)`
 1409 `...`
 1410 `conc_cm3[iz] = Dcm3_mod[iatm-1][iz]*gas_ratio[iz];`
 1411 `...`

1412 The abovementioned numerical integration of the methane number concentration over height
 1413 gives `nmolec = 3.5523e+19` (*molec/cm²*) or `ppm_ch4 = 1.6487`, in terms of *ppmv*

1414
$$ppmv_{molec} = 10^6 n_{molec} / n_{all} \quad (29)$$

1415 `column_amount_mod = nmolec*1.0e6/nmolec_all;`

1416 for the US 1976 standard atmosphere. This is the “standard” MODTRAN value, which is used in
 1417 calculations by default if the user provides negative gas concentration as input parameter (see
 1418 Sec.3.2.2). For validation purposes, **Table 6** indicates the “standard” columnar amount of the
 1419 considered gases, for all atmospheres, in absolute units and in *ppmv* – i.e., relative to the values
 1420 from the bottom row aspect in **Table 5**.

1421

1422 **Table 6:** Absolute (top: in number of molecules) and relative (bottom: in *ppmv* w.r.t. **Table 5:** row =
1423 *apsect*) columnar amount of atmospheric gases, calculated by *apsect*.

#	Molec	Tropical	Mid Lat Sum	Mid Lat Win	Sub Arc Sum	Sub Arc Win	US 1976
1	H ₂ O	1.3769E+23	9.8002E+22	2.8614E+22	6.9511E+22	1.4215E+22	4.7460E+22
		6362.24	4538.21	1321.60	3237.07	663.00	2202.72
2	CO ₂	7.1420E+21	7.1263E+21	7.1449E+21	7.0863E+21	7.0752E+21	7.1102E+21
		330.00	330.00	330.00	330.00	330.00	330.00
3	O ₃	7.6343E+18	8.9471E+18	1.0191E+19	9.3798E+18	9.9720E+18	9.2607E+18
		0.352747	0.414317	0.470691	0.436808	0.465114	0.429811
4	N ₂ O	6.6300E+18	6.3862E+18	6.4632E+18	5.8955E+18	6.4306E+18	6.6159E+18
		0.306346	0.295727	0.298517	0.274547	0.299937	0.307058
5	CO	2.3730E+18	2.3608E+18	2.4218E+18	2.3688E+18	2.4433E+18	2.3879E+18
		0.109647	0.109322	0.111855	0.110314	0.113961	0.110828
6	CH ₄	3.5626E+19	3.4132E+19	3.4454E+19	3.3785E+19	3.4109E+19	3.5523E+19
		1.646144	1.580553	1.591323	1.573330	1.590893	1.648702
7	O ₂	4.5232E+24	4.5133E+24	4.5251E+24	4.4880E+24	4.4810E+24	4.5031E+24
		209000	209000	209000	209000	209000	209000
10	NO ₂	5.7520E+15	5.9628E+15	5.4231E+15	5.8875E+15	5.0470E+15	5.5625E+15
		0.000266	0.000276	0.000250	0.000274	0.000235	0.000258

1424

1425 To account for a different column amount of the gas, `column_amount_usr` (Sec.3.2.2) the
1426 user scales the vertical distribution of the number concentration and partial pressure, while the
1427 total pressure is not altered

```

1428     scalef = column_amount_usr/column_amount_mod;
1429     for (iz = 0; iz < nz_mod; iz++) {
1430         conc_cm3[iz] *= scalef;
1431         Pgas[iz] *= scalef;
1432     }

```

1433 After rescaling, we recommend integration over the column again, with the user-defined gas
1434 concentration, and checking the new *ppmv* value. It must match the input. *Aspect* does it by
1435 default and prints the user input on the screen.

1436 We note that the default MODTRAN values may be significantly outdated. For example, in
 1437 recent years the average amount of CH₄ in the atmosphere has grown from the MODTRAN's
 1438 ~1.6 (ppmv) to approximately 1.75 (ppmv) in 2020 (Bernath et al., 2020: Fig.21) and 1.92
 1439 (ppmv) in 2024 as indicated on the NOAA's Global Monitoring Laboratory website⁴⁹. For CO₂
 1440 and N₂O these numbers have also grown, respectively, from 330 and 0.297 (ppmv) in
 1441 MODTRAN to 422 and 0.337 (ppmv) at the present time, according to the NOAA website.

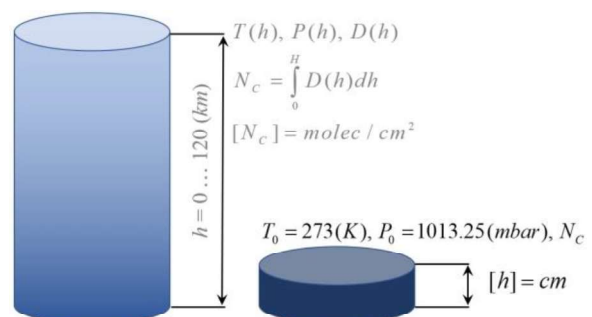
1442 The physically correct scaling of the partial pressure has non-linear effect on the resulting optical
 1443 thickness. However, **Fig.3** (right) shows that this effect may be overall insignificant. In this case,
 1444 the resulting optical thickness would depend on the concentration linearly, which simplifies
 1445 retrieval. For instance, one creates an optical thickness LUT for a unit amount of gas and scales
 1446 it according to the change of concentration.

1447 6.3 The mysterious *atm-cm/km*

1448 In addition to ppmv, the atmosphere-centimeter per kilometer, *atm-cm/km*, is another way to
 1449 define the relative (unitless) amount of gas in the atmosphere. It is widely used in practice by
 1450 some atmospheric scientists but looks confusing to others. Finding the relation between the two
 1451 units in literature is possible (see e.g., Berk et al., 1999: Sec. 3.4.1) but not always easy, which
 1452 induced us to compile this section.

1453 The *atm-cm* in the numerator indicates height of the gas layer, in *cm*, if one would bring all
 1454 molecules of the gas from the whole atmospheric column (which is measured in *km* -
 1455 denominator) to standard conditions, $T_0 = 273.15^\circ (K)$, $p_0 = 1 (atm)$, known as "standard
 1456 (atmospheric) temperature and pressure" – SATP or STP, **Fig.7(a)**.

Fig.7(a): Definition of the units of *atm-cm/km*. The tall column on the left represents a realistic atmosphere with some temperature, pressure, and density profiles. The right column is at normal condition but holds the same number of the gas molecules N as the right one. Both columns stand on the unit area surface element S .



⁴⁹ https://gml.noaa.gov/ccgg/trends/gl_data.html

1457

1458 In order to convert the MODTRAN density profile in $molec/cm^3$ into $atm\cdot cm/km$, one uses

1459
$$p = nk_B T = \frac{N}{Sh} k_B T, \quad (30)$$

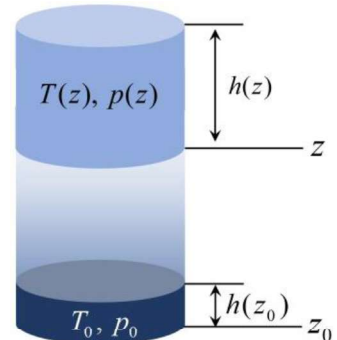
1460 where n ($molec/cm^3$) is the volume number concentration. From this equation one gets the ratio
1461 of two heights of gas in different thermodynamic conditions over the same (unit) area S of the
1462 atmospheric column (**Fig.7(b)**)

1463
$$\frac{h(z_0)}{h(z)} = \frac{T_0}{p_0} \frac{p(z)}{T(z)} = \frac{T_0}{p_0} nk_B \left(\frac{atm\cdot cm}{cm} \right) = \frac{T_0}{p_0} nk_B 10^5 \left(\frac{atm\cdot cm}{km} \right). \quad (31)$$

1464 In Eq.(31), the scaling factor 10^5 converts km to cm , and k_B and n are in SI units.

Fig.7(b): Graphical explanation for Eq.(31). Both heights h , measured at levels z and z_0 , are small so that temperature and pressure are constant with the shown volumes; the number of molecules in both volumes is the same.

Any volume element $h(z)$, floating at level z in the atmosphere, can be reduced to the one at normal conditions, $h(z_0)$.



1465

1466 In terms of code, `aspect` converts MODTRAN's number density profiles into $atm\cdot cm/km$ as
1467 follows

```
1468     c_stp = 1.0e5 * (k_boltzman * 1.0e-7) * To_stp / Po_stp * 1.0e6;  
1469     atmcm_km = new double [nz_mod];  
1470     for (iz = 0; iz < nz_mod; iz++) atmcm_km[iz] = c_stp*conc_cm3[iz];
```

1471 Note, the factors $1.0e-7$ and $1.0e6$ bring the Boltzmann constant and the number density,
1472 respectively, to SI units; `_stp` stands for “standard temperature and pressure”.

1473 In fact, `aspect` does not use the `atmcm_km` array in calculations. However, it can be used to
1474 test numerical integration over height and to convert units from/to other data sources. For

1475 example, the MODTRAN website⁵⁰ reports numerical results (5 significant digits) for the total
 1476 amount of species in *atm-cm* (integrated over height, hence no “per kilometer”). **Table 7**
 1477 replicates their results in our paper for convenience (only molecules #1-7 and #10), while **Table**
 1478 **8** compares numbers from **Table 7**, assumed baseline, vs. those for `aspect` and SHARM-IPC.
 1479 Negative sign in **Table 8** means our numerical result exceeds the one from **Table 7**.

1480

1481 **Table 7:** MODTRAN’s total vertical column amounts (*atm-cm*) listed in HITRAN order. CO₂ is indicated
 1482 for 380 (*ppmv*) as opposed to the default MODTRAN value of 330 (*ppmv*) – see **Table 6** and 2* below.

#	Molec	Tropical	Mid Lat Sum	Mid Lat Win	Sub Arc Sum	Sub Arc Win	US 1976
1	H ₂ O	5.1194E+03	3.6359E+03	1.0597E+03	2.5894E+03	5.1773E+02	1.7623E+03
2*	CO ₂	3.0587E+02	3.0513E+02	3.0599E+02	3.0347E+02	3.0421E+02	3.0448E+02
3	O ₃	2.7727E-01	3.3176E-01	3.7681E-01	3.4492E-01	3.7550E-01	3.4356E-01
4	N ₂ O	2.4649E-01	2.3743E-01	2.4037E-01	2.1920E-01	2.3993E-01	2.4593E-01
5	CO	3.0587E+02	3.0513E+02	3.0599E+02	3.0347E+02	3.0421E+02	3.0448E+02
6	CH ₄	1.3243E+00	1.2684E+00	1.2806E+00	1.2556E+00	1.2719E+00	1.3203E+00
7	O ₂	1.6823E+05	1.6782E+05	1.6829E+05	1.6691E+05	1.6732E+05	1.6746E+05
10	NO ₂	2.1091E-04	2.1814E-04	1.9842E-04	2.1543E-04	1.8654E-04	2.0418E-04

1483

1484 Regarding **Table 8**, we note that profiles and numerical integration technique used in SHARM-
 1485 IPC-LBL and `aspect` are not the same. First, in SHARM-IPC-LBL, the vertical distribution of
 1486 molecules is defined in (*atm-cm/km*), instead of the number density concentration (*molec/cm³*).
 1487 Next, the number of points over height is different. The middle atmospheres 25-50 (*km*) uses 5
 1488 (*km*) step (6 points), and the upper atmosphere uses 25 (*km*) step. The TOA is assumed at 100
 1489 (*km*), thus the upper part of atmosphere contains only 3 points. The total number of points in the
 1490 height grid is 33 (compare with **Fig.6(a)**).

⁵⁰ http://modtran.spectral.com/modtran_faq, Table 1: Total vertical column amounts (*atm-cm*) for the 12 ambient band model species

1491 SHARM-IPC-LBL uses the following algorithm for integration of its profiles. For the lower, 0:
 1492 1:25 (km) the trapezoidal quadrature is used. For the middle atmosphere, 25:5:45 (km)
 1493 atmosphere, the profile is first interpolated from 5 equidistant points, 5 (km) step, to 11
 1494 equidistant points, 2 (km) step, using the quadratic spline interpolation. Then, Simpson's rule is
 1495 used on these 11 interpolated points. The last four points, 45, 50, 75, and TOA at 100 (km), are
 1496 interpolated with an exp-function

1497
$$f(z) = f(45) \exp(-\alpha(z-45)). \quad (32)$$

1498 In Eq.(32), the decay factor α (km^{-1}) is derived from the log-linear least squares fit at the last
 1499 three points. We refer our reader back to Sec.6.2 for the vertical integration we use in `aspect`.

1500

1501 **Table 8:** Relative difference, in %, for MODTRAN (assumed as baseline, in **Table 7**) vs. `aspect` (left)
 1502 and SHARM-IPC (right: gray). Negative values mean our result exceeds the one for MODTRAN.

#	Molec	Tropical		Mid Lat Sum		Mid Lat Win		Sub Arc Sum		Sub Arc Win		US 1976	
1	H ₂ O	0.1	2.0	0.3	2.0	0.5	1.5	-0.1	1.5	2.2	1.2	0.2	1.4
2	CO ₂	0.1	0.0	0.1	0.0	0.1	0.1	0.1	0.0	-0.3	0.1	0.1	0.0
3	O ₃	2.5	2.6	0.4	1.6	0.7	0.5	1.2	0.4	-1.2	0.2	0.3	0.7
4	N ₂ O	0.1	0.0	0.1	0.0	0.1	0.1	0.1	0.1	-0.2	0.1	0.1	0.0
5	CO	0.8	0.1	0.1	0.2	0.1	0.3	0.1	0.1	0.0	0.3	0.2	0.2
6	CH ₄	0.1	0.0	0.2	0.0	0.1	0.0	0.1	0.0	-0.2	0.0	0.1	0.1
7	O ₂	0.1	0.0	0.1	0.0	0.1	0.1	0.1	0.0	-0.3	0.1	0.1	0.1
10	NO ₂	1.5	2.5	1.7	2.6	1.7	2.6	1.7	2.8	0.7	2.8	1.4	2.7

1503

1504 Because of the difference in profiles and numerical integration technique, the overall maximum
 1505 (and average) relative deviation of `aspect` and SHARM-IPC-LBL w.r.t. the MODTRAN
 1506 values are 2.5% (0.5%) and 2.8% (0.8%), respectively. **Table 8** shows that the Sharm-IPC
 1507 deviation is always higher, while that for `aspect` changes sign w.r.t to the MODTRAN values.
 1508 We ignored the change of sign in the overall errors mentioned. Also, based on our literature
 1509 search, we were unable to clarify MODTRAN's technique for vertical integration.

1510 6.4 Profile of optical thickness

1511 Aspect uses three steps to calculate the absorption optical thickness profile. For one, profile of
1512 the molecular absorption cross-section, k ($cm^2/molec$), is calculated in `kabs (...)` for each
1513 wavenumber v from the user's grid $[v_{min}, v_{max}]$ with step Δv . This is like the one for the gas cell
1514 (Sec.5): one picks all HITRAN line contributions to the user-defined band and accumulates
1515 them. The only two differences from simulation of the gas cell are: (1) one deals with a mixture
1516 of gases – hence Eq.(8) for the Lorentzian HWHM parameter uses both the total atmospheric and
1517 partial gas pressures, and two HITRAN parameters: γ_{self} and γ_{air} ; and (2): the atmosphere is a
1518 stack of “gas cells”, one on top of the other. Therefore, `kabs (...)` accepts as input the user's
1519 range of wavenumbers, parameters of the HITRAN lines (limited to those contributing to the
1520 user interval – see Sec.5.1), and profiles of temperature and pressure. The output of `kabs (...)`
1521 is the spectral and height dependence of the absorption cross-section, $k(v, z)$ ($cm^2/molec$), on the
1522 user grids of v (cm^{-1}) and heights, z (km) – an array `knu [nz*nnu]`.

1523 A few comments must be made here regarding the array `knu []`. First, in order to allocate the
1524 elements of an array in memory consecutively, we prefer a 1D array over the 2D one (*Oliveira &*
1525 *Stewart*, 2006: Sec.8.3). Second, the grid of heights z is the lead dimension of the array for
1526 efficiency of the vertical integration performed independently for each v . Third, the MODTRAN
1527 profiles are used. Before calling `kabs (...)`, the array `knu [nz_mod*nnu]` must be allocated
1528 for the number of the MODTRAN points over height `nz_mod`. Fourth and the last one, at present
1529 `nz_mod` = 53 and the user must be careful with the number of the spectral nodes, `nnu`. A
1530 wide spectral range combined with a very fine spectral resolution may lead to insufficient
1531 available memory. Aspect checks that and, if it happens, stops, and notifies the user. The
1532 easiest way to deal with the problem is to split the wide band into a few smaller ones, generate
1533 corresponding LUTs and, if needed, stitch them together into a single big file. Also, using single
1534 precision instead of double saves memory.

1535 The next steps are trivial: for a given v , `aspect` calculates the extinction profile by multiplying
1536 the cross-section and the number concentration profiles (the height grids must match); then it
1537 integrates the extinction over height from TOA to a user-defined level to get the optical thickness
1538 between TOA and the given level (i.e., optical depth). The corresponding element of code in
1539 `aspect` is

```

1540     for (inu = 0; inu < nnu; inu++) {
1541         for (iz = 0; iz < nz_mod; iz++)
1542             ext_km[iz] = knu[inu*nz_mod+iz]*conc_cm3[iz]*1.0e5;
1543         tauabs25(ext_km, zkm_mod, ztau, nzkm, tau_abs);
1544     }

```

1545 The scaling factor $km_to_cm = 1.0e5$ relates cm^{-1} (in k) and km^{-1} (in the grid of heights).

1546 The subroutine `tauabs25` (...) integrates the extinction profile, `ext_km`[nzkm_mod],
 1547 defined on the MODTRAN grid of heights, `zkm_mod`[nzkm_mod], using the two functions
 1548 already explained in Sec.6.2: `simpson`(...) and `intparab`(...). On output, this subroutine
 1549 gives an array, `tau_abs`[nzkm], of optical depths at every user requested height
 1550 `ztau`[nzkm]. For the code simplicity, we assume the user requests optical depths at levels not
 1551 exceeding 25 (km). As Sec.6.1 shows, MODTRAN uses equidistant grid of heights with 1(km)
 1552 step below the 25 (km) threshold. Therefore, it is easy to quickly get the left and right indices of
 1553 the interval of heights containing the user requested altitude. Using these indices, one integrates
 1554 from $z = 25$ (km) to the user level by accumulating Simpson integral and, optionally, trapezoidal
 1555 integral to include the part not covered by Simpson's rule due to the odd vs. even number of
 1556 points.

1557 At and above $z = 25$ (km), `tauabs25` (...) provides the vertical integral from 25 to 120 (km) –
 1558 regardless the user requested level. The 25-120 (km) value is calculated using only Simpson's
 1559 rule for the middle (11 points, 2.5 km step) and top (15 points, 5 km step) atmosphere which are
 1560 added to the final result.

1561 Also, for code simplicity, `tauabs25` (...) loops through the user's heights independently. If the
 1562 user requests many levels, $nzkm \gg 1$, this is inefficient: a lower level includes integral from
 1563 TOA to the level above it. However, our option *a*) helps keep the code simple; *b*) yields
 1564 flexibility: the order of the user's levels is not important; and *c*) is not a bottleneck for the
 1565 runtime – calculation of the Voigt line shape is.

1566 The output result, `tau_abs`[nzkm], is saved either to ASCII or to a binary file as explained in
 1567 Sec.3.3.2. In the former case, `aspect` prints out all values including 0.0. This is convenient for
 1568 visual inspection, debugging, and smaller LUTs. Consider as an example only one HITRAN-
 1569 2020 record for O₂ from Sec.4.2-4.3, default MODTRAN's amount of the gas in atmosphere, US

1570 1976 profile, 4 user defined levels $z = 0, 2, 4, 8$ (km), and 6 user's $v = 13000 + [0.80 : 0.01 :$
1571 $0.85]$ (cm^{-1}). The output file with optical thickness in ASCII format is

```
1572 # nu, zkm = 0.000 2.000 4.000 8.000
1573 0 13000.8000 3.077005e-02 1.877401e-02 1.106013e-02 3.841381e-03
1574 1 13000.8100 3.533850e-02 2.287806e-02 1.461589e-02 6.374547e-03
1575 2 13000.8200 3.425169e-02 2.232654e-02 1.442593e-02 6.519878e-03
1576 3 13000.8300 2.782967e-02 1.723955e-02 1.043387e-02 3.993817e-03
1577 4 13000.8400 2.084901e-02 1.196508e-02 6.532608e-03 1.837301e-03
1578 5 13000.8500 1.554367e-02 8.344352e-03 4.179478e-03 9.014089e-04
```

1579 These numbers are convenient for validation of integration over height because they correspond
1580 to a single HITRAN record.

1581 In the case of binary output file, aspect checks the highest value (lowest level) against a
1582 threshold, τ_{min} , defined in const_param.h (at present, $\tau_{min} = 1.0e-4$ which
1583 corresponds to the vertical one-way monochromatic transmittance of ~ 0.9999). If the highest
1584 thickness does not exceed the threshold, the whole wavenumber is not saved to the binary file.
1585 The check whether to save or skip **tau_abs** [nzkm] is made for each user's v. For that reason,
1586 **tau_abs** [nzkm], does not depend on inu and is small even for a dense user's grid of heights
1587 **zkm** [nzkm].

1588 [6.5 Practical units for water vapor](#)

1589 MODTRAN defines profiles for the particles number concentration in $ppmv$. In practice,
1590 however, different units are commonly used for some molecules: cm (or sometimes mm) of
1591 precipitable liquid water for water vapor (WV), and Dobson units (DU) for O_3 . In this part we
1592 convert the atmospheric columnar amounts of WV from $ppmv$ to cm of precipitated (liquid)
1593 water.

1594 The atmosphere-centimeters shown in **Table 7** for MODTRAN's US 1976 atmosphere
1595 corresponds to aspect's $h = 1766.42$ (cm). It is the height of a column of the water vapor (ideal
1596 gas) at the normal conditions. When the vapor is condensed into the liquid water, the number of
1597 molecules does not change, but the mass density does. Ratios of the mass densities and columns
1598 of water in two physical states are the same:

1599
$$h_{LW} = h_{WV} \frac{\rho_{LW}}{\rho_{WV}} \quad (33)$$

1600 In Eq.(33), the subscript LW means “Liquid Water” and $\rho_{LW} = 1.0 \text{ (g/cm}^3\text{)}$ is the liquid water
 1601 mass density. The water vapor mass density is calculated via scaling the molar mass of the H₂O
 1602 molecule $\mu_{\text{H}_2\text{O}} = 18.01528 \text{ (g/mole)}$ by the number of moles. The latter is computed as the ratio of
 1603 the Loschmidt number⁵¹ $N_L = 2.6867811 \cdot 10^{19} \text{ (molec/cm}^3\text{)}$ and the Avogadro number $N_A =$
 1604 $6.02214129 \cdot 10^{23} \text{ (molec/mole)}$

1605
$$\rho_{WV} = \mu_{\text{H}_2\text{O}} \frac{N_L}{N_A}. \quad (34)$$

1606 Eqs.(33) and (34) result in $\approx 1.42 \text{ (cm)}$ of liquid water for the MODTRAN’s Standard US1976
 1607 atmosphere. Recall, aspect expects the LW amount as input for H₂O.

1608 [6.6 Aspect validation](#)

1609 [6.6.1 Literature references](#)

1610 As for the gas cell, we recommend starting with a visual comparison of the spectral dependencies
 1611 calculated using aspect vs. figures published in literature. This helps catch misunderstandings
 1612 of units, which manifest as wrong order of magnitude. The existence and location of the spectral
 1613 line peaks (or drops in atmospheric transmittance, also called transmission, or transmissivity – in
 1614 the right-most column “Brief description” we borrow the term from the respective source) help
 1615 verify the proper reading and understanding of the HITRAN database. In **Table 9**, we combine
 1616 some references to published images that can be used for validation of separate molecules and
 1617 the whole atmosphere. The list is sporadic, non-exhaustive, and contains references to papers and
 1618 books that we found while working on this paper.

1619

1620 **Table 9:** References to published benchmark images that can be used to test codes like aspect. The
 1621 bottom row “total” refers to results for all gases mixed in atmosphere.

#	Mol.	Ref.	$\approx \Delta\nu \text{ (cm}^{-1}\text{)}$	$\approx \Delta\lambda \text{ (\mu m)}$	Brief description
---	------	------	--	---	-------------------

⁵¹ In 2018, the temperature at which the Loschmidt constant is defined, has changed from 296° to 273.15° (K). Thus its numerical value in legacy and modern codes may differ. If not compensated via ratio of the temperatures, this difference noticeably impacts output (https://en.wikipedia.org/wiki/Loschmidt_constant)

1	H ₂ O	Gao et al., 1993: Fig.2		0.4 - 2.5	Atmospheric water vapor transmittance spectrum, at 10 (nm) resolution, using LOWTRAN7 (Kneizys et al., 1988)
		Goody & Yung, 1995: p.68, p.71	630 – 710 (p.71)	1 - 13 (p.68)	Low-resolution atmospheric absorption spectrum; high-resolution transmission near 14.9 (μm) at 0 (km) and SZA = 30° and terrestrial concentration $\times 0.03$
		Petty, 2006: p.179		0.3 - 50	Zenith transmittance of a midlatitude summertime atmosphere.
		Thorpe et al., 2013: Fig.1		0.5 - 2.5 2.0 - 2.5	Transmittance spectra generated using MODTRAN v.5.3 for a sensor located at 8.9 (km) altitude.
		Yang et al., 2013: Fig.1		0.6 – 0.8	Atmospheric columnar water vapor absorption transmittance calculated using LBLRTM.
		Ibrahim et al., 2018: Fig.1		0.3 – 1.1	Columnar atmospheric transmittance for 3.3 (cm) of water vapor
		Coakley & Yang, 2014: p.157	800 - 900		Total atmospheric water vapor transmission for the 1976 US Standard Atmosphere. The water vapor continuum was not included “ <i>in order to better show the line structure</i> ”.
		Gordon, 2019: p.328		0.4 – 1.0 0.4 – 2.5	Water vapor transmittance in the US Standard Atmosphere at 20 (cm ⁻¹) resolution (p.327)
		Mobley, 2022: Fig. 15.15	300 - 1000		Transmittance by a moist tropical atmosphere at 1 (nm) resolution.
		Docter et al., 2023: Fig. 2		0.6 – 2.35	Atmospheric transmittance.
		Gordon et al., 2022: Fig.3	9000 - 19000		Terrestrial atmospheric transmittance for HITRAN 2020 and 2016.
2	CO ₂	Gao et al., 1993: Fig.2		0.4 – 2.5	Atmospheric carbon dioxide transmittance spectrum, at 10 (nm) resolution, using LOWTRAN7 (Kneizys et al., 1988)

		<i>Goody & Yung, 1995: p.68, p.71</i>	786 – 796 (p.71)	1.5 – 13 (p.68)	Low-resolution atmospheric absorption spectrum; high-resolution transmission near 12.64 (μm) at 15 (km) and SZA = 30° and terrestrial concentration $\times 10$.
		<i>Bohren & Clothiaux, 2006: Fig.2.22</i>	746 - 758 756.5 - 758.0 1074 - 1086 1082.0-1082.75		Absorptivity along a vertical path for a Mid-latitude Summer atmosphere and 4 different concentrations of carbon dioxide; note non-zero values for 0 (ppm) of CO ₂ .
		<i>Petty, 2006: p.179</i>		0.3 - 50	Zenith transmittance of a midlatitude summertime atmosphere.
		<i>Docter et al., 2023: Fig. 2</i>		0.6 – 2.35	Atmospheric transmittance.
3	O ₃	<i>Gao et al., 1993: Fig.3</i>		0.4 – 2.5	Atmospheric ozone transmittance spectrum, at 10 (nm) resolution, using LOWTRAN7 (Kneizys et al., 1988)
		<i>Goody & Yung, 1995: pp. 68 & 72</i>	1039 – 1041 (p.72)	3.5 – 15.5 (p.68)	Low-resolution atmospheric absorption spectrum; high-resolution transmission near 9.61 (μm) at 30 (km) and SZA = 30°.
		<i>Petty, 2006: p.179</i>		0.3 - 50	Zenith transmittance of a midlatitude summertime atmosphere.
		<i>Ibrahim et al., 2018: Fig.1</i>		0.3 – 1.1	Columnar atmospheric transmittance for 277 DU of ozone
		<i>Gordon, 2019: p.329</i>		0.4 – 0.8	Ozone transmittance in the US Standard Atmosphere.
		<i>Mobley, 2022: Fig. 15.16</i>	300 - 1000		Vertical atmospheric transmittance for 200, 350, and 500 DU. Strong absorption in the Blue-UV band, not available from HITRAN's LBL database, is visible.
4	N ₂ O	<i>Gao et al., 1993: Fig.3</i>		0.4 – 2.5	Atmospheric nitrous oxide transmittance spectrum, at 10 (nm) resolution, using LOWTRAN7 (Kneizys et al., 1988)

		<i>Goody & Yung, 1995: p.68, p.70, p.96</i>	1245 - 1325 (p.70) 1160.0 – 1160.6 (p.96)	2 – 9.5 (p.68)	Low-resolution atmospheric absorption spectrum (p.68); high-resolution transmission near 7.78 (μm) at 15 (km) and SZA = 30° (p.70); ultra-high resolution transmission for “ <i>physical conditions very different from those occurring in Earth’s atmosphere</i> ” (also useful for gas cell validation).
		<i>Petty, 2006: p.179</i>		0.3 - 50	Zenith transmittance of a midlatitude summertime atmosphere.
		<i>Coakley & Yang, 2014: p.153</i>	1120 - 1220		N_2O transmissivity near 8.6 (μm) for 1976 US Standard Atmosphere, HITRAN 2008, at ground level for SZA = 0°.
5	CO	<i>Gao et al., 1993: Fig.3</i>		0.4 – 2.5	Atmospheric carbon monoxide transmittance spectrum, at 10 (nm) resolution, using LOWTRAN7 (Kneizys et al., 1988)
		<i>Goody & Yung, 1995: p.68, p.70</i>	2102 - 2182 (p.70)	2 – 6 (p.68)	Low-resolution atmospheric absorption spectrum; high-resolution transmission near 4.67 (μm) at 10 (km) and SZA = 30°.
		<i>Petty, 2006: p.179</i>		0.3 - 50	Zenith transmittance of a midlatitude summertime atmosphere.
6	CH ₄	<i>Gao et al., 1993: Fig.3</i>		0.4 – 2.5	Atmospheric methane transmittance spectrum, at 10 (nm) resolution, using LOWTRAN7 (Kneizys et al., 1988)
		<i>Goody & Yung, 1995: p.68, p.69</i>	2874 – 2946 2904 - 2908	1.5 – 8.5 (p.68)	Low-resolution atmospheric absorption spectrum (p.68); and medium and high-resolution transmission spectra near 3.44 (μm) at 10 (km) above the ground for SZA = 30° (p.69)
		<i>Petty, 2006: p.179</i>		0.3 - 50	Zenith transmittance of a midlatitude summertime atmosphere.
		<i>Thorpe et al., 2013: Fig.1</i>		0.5 - 2.5 2.0 - 2.5	Transmittance spectra generated using MODTRAN v.5.3 for a sensor located at 8.9 (km) altitude.
		<i>Docter et al., 2023: Fig. 2</i>		0.6 – 2.35	Atmospheric transmittance.

7	O_2	<i>Gao et al., 1993: Fig.3</i>		0.4 – 2.5	Atmospheric oxygen transmittance spectrum, at 10 (nm) resolution, using LOWTRAN7 (Kneizys et al., 1988)
		<i>Goody & Yung, 1995: p.196</i>	842 - 7922		IR atmospheric band of molecular oxygen near 1.27 (μm) based on AFGL data at 0 (km) and SZA = 30°.
		<i>Pfeilsticker et al., 1998: Fig. 2</i>		0.768 – 0.772 (A-band)	Direct Sun observations of the atmospheric O_2 A-band at different solar zenith angles.
		<i>Stam et al., 2000: Figs.1, 2(a), & 3</i>		0.755 - 0.775 0.765 - 0.766	Fig.1: Molecular scattering and absorption columnar optical thickness based on HITRAN-92 for the A-band. Fig.2(a): Like Fig.1 but for a narrow band $\Delta\lambda = 1$ (nm) resolves peaks from the isotope minorities. Fig.3: Like Fig.2(a) but for absorption cross-section as a function for 0 (km) and 30 (km) with specified temperature and pressure (also useful for gas cell validation).
		<i>Petty, 2006: p.179</i>		0.3 - 50	Zenith transmittance of a midlatitude summertime atmosphere.
		<i>Nowlan et al., 2007: Figs.1, 3</i>		0.690 – 0.692 0.680 – 0.700 0.755 – 0.780	A- and B-bands cross-sections (Figs. 1 & 3) and transmittances (Fig.1 only) in atmosphere at 0, 30 (A-band only), and 50 (km); temperature and pressure are specified (also useful for gas cell validation).
		<i>Natraj et al., 2007: Fig.1</i>	12,995 - 13,020		Atmospheric columnar optical depth calculated using HITRAN 2000; corresponding Rayleigh optical depth is also shown.
		<i>Gordon et al., 2011: Figs. 2 & 4</i>	15,050 - 15,930 14,496 - 14,504		Oxygen B- and γ -bands: atmospheric transmittance.

		<i>Yang et al., 2013: Figs.1 & 2(ab)</i>		0.6 - 0.8	Oxygen transmittance in the A- and B -bands (Fig.1). Figs. 2(a) and 2(b) show details for the A- and B-bands, respectively.
		<i>Ibrahim et al., 2018: Fig.1</i>		0.3 – 1.1	Columnar transmittance for tropical atmosphere.
		<i>Mobley, 2022: Fig. 15.15</i>	300 - 1000		Atmospheric columnar transmittance at 1 (nm) resolution.
10	NO ₂	<i>Ibrahim et al., 2018: Fig.1</i>		0.3 – 1.1	Columnar transmittance for tropical atmosphere
		<i>Gordon, 2019: p.328</i>		0.35 – 0.90	Columnar transmittance for the US 1976 Standard Atmosphere.
		<i>Mobley, 2022: Fig. 15.17</i>	300 - 1000		Vertical atmospheric for low, typical, and high concentrations of NO ₂ .
-	Total	<i>Goody & Yung, 1995: p.4</i>		0.1 - 100	Atmospheric absorption at ground level and at 11 (km)
		<i>Petty, 2006: p.179</i>		0.3 - 50	Zenith transmittance of a midlatitude summertime atmosphere.
		<i>Bohren & Clothiaux, 2006: Fig.2.13</i>		0.1 (μm) – 10 (cm)	Atmospheric transmissivity along a vertical path in a very broad band. There are 6 panels, each panel is one wavelength decade - hence the top covered limit: 10 centimeters . Ozone absorption, not included in our HITRAN-based LBL calculations, is visible in the 0.1 (μm) – 1 (μm) panel.
		<i>Thompson et al., 2015: Fig.1</i>		0.4 – 2.4	Atmospheric transmittance due to atmospheric gases.
		<i>Ibrahim et al., 2018: Fig.1</i>		0.3 – 1.1	Tropical atmosphere transmittance for 3.3 (cm) of H ₂ O, 277 DU of O ₃ , O ₂ , and NO ₂ combined.
		<i>Gordon, 2019: p.329</i>		0.4 – 1.0 0.4 – 2.5	Columnar transmittance for the US Standard Atmosphere.

		<i>Chen et al., 2021: Fig.2(a)</i>		0.25 - 2.50	Atmospheric transmittance in the Solar reflectance band. Note, the ozone absorption at wavelength shorter than 700 (nm) is not included in HITRAN, hence, in our paper as well.
--	--	------------------------------------	--	-------------	---

1622

1623 Once the user has verified the order of magnitude, it is time for accurate numerical comparison
 1624 vs. tools mentioned in the Introduction. With this paper, we distribute our numbers for the
 1625 oxygen A-band and methane optical thickness integrated from TOA to several levels in the
 1626 atmosphere (see Sec. 3.2.2).

1627 [6.6.2 Numerical validation of atmospheric absorption](#)

1628 This section presents examples of numerical validation of `aspect` against another code
 1629 (*Ibrahim et al., 2018*) simulating LBL atmospheric absorption spectroscopy for the PACE-OCI
 1630 instrument. That code, assumed benchmark, was developed independently of `aspect`. It is a
 1631 completely refactored and updated version of the ATREM code (*Gao et al., 1993; Thompson et*
 1632 *al., 2015*). Two key modifications in the benchmark code include the translation from Fortran
 1633 into Python and the use of the HAPI tool (*Kochanov et al., 2016*) for simulating the absorption
 1634 cross-section k ($cm^2/molec$) at a given temperature, pressure (i.e., in a layer at a specific altitude)
 1635 and for the Voigt line shape via the `absorptionCoefficient_Voigt(...)` function. The
 1636 wing cut-off was set to 25 (cm^{-1}).

1637 Like `aspect`, the benchmark code uses prescribed MODTRAN atmospheric profiles with 50
 1638 boundaries; however, the calculation of optical thickness τ differs. The benchmark code models
 1639 the atmosphere as consisting of 49 layers, where pressure, temperature, and particles number
 1640 concentrations are assumed constant in each layer and calculated as the average of those at the
 1641 layer boundaries. Thus, the atmosphere is treated as a vertical stack of gas cells, whose
 1642 absorption properties can be tested using `gcell`. The atmospheric optical thickness is then
 1643 accumulated from TOA to BOA or to any desired altitude in the atmosphere. For tests presented
 1644 in this section, both codes calculated $\tau(v)$ in LBL mode with a spectral resolution $\Delta v = 0.01 (cm^{-1})$, using MODTRAN US 1976 atmospheric profile (Sec.6.1) and HITRAN-2020 edition. We

1646 considered absorption by two molecules: H₂O within 550-900 (*nm*) and O₂ in the B- and A-
1647 bands: 680-700 and 750-780 (*nm*), respectively. We ignored continuum for both.

1648 To provide a practical perspective for our comparison and to enhance visual clarity, we compare
1649 the total atmosphere one-way vertical transmittance within the PACE-OCI instrument bands as
1650 defined by Eq.(25). The OCI relative spectral response functions (RSRs) are available from the
1651 NASA GSFC Ocean Color website⁵² in a netCDF file. All RSRs are defined on the same grid of
1652 20926 equidistant wavelength points beginning at 306 (*nm*) with 0.1 (*nm*) step. **Fig.8** shows the
1653 RSRs for all OCI bands, however, we are interested only in “hyperspectral” mode which extends
1654 up to ~894(*nm*), with 5 (*nm*) resolution bandwidth (full width at half maximum), and spectral
1655 steps 2.5 (*nm*) (between band centers) for most bands and 1.25 (*nm*) for a few.

1656 In addition to the RSRs, **Fig.8** also shows the solar spectral irradiance normalized to its
1657 maximum value, $\approx 2.4 (W m^{-2} nm^{-1})$. For this, we use a new solar irradiance reference spectrum
1658 recently published by *Coddington et al. (2023)*. The solar spectrum is available online⁵³ for the
1659 wavelength range from 202 (*nm*) to 2730 (*nm*), with native (unconvolved) spectral resolution
1660 0.001 (*nm*), as reported in `hybrid_reference_spectrum_c2022-11-`
1661 `30_with_unc.nc` file, which we use in our calculations.

1662 Since both the solar irradiance spectrum and RSRs are defined in the wavelength domain, we
1663 integrate Eq. (25) over λ . This requires converting the HITRAN-LBL absorption optical
1664 thickness from wavenumbers to wavelengths, and then interpolating between different
1665 wavelength grids. The constant step $\Delta\nu = 0.01 (cm^{-1})$ for the HITRAN-LBL calculations
1666 corresponds to a step $\Delta\lambda$ not exceeding 0.001 (*nm*) for $\lambda < 1000 (nm)$. Therefore, we interpolate
1667 the solar spectrum and hyperspectral RSRs from their wavelength grid to match that of LBL τ .
1668 We developed a Python script for cubic interpolation and Simpson integration, and used it for
1669 both `aspect` and benchmark LBL data. This ensures that no discrepancies arise from
1670 interpolation and integration in Eq. (25).

⁵² https://oceancolor.gsfc.nasa.gov/images/data/PACE OCI L1B LUT_RSR_baseline_1.1.1.nc

⁵³ https://lasp.colorado.edu/lisird/data/tsis1_hsrsp1nm

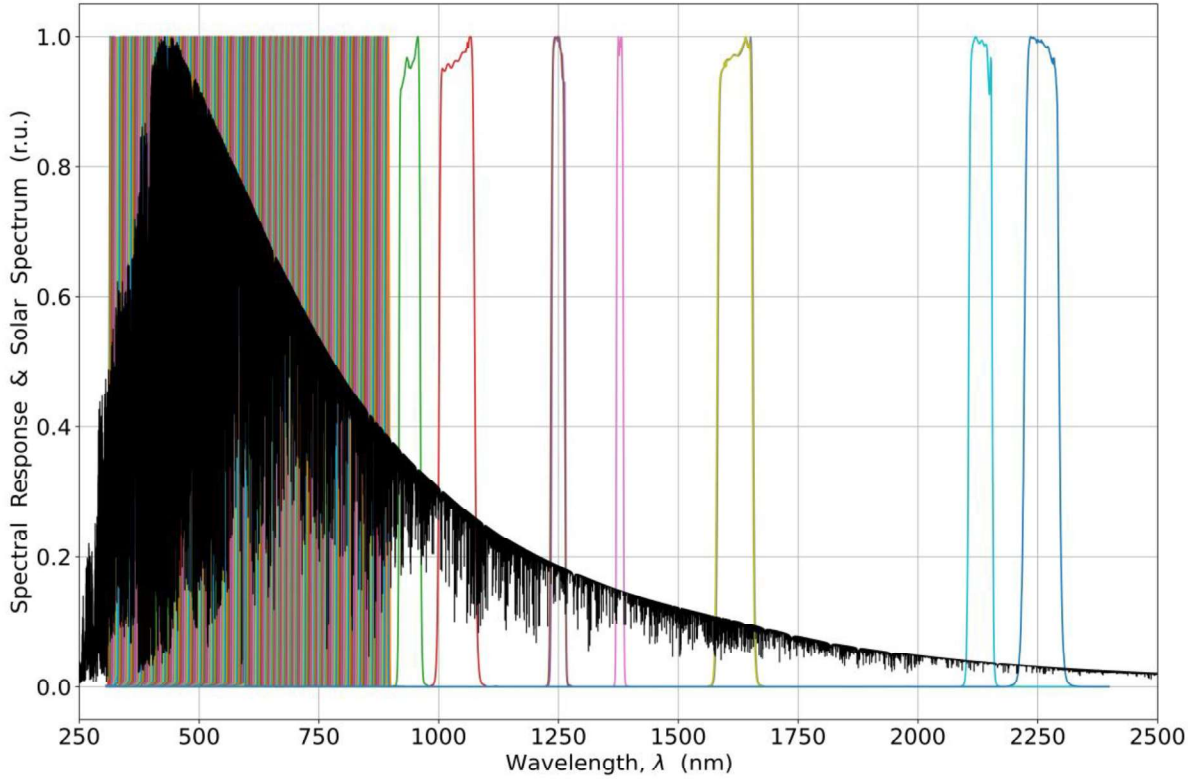


Fig.8: PACE-OCI RSRs (colored lines) and solar spectrum (black) normalized to its maximum value $\approx 2.4 (W m^{-2} nm^{-1})$. The multiple colored bands below 900 (nm) correspond to the hyperspectral mode.

1671

1672 **Fig.9(a)** compares one-way vertical transmittances, expressed as percentages (%), where 100%
 1673 corresponds to total transparency ($T = 1$), within OCI bands for 0.5 and 5 (cm) of liquid water.
 1674 **Fig.9(b)** shows the absolute difference between `aspect` and the benchmark code in the same
 1675 percentage units. Given the different approaches to simulating absorption cross-sections (self-
 1676 coded vs. HAPI) and to vertical integration (Simpson rule vs. layer-averaged) in `aspect` and
 1677 the benchmark code, we are satisfied with the result.

1678 **Fig.9(c)** compares true `aspect` calculations with those obtained through linear scaling of
 1679 absorption optical thickness in the same code:

1680
$$\tau_{WV}(\nu) = \frac{LW}{LW_{Std}} \tau_{Std}(\nu), \quad (35)$$

1681 where $LW_{Std} \approx 1.4197655$ (cm) is the amount of water vapor condensed into a liquid for the
 1682 standard MODTRAN US 1976 atmosphere, $\tau_{Std}(\nu)$ is the LBL optical thickness calculated for
 1683 the same, and LW is the user-defined amount (e.g., 0.5 or 5 (cm) in our examples, as shown in

1684 **Fig.9).** This simple scaling is convenient for retrievals; however, it must be treated with caution
 1685 depending on the absorption characteristics of the media (strong absorption lines and/or large
 1686 amount of absorbent). We refer the reader to Eq.(12) in *Gueymard* (2001) for one modification
 1687 of the scaling rule, Eq. (35).

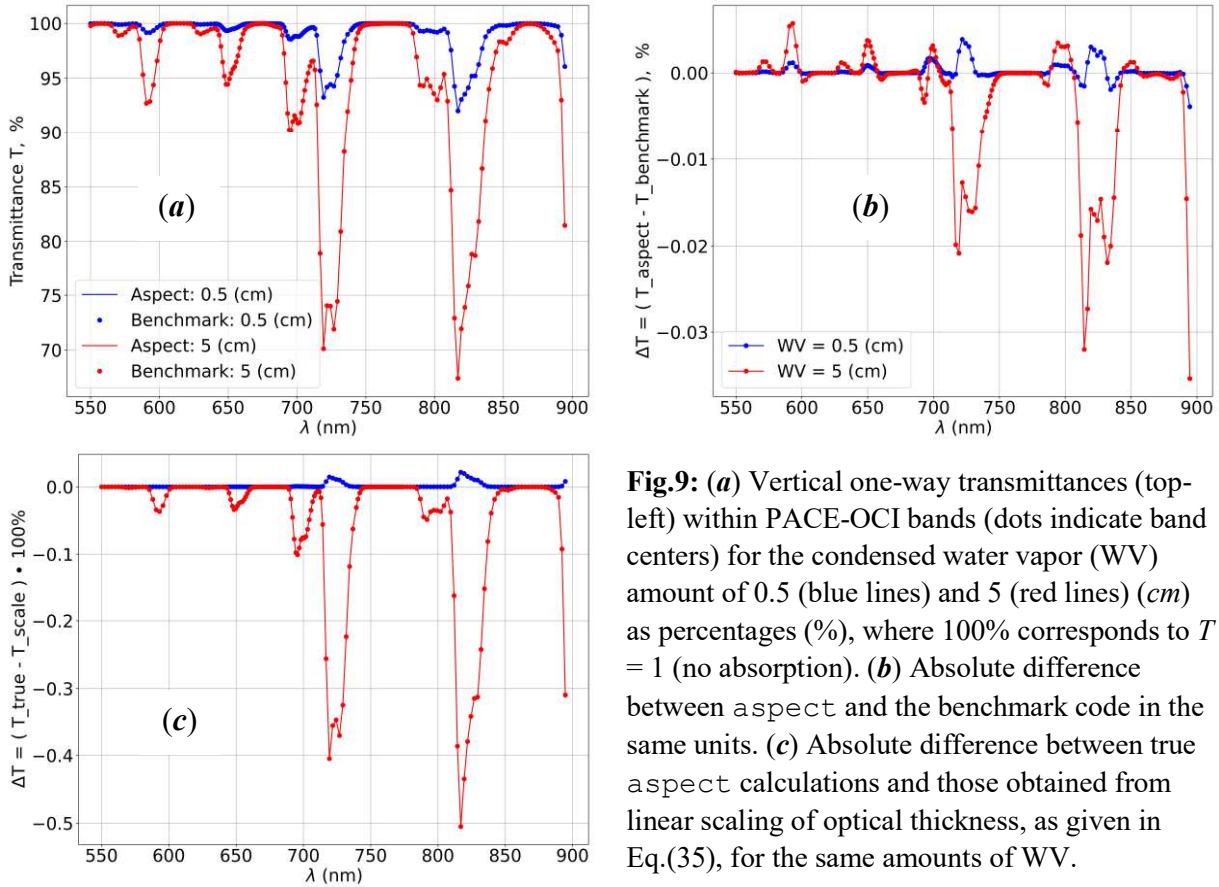


Fig.9: (a) Vertical one-way transmittances (top-left) within PACE-OCI bands (dots indicate band centers) for the condensed water vapor (WV) amount of 0.5 (blue lines) and 5 (red lines) (cm) as percentages (%), where 100% corresponds to $T = 1$ (no absorption). (b) Absolute difference between aspect and the benchmark code in the same units. (c) Absolute difference between true aspect calculations and those obtained from linear scaling of optical thickness, as given in Eq.(35), for the same amounts of WV.

1688

1689 **Fig.10** shows another comparison of aspect versus the benchmark code for O₂ B- and A-
 1690 bands, shown in the left and right charts, respectively. As in **Fig.9**, we plot one-way vertical
 1691 transmittance as percentages (%) (left y-axes) and the absolute difference in the simulated
 1692 transmittances between the two codes (right y-axes), also expressed as percentages (%). Like in
 1693 Fig.9 (b), we attribute the difference to different approaches to simulating absorption cross-
 1694 sections and to its vertical integration. To confirm this, we applied the Simpson integration from
 1695 Python's `scipy.integrate` package (hence independently developed by experts) in the
 1696 benchmark HAPI-based code. The pattern of the deviation remained the same; however, the
 1697 maximum deviation decreased by factors of 5 and 3 in the B- and A-bands, respectively.

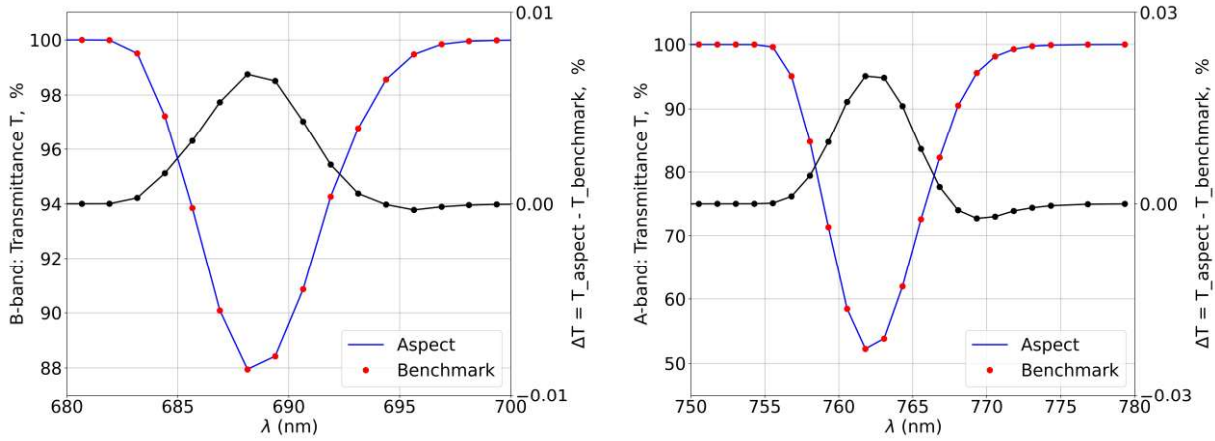


Fig.10: Comparison of one-way vertical transmittance in O₂ B (left image) and A (right image) bands. Red dots in the benchmark results correspond to PACE-OCI RSR band centers, while aspect results are shown with continuous blue lines for better visual perception. In each of the two charts, left y-axes show the absolute values of the transmittances, while the right y-axes show the absolute difference between aspect and benchmark codes.

1700 For the cases considered in **Figs. 9** and **10**, we have prepared five `txt` files with LBL values of
 1701 absorption optical thickness, which are distributed with our code in the `./benchmarks/`
 1702 folder. Three of the files correspond to H₂O at 0.5, ≈ 1.42 (standard atmosphere), and 5 (cm) of
 1703 liquid; the other two correspond to the oxygen A- and B-bands, as indicated in their respective
 1704 file names. The optical thickness is calculated at 0, 1, 2.5, and 8 (km) altitudes; figures in this
 1705 section show results for BOA, 0 (km). Structure of each file is explained in Sec.3.2.2 above. We
 1706 used `aspect` to prepare the `txt` files.

1707 7. Conclusion

1708 Following our published “A practical guide to writing a radiative transfer code”, this paper
 1709 explains the development of a code for line-by-line trace gas absorption in Earth atmosphere
 1710 within the solar reflectance band, 250-2500 (nm). We focus on the code, as opposed to
 1711 theoretical background or practical applications, thoroughly discussed elsewhere. We start by
 1712 reading the HITRAN database and simulate absorption by a single spectral line. Then we
 1713 consider absorption by many lines in a gas cell at a given temperature and pressure. Finally,
 1714 using the MODTRAN profiles, we simulate atmospheric absorption at user-defined altitudes.
 1715 This sequence deals with one problem at a time: reading and understanding HITRAN,

1716 calculation of absorption for fixed thermodynamic conditions in a gas cell (code `gcell`), and
1717 lastly dealing with atmospheric profiles in the code `aspect`. In terms of the code text, `gcell`
1718 and `aspect` largely overlap.

1719 Unlike the mentioned “guide to writing a radiative transfer code”, which shows an entire scalar
1720 plane-parallel RT code, the current paper explains only key parts of each program. All the source
1721 codes and test data are available from the journal website and from our GitHub repository⁵⁴. The
1722 sources are carefully commented. In this paper, we pay particular attention to unit testing and
1723 provide numerical and graphical material for debugging. We believe this detailed explanation
1724 leads to a thorough understanding of our software. This, in its turn, should simplify the
1725 completion of the basic tasks (e.g., the replacement for the current HITRAN database with a
1726 newer version, or vice versa, reproducing results with an older version), moderate modification
1727 of the code (acceleration of the *Humlíček* convolution algorithm; updating TIPS; adding a new
1728 molecule or profile; account for the wavenumber shift due to refractive index of air, which
1729 changes with height, as opposed to the HITRAN's line positions in vacuum), and fundamental
1730 changes (eventual replacement of the Voigt line shape with the speed-dependent Voigt, or other
1731 “beyond Voigt” models of line shape). The mentioned changes become necessary when one
1732 faces the everlasting question: “is this effect important in my case?”. And even if numerical
1733 simulation proves that no changes are required so far, our approach assures confident
1734 exploitation of the code over time and smooth transition of knowledge between generations of
1735 atmospheric scientists.

1736 Both our “practical guide”-papers differ from most scientific papers because they do not present
1737 new information but rather act as an instructive resource to present necessary but disparate
1738 materials that are not often discussed together in a practically convenient form of “get to coding
1739 quickly”. Repeating our “RT guide”, we say here that a real understanding of how software
1740 applications of a general type of work is, in most cases, truly only attainable by developing your
1741 own. We encourage the reader to use our presented open-source scripts as an example to aid their
1742 understanding and a basis to develop tools for their own needs, and not merely as a shortcut.

⁵⁴ https://github.com/korkins/aspect_gcell

1743 Naturally, this paper and code have many limitations. We have restricted ourselves to absorption
1744 in spectral lines under conditions typical for the Earth environment – the area of our expertise.
1745 We take the line parameters from only one database – HITRAN. The main part of the HITRAN
1746 database simulates the line shape using convolution of the Doppler and Lorentzian contours – the
1747 Voigt profile. We mentioned above that we didn't go “beyond Voigt”: e.g., the speed
1748 dependence (affecting the Doppler contour) and line mixing effects (affecting the Lorentzian
1749 contour) are not considered. We have hard-coded atmospheric profiles from MODTRAN.
1750 Therefore, our program is not ready for profile retrieval. Most importantly, we do not consider
1751 spectrally smooth absorption, like water vapor or ozone continuum. Hence, our tools cannot be
1752 used for ozone correction or in the microwave. We skip collision induced absorption (CIA),
1753 which seems important for cloud top height retrieval in the oxygen A-band. The number of gas
1754 species is limited to only the first few from a long HITRAN list.

1755 Each limitation comes for a reason. Due to different theoretical backgrounds and scaling of the
1756 LBL and continuum-type absorption, e.g., for variations of temperature and pressure, it makes
1757 little sense to combine LBL and continuum in one program. Parameters for CIA are still not
1758 included in the “main” HITRAN database but come as separate ones. Same for non-Voigt line
1759 shapes. In order to partially close the gap in capabilities, we provide a broad list of literature
1760 references, 186 items, including some from the XIX-th century to give a historical perspective.
1761 Separate sections of our papers are devoted to the effects that we have dropped and to multiple
1762 tools for atmospheric spectroscopy that have been developed – many as open source, some with
1763 tutorial goal in developers' mind. We encourage the reader to study literature focusing on their
1764 spectral band, as well as the light source (e.g., Sun vs. laser) and figure out what effects are
1765 important, and what are not so. One common reason for all the limitations was to balance the
1766 simplicity of our codes with their practical value.

1767 As to the limitations on the list of molecules, we believe our explanation of the source code
1768 bundled with theoretical background will help potential users to build-in and test any molecule
1769 from the HITRAN list quickly yet confidently. Our belief is based on the feedback to our
1770 proposal “The paper-and-code bundle as a new paradigm supporting the TOPS initiative in Earth
1771 Science” (NASA ROSES-22 program element F.15 High Priority Open-Source Science:
1772 NNH22ZDA001N-HPOSS). Although we received no funding from the program, the

1773 “selectable” status and overall positive review encouraged us to find extra time and finish this
1774 work, as proposed, but largely on a volunteer basis.

1775 Acknowledgements

1776 The authors are grateful to Laurence Rothman, Iouli Gordon (Harvard, USA) and the broader
1777 HITRAN team for the years of work developing and maintaining the database and associated
1778 resources. Sergey Korkin and Alexei Lyapustin thank Larry Gordley, Tom Marshall, and the
1779 GATS Inc. team (USA) for sharing numerical results discussed in Sec.5.3.2 “Methane band at
1780 2.3 (μm)”. Andrew M. Sayer thanks Keith Shine and Jon Elsey (University of Reading, UK) for
1781 useful discussions which aided our understanding of the history and conventions of line shape
1782 models, and Luca Lelli (DLR, Germany) for independent verification of some numerical results
1783 from his implementation of absorption line code. Sergey Korkin, Andrew M. Sayer, and Amir
1784 Ibrahim are thankful to Bo-Cai Gao (Naval Research Laboratory, USA) for help with
1785 understanding of the nature of “minor” lines in the oxygen absorption (see arrows in **Fig.4(a)**;
1786 private communication, May 2020). OpenAI’s ChatGPT helped us create Makefiles for our
1787 codes; it also helped the first author with the initial editing of the text, although submitted and
1788 revised texts have been independently and fully checked by the authors.

1789 Sergey Korkin thanks the Richard M. Goody Award Selection Committee for their decision,
1790 anonymous colleagues for their nomination, and numerous fellow workers collaboration with
1791 whom resulted in the 2016 Award.

1792 Authors contribution

1793 SK: original draft and development of codes `gcell` and `aspect`; AMS: critical revision and
1794 editing of the original draft, numerical validation of intermediate results in `gcell`; AI:
1795 development of HAPI-based Python code for atmospheric absorption spectroscopy and
1796 validation of `aspect` results; AL: development of the original SHARM-IPC package, which
1797 LBL part we have refactored and updated in the current paper; funding acquisition for SK. All:
1798 review and editing of the manuscript.

1799 **Funding information**

1800 This work received no target funding (see Conclusion: last paragraph). However, the work of S.
1801 Korkin was partially supported by NASA Atmosphere Observing System (AOS) mission; the
1802 work of A. Lyapustin and S. Korkin was partially supported by NASA VIIRS, DSCOVR, and
1803 PACE programs via respective ROSES proposals (PI: A. Lyapustin); the work of A. M. Sayer
1804 and A. Ibrahim was partially supported by NASA PACE Project Science.

1805 **References**

1806 See separate file.

References¹

1. Abrarov S. M. and Quine B. M., "Sampling by incomplete cosine expansion of the sinc function: Application to the Voigt/complex error function", *Applied Mathematics and Computation*, **258**, pp. 425-435, 2015. doi: <https://doi.org/10.1016/j.amc.2015.01.072>
2. Adorf C.S., Ramasubramani V., Anderson J. A., and Glotzer S.C., "How to Professionally Develop Reusable Scientific Software—And When Not To", *Computing in Science & Engineering*, **21** (2), pp. 66-79, 2019. doi: <https://doi.org/10.1109/MCSE.2018.2882355>
3. Amato U., Masiello G., Serio C., and Viggiano M., "The σ -IASI code for the calculation of infrared atmospheric radiance and its derivatives", *Environmental Modelling & Software*, **17** (7), pp. 651–667, **2002**. doi: [https://doi.org/10.1016/S1364-8152\(02\)00027-0](https://doi.org/10.1016/S1364-8152(02)00027-0)
4. Armstrong B.H., "Spectrum line profiles: The Voigt function," *Journal of Quantitative Spectroscopy and Radiative Transfer*, **7** (1), pp. 61-88, 1967. doi: [https://doi.org/10.1016/0022-4073\(67\)90057-X](https://doi.org/10.1016/0022-4073(67)90057-X)
5. Arrhenius S., "On the influence of carbonic acid in the air upon the temperature of the ground", *Philosophical Magazine and Journal of Science*, **41** (251), pp. 237-276, 1896. doi: <https://doi.org/10.1080/14786449608620846>
6. Arrhenius S., "On the influence of carbonic acid in the air upon the temperature of the Earth," *Publications of the Astronomical Society of the Pacific*, **9** (54), pp. 14-24, 1897. <https://www.jstor.org/stable/40670917>
7. Bailey J. and Kedziora-Chudczer L., "Modelling the spectra of planets, brown dwarfs and stars using vstar", *Monthly Notices of the Royal Astronomical Society*, **419** (3), pp.1913-1929, 2012. doi: <https://doi.org/10.1111/j.1365-2966.2011.19845.x>
8. Baldridge A.M., Hook S.J., Grove C.I., and Rivera G., "The ASTER spectral library version 2.0", *Remote Sensing of Environment*, **113** (4), pp. 711-715, 2009. doi: <https://doi.org/10.1016/j.rse.2008.11.007>
9. Berk A., Conforti P., Kennett R., Perkins T., Hawes F., and van den Bosch J., "MODTRAN® 6: A major upgrade of the MODTRAN® radiative transfer code", *6th Workshop on Hyperspectral Image and Signal Processing: Evolution in Remote Sensing*, pp. 1-4, 2014. doi: <https://doi.org/10.1109/WHISPERS.2014.8077573>
10. Berk A. and Hawes F., "Validation of MODTRAN®6 and its line-by-line algorithm," *Journal of Quantitative Spectroscopy and Radiative Transfer*, **203**, pp. 542-556, 2017. doi: <https://doi.org/10.1016/j.jqsrt.2017.03.004>
11. Berk A., J. van den Bosch J., Hawes F., Perkins T., Conforti P. F., Acharya P.K., Anderson G.P., and Kennett R.G., *MODTRAN 6.0 User's Manual*. Kirtland AFB, NM: Air Force Research Laboratory, 2019.
link: [https://wiki.harvard.edu/confluence/download/attachments/301915384/MODTRAN 6 User's Manual.pdf](https://wiki.harvard.edu/confluence/download/attachments/301915384/MODTRAN%206%20User's%20Manual.pdf)

¹ We refer to papers with 10+ authors by name of the first author and "Coauthors".

12. Bernath P. F., Steffen J., Crouse J., Boone C.D., Sixteen-year trends in atmospheric trace gases from orbit, *Journal of Quantitative Spectroscopy and Radiative Transfer*, 253, 107178, 2020. doi: <https://doi.org/10.1016/j.jqsrt.2020.107178>
13. Bertaux J.L., Lallement R., Ferron S., Boonne C., and Bodichon R., “TAPAS, a web-based service of atmospheric transmission computation for astronomy”, *Astronomy & Astrophysics*, **564**, A46, 2014. doi: <https://doi.org/10.1051/0004-6361/201322383>
14. Binkley D., Davis M., Lawrie D., and Morrell C., "To camelcase or under_score", IEEE 17th International Conference on Program Comprehension, Vancouver, BC, Canada, pp. 158-167, 2009. doi: <https://doi.org/10.1109/ICPC.2009.5090039>
15. Bogumil K. and Coauthors, “Measurements of molecular absorption spectra with the SCIAMACHY pre-flight model: instrument characterization and reference data for atmospheric remote-sensing in the 230–2380 nm region”, *Journal of Photochemistry and Photobiology A: Chemistry*, **157** (2–3), pp.167-184, 2003.
doi: [https://doi.org/10.1016/S1010-6030\(03\)00062-5](https://doi.org/10.1016/S1010-6030(03)00062-5)
16. Bohren C. F., and Clothier E. E., *Fundamentals of Atmospheric Radiation: An Introduction with 400 Problems*, Wiley, 2006.
doi: <https://onlinelibrary.wiley.com/doi/book/10.1002/9783527618620>
17. Boone C.D., Walker K.A., and Bernath P.F., “Speed-dependent Voigt profile for water vapor in infrared remote sensing applications”, *Journal of Quantitative Spectroscopy and Radiative Transfer*, **105** (3), pp. 525–532, 2007. doi: <https://doi.org/10.1016/j.jqsrt.2006.11.015>
18. Boone C.D., Walker K.A., and Bernath P.F., “An efficient analytical approach for calculating line mixing in atmospheric remote sensing applications”, *Journal of Quantitative Spectroscopy and Radiative Transfer*, **112** (6), pp. 980–989, 2011.
doi: <https://doi.org/10.1016/j.jqsrt.2010.11.013>
19. Bourassa A.E., Degenstein D.A., and Llewellyn E.J., “SASKTRAN: A spherical geometry radiative transfer code for efficient estimation of limb scattered sunlight”, *Journal of Quantitative Spectroscopy and Radiative Transfer*, **109** (1), pp. 52-73, 2008.
doi: <https://doi.org/10.1016/j.jqsrt.2007.07.007>
20. Böhlke J. K., de Laeter J. R., De Bièvre P., Hidaka H., Peiser H. S., Rosman K. J. R., and Taylor P. D. P., “Isotopic Compositions of the Elements, 2001”, *Journal of Physical and Chemical Reference Data*, **34** (1), pp. 57 - 67, 2005. doi: <https://doi.org/10.1063/1.1836764>
21. Buehler S.A., Mendrok J., Eriksson P., Perrin A., Larsson R., and Lemke O., “ARTS, the Atmospheric Radiative Transfer Simulator – version 2.2, the planetary toolbox edition”, *Geoscientific Model Development*, **11** (4), pp. 1537-1556, 2018.
doi: <https://doi.org/10.5194/gmd-11-1537-2018>
22. Burch D.E., “Continuum absorption by H₂O”, AFGL Technical Report, 1982.
link: <https://apps.dtic.mil/sti/citations/ADA112264>
23. Carissimo A., De Feis I., and Serio C., “The physical retrieval methodology for IASI: the δ -IASI code”, *Environmental Modelling & Software*, **20** (9), pp. 1111-1126, 2005.
doi: <https://doi.org/10.1016/j.envsoft.2004.07.003>

24. Chance K. and Kurucz R.L., “An improved high-resolution solar reference spectrum for earth's atmosphere measurements in the ultraviolet, visible, and near infrared”, *Journal of Quantitative Spectroscopy and Radiative Transfer*, **111** (9), pp.1289-1295, 2010.
doi: <https://doi.org/10.1016/j.jqsrt.2010.01.036>

25. Chapman I.M., Naylor D., Gom B.G., Querel R.R., and Davis-Imhof P., “BTRAM : An Interactive Atmospheric Radiative Transfer Model” in *The 30th Canadian Symposium on Remote Sensing*, pp. 22–25, 2010. link: <https://blueskyspectroscopy.com/>

26. Chen W., Ren T., and Zhao C., “A machine learning based model for gray gas emissivity and absorptivity of H₂O-CO₂-CO-N₂ mixtures”, *Journal of Quantitative Spectroscopy and Radiative Transfer*, **312**: 108798, 2024. doi: <https://doi.org/10.1016/j.jqsrt.2023.108798>

27. Chen X. and Coauthors, “First retrieval of absorbing aerosol height over dark target using TROPOMI oxygen B band: Algorithm development and application for surface particulate matter estimates”, *Remote Sensing of Environment*, **265**, 112674, 2021.
doi: <https://doi.org/10.1016/j.rse.2021.112674>

28. Clough S.A., Kneizys F.X., Rothman L.S., and Gallery W.O., “Atmospheric Spectral Transmittance And Radiance: FASCOD1B”, *Proceedings of SPIE*, **277**, pp. 152–166, 1981.
doi: <https://doi.org/10.1117/12.931914>

29. Clough S.A., Kneizys F.X., and Davies R.W., “Line shape and the water vapor continuum,” *Atmospheric Research*, **23** (3-4), pp. 229–241, 1989.
doi: [https://doi.org/10.1016/0169-8095\(89\)90020-3](https://doi.org/10.1016/0169-8095(89)90020-3)

30. Clough S.A., Shephard M.W., Mlawer E.J., Delamere J.S., Iacono M.J., Cady-Pereira K., Boukabara S., and Brown P.D., “Atmospheric radiative transfer modeling: A summary of the AER codes”, *Journal of Quantitative Spectroscopy and Radiative Transfer*, **91** (2), pp. 233–244, 2005. doi: <https://doi.org/10.1016/j.jqsrt.2004.05.058>

31. Coakley J., and Yang P., *Atmospheric Radiation: A Primer with Illustrative Solutions*, Wiley Series in Atmospheric Radiation and Remote Sensing (Ed. A. Kokhanovsky), 2014.
link: N/A.

32. Coddington O. M., Richard E. C., Harber D., Pilewskie P., Woods T. N., Chance K., Liu X., and Sun K., “The TSIS-1 Hybrid Solar Reference Spectrum”, *Geophysical Research Letters*, **48**, e2020GL091709, 2023. doi: <https://doi.org/10.1029/2020GL091709>

33. Collange S., Daumas M., and Defour D., “Line-by-line spectroscopic simulations on graphics processing units”, *Computer Physics Communications*, **178** (2), pp. 135–143, 2008.
doi: <https://doi.org/10.1016/j.cpc.2007.08.013>

34. Cornette W.M., Acharya P.K., and Anderson G.P., “Using the MOSART code for atmospheric correction”, *Proceedings of IGARSS '94 - 1994 IEEE International Geoscience and Remote Sensing Symposium*, pp. 215–219, 1994.
doi: <https://doi.org/10.1109/IGARSS.1994.399084>

35. De Biévre P., Gallet M., Holden N. E., and Barnes I. L., “Isotopic abundances and atomic weights of the elements”, *Journal of Physical and Chemical Reference Data*, **13**, pp. 809 - 891, 1984. doi: <https://doi.org/10.1063/1.555720>

36. Delahaye T. and Coauthors, "The 2020 edition of the GEISA spectroscopic database", *Journal of Molecular Spectroscopy*, **380**, 111510, 2021.
doi: <https://doi.org/10.1016/j.jms.2021.111510>

37. Dicke R.H., "The effect of collisions upon the Doppler width of spectral lines", *Physical Review*, **89** (2), pp.472-473, 1953. doi: <https://link.aps.org/doi/10.1103/PhysRev.89.472>

38. Diner D. J. and Coauthors, "The Airborne Multiangle SpectroPolarimetric Imager (AirMSPI): a new tool for aerosol and cloud remote sensing", *Atmospheric Measurement Techniques*, **6**, pp. 2007–2025, 2013. doi: <https://doi.org/10.5194/amt-6-2007-2013>

39. Docter N., Preusker R., Filipitsch F., Kritten L., Schmidt F., and Fischer, J., "Aerosol optical depth retrieval from the EarthCARE Multi-Spectral Imager: the M-AOT product", *Atmospheric Measurement Techniques*, **16**, pp. 3437–3457, 2023.
doi: <https://doi.org/10.5194/amt-16-3437-2023>

40. Domysławska J., Wójtewicz S., Masłowski P., Cygan A., Bielska K., Trawiński R.S., Ciuryło R., and Lisak D., "A new approach to spectral line shapes of the weak oxygen transitions for atmospheric applications", *Journal of Quantitative Spectroscopy and Radiative Transfer*, **169**, pp.111-121, 2016. doi: <https://doi.org/10.1016/j.jqsrt.2015.10.019>

41. Dudhia A., "The Reference Forward Model (RFM)," *Journal of Quantitative Spectroscopy and Radiative Transfer*, **186**, pp. 243–253, 2017.
doi: <https://doi.org/10.1016/j.jqsrt.2016.06.018>

42. Dubey A., "Good Practices for High-Quality Scientific Computing", *Computing in Science & Engineering*, **24** (6), pp. 72-76, 2022.
doi: <https://doi.ieeecomputersociety.org/10.1109/MCSE.2023.3259259>

43. Easterbrook S.M. and Johns T.C., "Engineering the Software for Understanding Climate Change", *Computing in Science & Engineering*, **11** (6), pp. 65-74, 2009.
doi: <https://doi.org/10.1109/MCSE.2009.193>

44. Edwards D.P., "GENLN2: A General Line-by-line Atmospheric Transmittance and Radiance Model. Version 3.0 Description and Users Guide", University Corporation for Atmospheric Research (UCAR) Technical Report, No. NCAR/TN-367+STR, 1992.
doi: <http://dx.doi.org/10.5065/D6W37T86>

45. Efremenko D., and Kokhanovsky A., *Foundations of Atmospheric Remote Sensing*, Springer, 2021. doi: <https://doi.org/10.1007/978-3-030-66745-0>

46. Elsasser W.M., *Heat transfer by infrared radiation in the atmosphere*, Harvard University Press, Cambridge, 108 pp., 1942. link: <https://archive.org/details/ElsasserFull1942>

47. Emde C. and Coauthors, "The libRadtran software package for radiative transfer calculations (version 2.0.1)", *Geoscientific Model Development*, **9** (5), pp. 1647-1672, 2016.
doi: <https://doi.org/10.5194/gmd-9-1647-2016>

48. Fels S.B., "Simple strategies for inclusion of Voigt effects in infrared cooling rate calculations", *Applied Optics*, **18** (15), pp. 2634 - 2637, 1979.
doi: <https://doi.org/10.1364/AO.18.002634>

49. Foote E., “Circumstances Affecting the Heat of the Sun’s Rays”, *American Journal of Art and Science*, 22 (66), pp. 383–384, 1856.
link: https://en.wikipedia.org/wiki/Eunice_Foote (see Section “Scientific Career”)

50. Galatry L., “Simultaneous Effect of Doppler and Foreign Gas Broadening on Spectral Lines”, *Physical Review*, 122 (4), pp. 1218–1223, 1961.
doi: <https://doi.org/10.1103/PhysRev.122.1218>

51. Gamache R.R. and Coauthors, “Total internal partition sums for 166 isotopologues of 51 molecules important in planetary atmospheres: Application to HITRAN2016 and beyond,” *Journal of Quantitative Spectroscopy and Radiative Transfer*, 203, pp. 70–87, 2017.
doi: <https://doi.org/10.1016/j.jqsrt.2017.03.045>

52. Gamache R.R., Vispoel B., Rey M., Nikitin A., Tyuterev V., Egorov O., Gordon I.E., and Boudon V., “Total internal partition sums for the HITRAN2020 database”, *Journal of Quantitative Spectroscopy and Radiative Transfer*, 271, 107713, 2021.
doi: <https://doi.org/10.1016/j.jqsrt.2021.107713>

53. Gao B.-C., Heidebrecht K.B., and Goetz A.F.H., “Derivation of scaled surface reflectances from AVIRIS data”, *Remote Sensing of Environment*, 44 (2-3), pp. 165–178, 1993.
doi: [https://doi.org/10.1016/0034-4257\(93\)90014-O](https://doi.org/10.1016/0034-4257(93)90014-O)

54. Goldenstein C.S., Miller V.A., Spearrin R.M., and Strand C.L., “SpectraPlot.com: Integrated spectroscopic modeling of atomic and molecular gases,” *Journal of Quantitative Spectroscopy and Radiative Transfer*, 200, pp. 249–257, 2017.
doi: <https://doi.org/10.1016/j.jqsrt.2017.06.007>

55. Goody R.M., and Yung Y.L., *Atmospheric Radiation. Theoretical Basis*. Oxford University Press, 2nd Edition, 1989. link: N/A.

56. Gordley L.L., Marshall B.T., and Chu D.A., “Linepak: Algorithms for modeling spectral transmittance and radiance”, *Journal of Quantitative Spectroscopy and Radiative Transfer*, 52 (5), pp. 563–580, 1994. doi: [https://doi.org/10.1016/0022-4073\(94\)90025-6](https://doi.org/10.1016/0022-4073(94)90025-6)

57. Gordon H. R., *Physical Principles of Ocean Color Remote Sensing*, University of Miami, 2019. doi: <https://doi.org/10.33596/ppoers-19>

58. Gordon I.E., Rothman L.S., and Toon G. C., “Revision of spectral parameters for the B- and γ -bands of oxygen and their validation against atmospheric spectra”, *Journal of Quantitative Spectroscopy and Radiative Transfer*, 112 (14), pp. 2310–2322, 2011, doi: 10.1016/j.jqsrt.2011.05.007.

59. Gordon I.E., Potterbusch M.R., Bouquin D., Erdmann C.C., Wilzewski J.S., and Rothman L. S., “Are your spectroscopic data being used?”, *Journal of Molecular Spectroscopy*, 327, pp. 232–238, 2016. doi: <https://doi.org/10.1016/j.jms.2016.03.011>

60. Gordon I.E. and Coauthors, “The HITRAN2016 molecular spectroscopic database,” *Journal of Quantitative Spectroscopy and Radiative Transfer*, 203, pp. 3–69, 2017.
doi: <https://doi.org/10.1016/j.jqsrt.2017.06.038>

61. Gottschling P., *Discovering Modern C++: An Intensive Course for Scientists, Engineers, and Programmers*, 2nd Edition, Addison-Wesley Professional, 576 pp. 2021. link: N/A.

62. Greenblatt G. D., Orlando J. J., Burkholder J. B., and Ravishankara A. R., “Absorption measurements of oxygen between 330 and 1140 nm”, *Journal of Geophysical Research*, 95(D11), pp.18577 – 18582, 1990. doi: <https://doi.org/10.1029/JD095iD11p18577>

63. Gueymard C.A., “Parameterized transmittance model for direct beam and circumsolar spectral irradiance”, *Solar Energy*, 71 (5), pp. 325 – 346, 2001. doi: [https://doi.org/10.1016/S0038-092X\(01\)00054-8](https://doi.org/10.1016/S0038-092X(01)00054-8)

64. Havemann S., Thelen J.C., Taylor J.P., and Harlow R.C., “The Havemann-Taylor Fast Radiative Transfer Code (HT-FRTC): A multipurpose code based on principal components”, *Journal of Quantitative Spectroscopy and Radiative Transfer*, 220, pp. 180–192, 2018. doi: <https://doi.org/10.1016/j.jqsrt.2018.09.008>

65. He W., Wu K., Feng Y., Fu D., Chen Z., and Li F., “The Radiative Transfer Characteristics of the O₂ Infrared Atmospheric Band in Limb-Viewing Geometry”, *Remote Sensing*, 11(22): 2702, 2019. doi: <https://doi.org/10.3390/rs11222702>

66. Hearn A.G., “The Absorption of Ozone in the Ultra-violet and Visible Regions of the Spectrum”, *Proceedings of the Physical Society*, 78 (5), pp. 932-940, 1961. link: <https://iopscience.iop.org/article/10.1088/0370-1328/78/5/340>

67. Heaton D. and Carver J.C., “Claims about the use of software engineering practices in science: A systematic literature review”, *Information and Software Technology*, 67, pp. 207-219, 2015. doi: <https://doi.org/10.1016/j.infsof.2015.07.011>

68. Hinsen K., "Dealing With Software Collapse", *Computing in Science & Engineering*, 21 (3), pp.104-108, 2019. doi: <https://doi.org/10.1109/MCSE.2019.2900945>

69. Hollis M.D.J., Tessenyi M., and Tinetti G., “Tau: A 1D radiative transfer code for transmission spectroscopy of extrasolar planet atmospheres”, *Computer Physics Communications*, 184 (10), pp. 2351–2361, 2013. doi: <https://doi.org/10.1016/j.cpc.2013.05.011>

70. Hollis M.D.J., Tessenyi M., and Tinetti G., “TAU: A 1D radiative transfer code for transmission spectroscopy of extrasolar planet atmospheres”, *Computer Physics Communications*, 185 (2), p. 695, 2014. doi: <https://doi.org/10.1016/j.cpc.2013.05.011>

71. Hill C., Gordon I.E., Rothman L.S., and Tennyson J., “A new relational database structure and online interface for the HITRAN database”, *Journal of Quantitative Spectroscopy and Radiative Transfer*, 130, pp. 51–61, 2013. doi: <https://doi.org/10.1016/j.jqsrt.2013.04.027>

72. Hill C., Gordon I.E., Kochanov R.V., Barrett L., Wilzewski J.S., and Rothman L.S., “HITRANonline: An online interface and the flexible representation of spectroscopic data in the HITRAN database,” *Journal of Quantitative Spectroscopy and Radiative Transfer*, 177, pp. 4-14, 2016. doi: <https://doi.org/10.1016/j.jqsrt.2015.12.012>

73. Humlíček J., “Optimized computation of the Voigt and complex probability functions,” *Journal of Quantitative Spectroscopy and Radiative Transfer*, 27 (4), pp. 437-444, 1982. doi: [https://doi.org/10.1016/0022-4073\(82\)90078-4](https://doi.org/10.1016/0022-4073(82)90078-4)

74. Ibrahim A., Franz B., Ahmad Z., Healy R., Knobelispiesse K., Gao B-C, Proctor C, and Zhai P.-W., “Atmospheric correction for hyperspectral ocean color retrieval with application to the

Hyperspectral Imager for the Coastal Ocean (HICO)", *Remote Sensing of Environment*, **204**, pp.60-75, 2018. doi: <https://doi.org/10.1016/j.rse.2017.10.041>

75. Iwabuchi H. and Okamura R., "Multispectral Monte Carlo radiative transfer simulation by the maximum cross-section method", *Journal of Quantitative Spectroscopy and Radiative Transfer*, **193**, pp. 40-46, 2017. doi: <https://doi.org/10.1016/j.jqsrt.2017.01.025>

76. Kanewala U. and Bieman J.M., "Testing scientific software: A systematic literature review", *Information and Software Technology*, **56** (10), pp. 1219-1232, 2014. doi: <https://doi.org/10.1016/j.infsof.2014.05.006>

77. Kendall R., Fisher D., Henderson D., Carver J., Mark A., Post D., Rhoades Jr. C.E., and Squires S., "Development of a Weather Forecasting Code: A Case Study", *IEEE Software*, **25** (4), pp. 59-65, 2008. doi: <https://doi.org/10.1109/MS.2008.86>

78. Karlovets E.V., Mondelain D., Tashkun S.A., and Campargue A., "The absorption spectrum of nitrous oxide between 7250 and 7653 cm⁻¹", *Journal of Quantitative Spectroscopy and Radiative Transfer*, **301**, 108511, 2023. doi: <https://doi.org/10.1016/j.jqsrt.2023.108511>

79. Karman T., Koenis M. A. J., Banerjee A., Parker D. H., Gordon I. E., van der Avoird A., van der Zande W. J., and Groenenboom G. C., "O₂-O₂ and O₂-N₂ collision-induced absorption mechanisms unravelled", *Nature Chemistry*, **10** (5), pp. 549-554, 2018. doi: <https://doi.org/10.1038/s41557-018-0015-x>

80. Karman T., and Coauthors, "Update of the HITRAN collision-induced absorption section", *Icarus*, **328**, pp.160-175, 2019. doi: <https://doi.org/10.1016/j.icarus.2019.02.034>

81. Key J.R. and Schweiger A.J., "Tools for atmospheric radiative transfer: STREAMER and FLUXNET", *Computers & Geosciences*, **24** (5), pp. 443-451, 1998. doi: [https://doi.org/10.1016/S0098-3004\(97\)00130-1](https://doi.org/10.1016/S0098-3004(97)00130-1)

82. Kistenev Yu.V., Skiba V.E., Prischepa V.V., Vrazhnov D.A., and Borisov A.V., "Super-resolution reconstruction of noisy gas-mixture absorption spectra using deep learning", *Journal of Quantitative Spectroscopy and Radiative Transfer*, 289: 108278, 2022. doi: <https://doi.org/10.1016/j.jqsrt.2022.108278>

83. Kneizys F.X., Shettle E.P., Abreu L.W., Chetwynd J.H., Anderson G.P., Gallery W.O., Selby J.E.A., and Clough S.A., "Users Guide to LOWTRAN 7", Hanscom AFB, MA: Air Force Geophysics Laboratory, 1988. link: <https://apps.dtic.mil/sti/citations/ADA206773>

84. Kneizys F. X. and Coauthors, *The MODTRAN 2/3 Report and LOWTRAN 7 Model*, North Andover, MA, 1996. link: <https://web.gps.caltech.edu/~vijay/pdf/modrept.pdf>

85. Kochanov R.V., Gordon I.E., Rothman L.S., Wcisło P., Hill C., and Wilzewski J.S., "HITRAN Application Programming Interface (HAPI): A comprehensive approach to working with spectroscopic data", *Journal of Quantitative Spectroscopy and Radiative Transfer*, **177**, pp. 15-30, 2016. doi: <https://doi.org/10.1016/j.jqsrt.2016.03.005>

86. Kochanov R. V., and Coauthors, "Infrared absorption cross-sections in HITRAN2016 and beyond: Expansion for climate, environment, and atmospheric applications", *Journal of Quantitative Spectroscopy and Radiative Transfer*, **230**, pp. 172-221, 2019. doi: <https://doi.org/10.1016/j.jqsrt.2019.04.001>

87. Korkin S., Sayer A.M., Ibrahim A., and Lyapustin A., “A practical guide to writing a radiative transfer code”, *Computer Physics Communications*, **271**, 108198, 2022. doi: <https://doi.org/10.1016/j.cpc.2021.108198>

88. Kuntz M., “A new implementation of the Humlíček algorithm for the calculation of the Voigt profile function”, *Journal of Quantitative Spectroscopy and Radiative Transfer*, **57** (60), pp. 819-824, 1997. doi: [https://doi.org/10.1016/S0022-4073\(96\)00162-8](https://doi.org/10.1016/S0022-4073(96)00162-8)

89. Kurucz R.L., “Synthetic infrared spectra”, *Infrared Solar Physics*, IAU Symp. **154**, edited by D.M. Rabin and J.T. Jefferies, Kluwer, Acad., Norwell Massachusetts, pp. 523-531, 1992. link: <https://adsabs.harvard.edu/full/1994IAUS..154..523K>

90. Kurucz R.L., “The solar irradiance by computation”, (unpublished) 1997. link: <http://kurucz.harvard.edu/sun/irradiance/solarirr.tab>

91. Laraia A.L., Gamache R.R., Lamouroux J., Gordon I.E., and Rothman L.S., “Total internal partition sums to support planetary remote sensing”, *Icarus*, **215** (1), pp. 391-400, 2011. doi: <https://doi.org/10.1016/j.icarus.2011.06.004>

92. Laszlo I., Stamnes K., Wiscombe W., and Tsay S.-C., “The Discrete Ordinate Algorithm, DISORT for Radiative Transfer,” in *Light Scattering Reviews*, Springer., A. A. Kokhanovsky, Ed. Berlin, 2016, pp. 3–65. doi: https://doi.org/10.1007/978-3-662-49538-4_1

93. LeVeque R.J., Mitchell I.M., and Stodden V., "Reproducible research for scientific computing: Tools and strategies for changing the culture", *Computing in Science & Engineering*, **14** (4), pp. 13-17, 2012. doi: <https://doi.org/10.1109/MCSE.2012.38>

94. Liou K. N., *An Introduction to Atmospheric Radiation* (2nd Ed.), Academic Press, 2002. link: <https://shop.elsevier.com/books/an-introduction-to-atmospheric-radiation/liou/978-0-12-451451-5>

95. Liu X., Yang Q., Li H., Jin Z., Wu W., Kizer S., Zhou D.K., and Yang P., “Development of a fast and accurate PCRTM radiative transfer model in the solar spectral region”, *Applied Optics*, **55** (29), pp. 8236-8247, 2016. doi: <https://doi.org/10.1364/AO.55.008236>

96. Lyapustin A.I., “Interpolation and Profile Correction (IPC) Method for Shortwave Radiative Transfer in Spectral Intervals of Gaseous Absorption,” *Journal of the Atmospheric Sciences*, **60** (6), pp. 865–871, 2003. doi: [https://doi.org/10.1175/1520-0469\(2003\)060%3C0865:IAPCIM%3E2.0.CO;2](https://doi.org/10.1175/1520-0469(2003)060%3C0865:IAPCIM%3E2.0.CO;2)

97. Lyapustin A., Muldashev T., and Wang Y., “Code SHARM: fast and accurate radiative transfer over spatially variable anisotropic surfaces,” in *Light Scattering Reviews 5. Single light scattering and radiative transfer* (A. Kokhanovsky, Ed.), Chichester, UK: Springer, 2010, pp. 205–247. doi: https://doi.org/10.1007/978-3-642-10336-0_6

98. Luther F. M., Ellingson R. G., Fouquart Y., Fels S., Scott N. A., and Wiscombe W. J., “Intercomparison of Radiation Codes in Climate Models (ICRCCM): Longwave Clear-Sky Results – A Workshop Summary”, *Bulletin of the American Meteorological Society*, **69**, pp. 40 – 48, 1988. doi: <https://doi.org/10.1175/1520-0477-69.1.40>

99. McClatchey R.A., Benedict W.S., Clough S.A., Burch D.E., Calfee R.F., Fox K., Rothman L.S., and Garing J.S., “AFCRL Atmospheric Absorption Line Parameters Compilation”, Air

Force Cambridge Research Laboratories, Bedford MA, 1973.

link: https://modis-images.gsfc.nasa.gov/JavaHAWKS/AFCRL_AALPC.pdf

100. McLean A. B., Mitchell C. E. J., and Swanston D. M., “Implementation of an efficient analytical approximation to the Voigt function for photoemission lineshape analysis”, *Journal of Electron Spectroscopy and Related Phenomena*, **69** (2), pp. 125–132, 1994.
doi: [https://doi.org/10.1016/0368-2048\(94\)02189-7](https://doi.org/10.1016/0368-2048(94)02189-7)
101. Mlawer E.J., Taubman S.J., Brown P.D., Iacono M.J., and Clough S.A., “Radiative transfer for inhomogeneous atmospheres: RRTM, a validated correlated- k model for the longwave,” *Journal of Geophysical Research: Atmospheres*, **102** (D14), pp. 16663–16682, 1997.
doi: <https://doi.org/10.1029/97JD00237>
102. Mlawer E.J., Payne V.H., Moncet J.L., Delamere J.S., Alvarado M.J., and Tobin D.C., “Development and recent evaluation of the MT-CKD model of continuum absorption”, *Philosophical Transactions of the Royal Society A*, **370**, pp. 2520–2556, 2012.
doi: <https://doi.org/10.1098/rsta.2011.0295>
103. Mlawer E.J., Cady-Pereira K.E., Mascio J., and Gordon I.E., “The inclusion of the MT_CKD water vapor continuum model in the HITRAN molecular spectroscopic database”, *Journal of Quantitative Spectroscopy and Radiative Transfer*, **306**, 108645, 2023.
doi: <https://doi.org/10.1029/97JD00237>
104. Mobley C. D. (Editor), *The Oceanic Optics Book*, International Ocean Colour Coordinating Group (IOCCG), Dartmouth, NS, Canada, 924 pp., 2022.
doi: <http://dx.doi.org/10.25607/OBP-1710>
105. Mohankumar N. and Sen S., “On the very accurate evaluation of the Voigt functions,” *Journal of Quantitative Spectroscopy and Radiative Transfer*, **224**, pp. 192–196, 2019.
doi: <https://doi.org/10.1016/j.jqsrt.2018.11.022>
106. Müller H.S.P., Schlöder F., Stutzki J., and Winnewisser G., “The Cologne Database for Molecular Spectroscopy, CDMS: a useful tool for astronomers and spectroscopists”, *Journal of Molecular Structure*, **742** (1-3), pp. 215–227, 2005.
doi: <https://doi.org/10.1016/j.molstruc.2005.01.027>
107. Natraj V., Spurr R. J. D., Boesch H., Jiang Y., and Yung Y. L., “Evaluation of errors from neglecting polarization in the forward modeling of O₂ A band measurements from space, with relevance to CO₂ column retrieval from polarization-sensitive instruments”, *Journal of Quantitative Spectroscopy and Radiative Transfer*, **103** (2), pp. 245–259, 2007,
doi: 10.1016/j.jqsrt.2006.02.073.
108. Ngo N. H., Lisak D., Tran H., and Hartmann J. M., “An isolated line-shape model to go beyond the Voigt profile in spectroscopic databases and radiative transfer codes”, *Journal of Quantitative Spectroscopy and Radiative Transfer*, **129**, pp. 89–100, 2013.
doi: <https://doi.org/10.1016/j.jqsrt.2013.05.034>
109. Ngo N. H., Lisak D., Tran H., and Hartmann J. M., “Erratum to ‘An isolated line-shape model to go beyond the Voigt profile in spectroscopic databases and radiative transfer codes’ [J. Quant. Spectrosc. Radiat. Transf. 129 (2013) 89-100]”, *Journal of Quantitative Spectroscopy and Radiative Transfer*, **130**, pp. 1–2, 2014.
doi: <https://doi.org/10.1016/j.jqsrt.2013.09.014>

Spectroscopy and Radiative Transfer, **134**, p. 105, 2014.
doi: <http://dx.doi.org/10.1016/j.jqsrt.2013.10.016>

110. Nordebo S., “Uniform error bounds for fast calculation of approximate Voigt profiles” *Journal of Quantitative Spectroscopy and Radiative Transfer*, **270**, 107715, 2021.
doi: <https://doi.org/10.1016/j.jqsrt.2021.107715>
111. Nowlan C. R., McElroy C. T., and Drummond J. R., “Measurements of the O2A - and B-bands for determining temperature and pressure profiles from ACE-MAESTRO: Forward model and retrieval algorithm”, *Journal of Quantitative Spectroscopy and Radiative Transfer*, **108** (3), pp. 371–388, 2007. doi: <https://doi.org/10.1016/j.jqsrt.2007.06.006>
112. Oliveira S., and Stewart D., *Writing Scientific Software: A Guide to Good Style*, Cambridge University Press, New York, 303 pp., 2006.
113. Orphal J., and Coauthors, “Absorption cross-sections of ozone in the ultraviolet and visible spectral regions: Status report 2015”, *Journal of Molecular Spectroscopy*, **327**, pp. 105-121, 2016. doi: <http://dx.doi.org/10.1016/j.jms.2016.07.007>
114. Pannier E. and Laux C.O., “RADIS: A nonequilibrium line-by-line radiative code for CO2 and HITRAN-like database species”, *Journal of Quantitative Spectroscopy and Radiative Transfer*, **222–223**, pp. 12–25, 2019.
doi: <https://doi.org/10.1016/j.jqsrt.2018.09.027>
115. Payne V.H. and Coauthors, “Absorption coefficient (ABSCO) tables for the Orbiting Carbon Observatories: Version 5.1”, *Journal of Quantitative Spectroscopy and Radiative Transfer*, **255**, 2020. doi: <https://doi.org/10.1016/j.jqsrt.2020.107217>
116. Petty G. W., *A First Course in Atmospheric Radiation* (2nd ed.), Sundog Publishing, Madison, Wisconsin, 2006. Link: N/A.
117. Pfeilsticker K., Erle F., Funk O., Veitel H., and Platt U., “First geometrical pathlengths probability density function derivation of the skylight from spectroscopically highly resolving oxygen A-band observations: 1. Measurement technique, atmospheric observations and model calculations”, *Journal of Geophysical Research: Atmospheres*, **103** (D10), pp. 11483–11504, 1998. doi: <https://doi.org/10.1029/98JD00725>
118. Pickett H.M., Poynter R.L., Cohen E.A., Delitsky M.L., Pearson J.C., and Muller H.S.P., “Submillimeter, millimeter, and microwave spectral line catalog”, *Journal of Quantitative Spectroscopy and Radiative Transfer*, **60** (5), pp. 883–890, 1998.
doi: [https://doi.org/10.1016/S0022-4073\(98\)00091-0](https://doi.org/10.1016/S0022-4073(98)00091-0)
119. Pincus R. and Coauthors, “Benchmark calculations of radiative forcing by greenhouse gases”, *Journal of Geophysical Research*, **125**: e2020JD033483, 2020.
doi: <https://doi.org/10.1029/2020JD033483>
120. Pipitone J. and Easterbrook S., “Assessing climate model software quality: a defect density analysis of three models”, *Geoscientific Model Development*, **5**, 1009–1022, 2012.
doi: <https://doi.org/10.5194/gmd-5-1009-2012>
121. Pliutau D. and Roslyakov K., “Bytran - |- spectral calculations for portable devices using the HITRAN database”, *Earth Science Informatics*, **10**, pp. 395–404, 2017.
doi: <https://doi.org/10.1007/s12145-017-0288-4>

122. Pouillet C., “Memoir on the solar heat, on the radiating and absorbing powers of atmospheric air, and on the temperature of space”, in *Scientific Memoirs, Selected from the Transactions of Foreign Academies of Science and Learned Societies, and from Foreign Journals* (Taylor R., Editor), London, England: Richard and John E. Taylor, pp.44-90, 1846. link: https://en.wikipedia.org/wiki/Claude_Pouillet (see Ref. 6: English translation for pdf)

123. Predoi-Cross A., Hambrook K., Keller R., Povey C., Schofield I., HurtmansD., Over H., and Mellau G. Ch., “Spectroscopic lineshape study of the self-perturbed oxygen A-band”, *Journal of Molecular Spectroscopy*, **248** (2), pp. 85–110, 2008. doi: <https://doi.org/10.1016/j.jms.2007.11.007>

124. Press W.H., Teukolsky S.A., Vettering W.T., and Flannery B.P., *Numerical Recipes in C: the Art of Scientific Computing*, Cambridge University Press, New York, 1992. link: <https://numerical.recipes/>

125. Press W.H., Teukolsky S.A., Vettering W.T., and Flannery B.P., *Numerical Recipes. The Art of Scientific Computing*, Cambridge University Press, New York, 2007. link: <https://numerical.recipes/>

126. Prischepa V.V., Skiba V.E., Vrazhnov D.A., Kistenev Yu. V., “Gas mixtures IR absorption spectra decomposition using a deep neural network”, *Journal of Quantitative Spectroscopy and Radiative Transfer*, **301**: 108521, 2023. doi: <https://doi.org/10.1016/j.jqsrt.2023.108521>

127. Puthukkudy A., Martins J. V., Remer L. A., Xu X., Dubovik O., Litvinov P., McBride B., Burton S., and Barbosa H. M. J., “Retrieval of aerosol properties from Airborne Hyper-Angular Rainbow Polarimeter (AirHARP) observations during ACEPOL 2017”, *Atmospheric Measurement Techniques*, **13**, 5207–5236, 2020. doi: <https://doi.org/10.5194/amt-13-5207-2020>

128. Rautian S. G., and Sobel'man I. I., “The effect of collisions on the Doppler broadening of spectral lines”, *Soviet Physics Uspekhi*, **9** (5), pp.701-716, 1967. doi: <https://dx.doi.org/10.1070/PU1967v009n05ABEH003212>

129. Richard C., and Coauthors, “New section of the HITRAN database: Collision-induced absorption (CIA)”, *Journal of Quantitative Spectroscopy and Radiative Transfer*, **113** (11), pp. 1276-1285, 2012. doi: <https://doi.org/10.1016/j.jqsrt.2011.11.004>

130. Rothman L.S., “Update of the AFGL atmospheric absorption line parameters compilation”, *Applied Optics*, **17** (22), pp. 3517–3518, 1978. doi: <https://doi.org/10.1364/AO.17.003517>

131. Rothman L.S. and Coauthors, “The HITRAN database: 1986 edition”, *Applied Optics*, **26** (19), pp. 4058–4097, 1987. doi: <https://doi.org/10.1364/AO.26.004058>

132. Rothman L.S. and Coauthors, “The HITRAN molecular spectroscopic database and HAWKS (HITRAN atmospheric workstation): 1996 edition”, *Journal of Quantitative Spectroscopy and Radiative Transfer*, **60** (5), pp. 665-710, 1998. doi: [https://doi.org/10.1016/S0022-4073\(98\)00078-8](https://doi.org/10.1016/S0022-4073(98)00078-8)

133. Rothman L.S. and Coauthors, “The HITRAN molecular spectroscopic database: edition of 2000 including updates through 2001”, *Journal of Quantitative Spectroscopy and*

Radiative Transfer, **82** (1-4), pp. 5–44, 2003.
doi: [https://doi.org/10.1016/S0022-4073\(03\)00146-8](https://doi.org/10.1016/S0022-4073(03)00146-8)

134. Rothman L.S. and Coauthors, “The HITRAN 2004 molecular spectroscopic database”, *Journal of Quantitative Spectroscopy and Radiative Transfer*, **96** (2), pp. 139–204, 2005.
doi: <https://doi.org/10.1016/j.jqsrt.2004.10.008>

135. Rothman L.S., Jacquinet-Husson N., Boulet C., and Perrin A. M., “History and future of the molecular spectroscopic databases”, *Comptes Rendus Physique*, **6**(8), pp.897-907, 2005.
doi: <https://doi.org/10.1016/j.crhy.2005.09.001>

136. Rothman L.S. and Coauthors, “The HITRAN 2008 molecular spectroscopic database,” *Journal of Quantitative Spectroscopy and Radiative Transfer*, **110** (9–10), pp. 533–572, 2009. doi: <https://doi.org/10.1016/j.jqsrt.2009.02.013>

137. Rothman L.S., “The evolution and impact of the HITRAN molecular spectroscopic database”, *Journal of Quantitative Spectroscopy and Radiative Transfer*, **111** (11), pp. 1565–1567, 2010. doi: <https://doi.org/10.1016/j.jqsrt.2010.01.027>

138. Rothman L.S., and Coauthors, “The HITRAN2012 molecular spectroscopic database”, *Journal of Quantitative Spectroscopy and Radiative Transfer*, **130**, pp. 4-50. doi: <http://dx.doi.org/10.1016/j.jqsrt.2013.07.002>

139. Rothman L.S., “History of the HITRAN Database”, *Nature Reviews Physics*, **3** (5), pp. 302–304, 2021. doi: <https://doi.org/10.1038/s42254-021-00309-2>

140. Rozanov V.V., Rozanov A.V., Kokhanovsky A.A., and Burrows J.P., “Radiative transfer through terrestrial atmosphere and ocean : Software package SCIATRAN,” *Journal of Quantitative Spectroscopy and Radiative Transfer*, **133**, pp. 13–71, 2014
doi: <https://doi.org/10.1016/j.jqsrt.2013.07.004>

141. Ruyten W., “Comment on ‘A new implementation of the Humlíček algorithm for the calculation of the Voigt profile function’ by M. Kuntz [JQSRT 57(6) (1997) 819–824]”, *Journal of Quantitative Spectroscopy and Radiative Transfer*, **86** (2), pp. 231-233, 2004.
doi: <https://doi.org/10.1016/j.jqsrt.2003.12.027>

142. Sanders R. and Kelly D., "Dealing with Risk in Scientific Software Development", *IEEE Software*, **25** (4), pp. 21-28, 2008. doi: <https://doi.org/10.1109/MS.2008.84>

143. Sayer A.M., Lelli L., Cairns B., van Diedenhoven B., Ibrahim A., Knobelspiesse K.D., Korkin S., and Werdell P.J., “The CHROMA cloud-top pressure retrieval algorithm for the Plankton, Aerosol, Cloud, ocean Ecosystem (PACE) satellite mission”, *Atmospheric Measurement Techniques*, **16** (4), pp.969-996, 2023.
doi: <https://doi.org/10.5194/amt-16-969-2023>

144. Saunders R., Matricardi M., and Brunel P., “An improved fast radiative transfer model for assimilation of satellite radiance observations”, *Quarterly Journal of Royal Meteorological Society*, **125** (556), pp. 1407-1425, 1999.
doi: <https://doi.org/10.1002/qj.1999.49712555615>

145. Segal J. and Morris C., "Developing Scientific Software", *IEEE Software*, **25** (4), pp. 18-20, 2008. doi: <https://doi.ieeecomputersociety.org/10.1109/MS.2008.85>

146. Schreier F., “The Voigt and complex error function: A comparison of computational methods”, *Journal of Quantitative Spectroscopy and Radiative Transfer*, **48** (5), pp. 743–762, 1992. doi: [https://doi.org/10.1016/0022-4073\(92\)90139-U](https://doi.org/10.1016/0022-4073(92)90139-U)

147. Schreier F. and Schimpf B., “A New Efficient Line-By-Line Code for High Resolution Atmospheric Radiation Computations incl. Derivatives”, IRS 2000: Current Problems in Atmospheric Radiation, A. Deepak Publishing, pp.381-385, 2001.
link: <https://www.gbv.de/dms/goettingen/333853989.pdf>

148. Schreier F. and Böttger U., “MIRART, a line-by-line code for infrared atmospheric radiation computations incl. derivatives”, *Atmospheric and Oceanic Optics*, **16** (3), pp. 262–268, 2003. link: <https://ao.iao.ru/en/content/vol.16-2003/iss.03>

149. Schreier F., Gimeno García S., Hedelt P., Hess M., Mendrok J., Vasquez M., and Xu J., “GARLIC - A general purpose atmospheric radiative transfer line-by-line infrared-microwave code: Implementation and evaluation”, *Journal of Quantitative Spectroscopy and Radiative Transfer*, **137**, pp. 29–50, 2014. doi: <https://doi.org/10.1016/j.jqsrt.2013.11.018>

150. Schreier F., “Computational aspects of speed-dependent Voigt profiles”, *Journal of Quantitative Spectroscopy and Radiative Transfer*, **187**, pp. 44–53, 2017.
doi: <https://doi.org/10.1016/j.jqsrt.2016.08.009>

151. Schreier F., “The Voigt and complex error function: Humlíček’s rational approximation generalized”, *Monthly Notices of the Royal Astronomical Society*, **479** (3), pp. 3068–3075, 2018(a). doi: <https://doi.org/10.1093/mnras/sty1680>

152. Schreier F., “Comments on the Voigt function implementation in the Astropy and SpectraPlot.com packages”, *Journal of Quantitative Spectroscopy and Radiative Transfer*, **213**, pp. 13–16, 2018(b). doi: <https://doi.org/10.1016/j.jqsrt.2018.03.019>

153. Schreier F., Gimeno García S., Hochstafpl P., and Städlt S., “Py4CAtS—PYthon for Computational ATmospheric Spectroscopy”, *Atmosphere*, **10** (5), 262, 2019.
doi: <https://doi.org/10.3390/atmos10050262>

154. Schreier F. and Hochstafpl P., “Computational aspects of speed-dependent Voigt and Rautian profiles”, *Journal of Quantitative Spectroscopy and Radiative Transfer*, **258**, 107385, 2021. doi: <https://doi.org/10.1016/j.jqsrt.2020.107385>

155. Scott N.A. and Chedin A., “A Fast Line-by-Line Method for Atmospheric Absorption Computations: The Automatized Atmospheric Absorption Atlas”, *Journal of Applied Meteorology and Climatology*, 20 (7), pp. 802–812, 1981.
doi: [https://doi.org/10.1175/1520-0450\(1981\)020%3C0802:AFLBLM%3E2.0.CO;2](https://doi.org/10.1175/1520-0450(1981)020%3C0802:AFLBLM%3E2.0.CO;2)

156. Shine K. P., Ptashnik I.V., and Rädel G., “The water vapour continuum: brief history and recent developments”, *Surveys in Geophysics*, **33**, pp. 535 – 555, 2012.
doi: <https://doi.org/10.1007/s10712-011-9170-y>

157. Smette A. and Coauthors, “Molecfit: A general tool for telluric absorption correction”, *Astronomy & Astrophysics*, **576**, A77, 2015.
doi: <https://doi.org/10.1051/0004-6361/201423932>

158. Spänkuch D., "Effects of line shapes and line coupling on the atmospheric transmittance," *Atmospheric Research*, **23**(3), pp. 323–344, 1989.
doi: [https://doi.org/10.1016/0169-8095\(89\)90024-0](https://doi.org/10.1016/0169-8095(89)90024-0)

159. Stam D. M., de Haan J. F., Hovenier J. W., and Stammes P., "A fast method for simulating observations of polarized light emerging from the atmosphere applied to the oxygen-A band", *Journal of Quantitative Spectroscopy and Radiative Transfer*, **64** (2), pp. 131–149, 2000. doi: [https://doi.org/10.1016/S0022-4073\(99\)00009-6](https://doi.org/10.1016/S0022-4073(99)00009-6)

160. Stammes K., Tsay S.-C., Wiscombe W., and Jayaweera K., "Numerically stable algorithm for discrete-ordinate-method radiative transfer in multiple scattering and emitting layered media", *Applied Optics*, **27** (12), pp. 2502–2509, 1988.
doi: <https://doi.org/10.1364/AO.27.002502>

161. Stammes K., Thomas G. E., and Stammes J. J., *Radiative Transfer in the Atmosphere and Ocean* (2nd Ed.), Cambridge University Press, 2017.
doi: <https://doi.org/10.1017/9781316148549>

162. Stiller G.P., von Clarmann T., Funke B., Glatthor N., Hase F., Höpfner M., and Linden A., "Sensitivity of trace gas abundances retrievals from infrared limb emission spectra to simplifying approximations in radiative transfer modelling", *Journal of Quantitative Spectroscopy and Radiative Transfer*, **72** (3), pp. 249–280, 2001.
doi: [https://doi.org/10.1016/S0022-4073\(01\)00123-6](https://doi.org/10.1016/S0022-4073(01)00123-6)

163. Storer T., "Bridging the Chasm: A Survey of Software Engineering Practice in Scientific Programming", *ACM Computing Surveys*, **50**(4), 47, pp.1-32, 2017.
doi: <https://doi.org/10.1145/3084225>

164. Tennyson J. and Coauthors, "Recommended isolated-line profile for representing high-resolution spectroscopic transitions (IUPAC technical report)", *Pure and Applied Chemistry*, **86** (12), pp. 1931–1943, 2014. doi: <https://doi.org/10.1515/pac-2014-0208>

165. Thompson D.R., Gao B.-C., Green R.O., Roberts D.A., Dennison P.E., and Lundein S.R., "Atmospheric correction for global mapping spectroscopy: ATREM advances for the HyspIRI preparatory campaign", *Remote Sensing of Environment*, **167**, pp. 64–77, 2015.
doi: <https://doi.org/10.1016/j.rse.2015.02.010>

166. Thorpe A. K., Roberts D.A., Bradley E.S., Funk C.C., Dennison P.E., and Leifer I., "High resolution mapping of methane emissions from marine and terrestrial sources using a Cluster-Tuned Matched Filter technique and imaging spectrometry", *Remote Sensing of Environment*, **134**, pp. 305-318, 2013. doi: <https://doi.org/10.1016/j.rse.2013.03.018>

167. Tonkov M. V., Filippov N. N., Timofeyev Yu. M., and Polyakov A.V., "A simple model of the line mixing effect for atmospheric applications: Theoretical background and comparison with experimental profiles", *Journal of Quantitative Spectroscopy and Radiative Transfer*, **56** (5), pp.783-795, 1996. doi: [https://doi.org/10.1016/S0022-4073\(96\)00113-6](https://doi.org/10.1016/S0022-4073(96)00113-6)

168. Tran H., Boulet C., and Hartmann J.-M., "Line mixing and collision-induced absorption by oxygen in the A band: Laboratory measurements, model, and tools for atmospheric spectra computations", *Journal of Geophysical Research*, **111**, D15210, 2006.
doi: <https://doi.org/10.1029/2005JD006869>

169. Tran H. and Hartmann J.-M., “An improved O₂ A band absorption model and its consequences for retrievals of photon paths and surface pressures”, *Journal of Geophysical Research*, **113**, D18104, 2008. doi: <https://doi.org/10.1029/2008JD010011>

170. Tran H., Ngo N.H., and Hartmann J.-M., “Efficient computation of some speed-dependent isolated line profiles”, *Journal of Quantitative Spectroscopy and Radiative Transfer*, **129**, pp. 199–203, 2013, doi: <https://doi.org/10.1016/j.jqsrt.2013.06.015>

171. Tran H., Ngo N.H., Hartmann J.-M., “Erratum to “Efficient computation of some speed-dependent isolated line profiles” [J. Quant. Spectrosc. Radiat. Transfer 129 (2013) 199–203]”, *Journal of Quantitative Spectroscopy and Radiative Transfer*, **134**, p.104, 2014. doi: <https://doi.org/10.1016/j.jqsrt.2013.10.015>

172. Turner E., Rayer P., and Saunders R., “AMSUTRAN: A microwave transmittance code for satellite remote sensing”, *Journal of Quantitative Spectroscopy and Radiative Transfer*, **227**, pp. 117–129, 2019. doi: <https://doi.org/10.1016/j.jqsrt.2019.02.013>

173. Tyndall J., “Note on the transmission of radiant heat through gaseous bodies”, *Proceedings of the Royal Society of London*, **10**, pp. 37-39, 1860. doi: <https://doi.org/10.1098/rspl.1859.0017>

174. Urban J., Baron P., Lautié N., Schneider N., Dassas K., Ricaud P., and De La Noë J., “Moliere (v5): A versatile forward- and inversion model for the millimeter and sub-millimeter wavelength range,” *Journal of Quantitative Spectroscopy and Radiative Transfer*, **83** (3–4), pp. 529–554, 2004. doi: [https://doi.org/10.1016/S0022-4073\(03\)00104-3](https://doi.org/10.1016/S0022-4073(03)00104-3)

175. van de Hulst H.C. and Reesinck J. J. M., “Line Breadths and Voigt Profiles”, *The Astrophysical Journal*, **106**, pp. 121-127, 1947.
link: <https://adsabs.harvard.edu/pdf/1947ApJ...106..121V>

176. Vangvichith M., Tran H., and Hartmann J.-M., “Line-mixing and collision induced absorption for O₂–CO₂ mixtures in the oxygen A-band region”, *Journal of Quantitative Spectroscopy and Radiative Transfer*, **110** (18), pp.2212-2216, 2009. doi: <https://doi.org/10.1016/j.jqsrt.2009.06.002>

177. Villanueva G.L., Smith M.D., Protopapa S., Faggi S., and Mandell A.M., “Planetary Spectrum Generator: An accurate online radiative transfer suite for atmospheres, comets, small bodies and exoplanets”, *Journal of Quantitative Spectroscopy and Radiative Transfer*, **217**, pp. 86-104, 2018. doi: <https://doi.org/10.1016/j.jqsrt.2018.05.023>

178. Wcisło P. and Coauthors, “The first comprehensive dataset of beyond-Voigt line-shape parameters from ab initio quantum scattering calculations for the HITRAN database: He-perturbed H₂ case study”, *Journal of Quantitative Spectroscopy and Radiative Transfer*, **260**, 2021. doi: <https://doi.org/10.1016/j.jqsrt.2020.107477>

179. Wells R.J., “Rapid approximation to the Voigt/Faddeeva function and its derivatives”, *Journal of Quantitative Spectroscopy and Radiative Transfer*, **62** (1), pp. 29–48, 1999. doi: [https://doi.org/10.1016/S0022-4073\(97\)00231-8](https://doi.org/10.1016/S0022-4073(97)00231-8)

180. Werdell P. J., and Coauthors, “The Plankton, Aerosol, Cloud, Ocean Ecosystem Mission: Status, Science, Advances”, *Bulletin of the American Meteorological Society*, **100** (9), pp. 1775–1794, 2019. doi: <https://doi.org/10.1175/BAMS-D-18-0056.1>

181. Wilson G., and Coauthors, “Best practices for scientific computing”, *PLOS Biology*, **12** (1), e1001745, 2014. doi: <https://doi.org/10.1371/journal.pbio.1001745>

182. Xie Y., Sengupta M., and Dudhia J., “A Fast All-sky Radiation Model for Solar applications (FARMS): Algorithm and performance evaluation”, *Solar Energy*, **135**, pp. 435–445, 2016. doi: <https://doi.org/10.1016/j.solener.2016.06.003>

183. Yang Q., Liu X., Wu W., Kizer S., and Baize R. R., “Fast and accurate hybrid stream PCRTM-SOLAR radiative transfer model for reflected solar spectrum simulation in the cloudy atmosphere”, *Optics Express*, **24** (26), pp. A1514-A1527, 2016. doi: <https://doi.org/10.1364/OE.24.0A1514>

184. Yang Y., Marshak A., Mao J., Lyapustin A., and Herman J., “A method of retrieving cloud top height and cloud geometrical thickness with oxygen A and B bands for the Deep Space Climate Observatory (DSCOVR) mission: Radiative transfer simulations”, *Journal of Quantitative Spectroscopy and Radiative Transfer*, **122**, pp. 141–149, 2013. doi: <https://doi.org/10.1016/j.jqsrt.2012.09.017>

185. Zhou Y., Wang C., Ren T., and Zhao C., “A machine learning based full-spectrum correlated k-distribution model for nonhomogeneous gas-soot mixtures”, *Journal of Quantitative Spectroscopy and Radiative Transfer*, **268**: 107628, 2021. doi: <https://doi.org/10.1016/j.jqsrt.2021.107628>

186. Zhu M., Zhang F., Li W., Wu Y., and Xu N., “The impact of various HITRAN molecular spectroscopic databases on infrared radiative transfer simulation”, *Journal of Quantitative Spectroscopy and Radiative Transfer*, **234**, pp.55-63, 2019. doi: <https://doi.org/10.1016/j.jqsrt.2019.04.031>